Spin effects in single-electron tunnelling

2008 J. Phys.: Condens. Matter 20 423202

(http://iopscience.iop.org/0953-8984/20/42/423202)

IOP PUBLISHING JOURNAL OF PHYSICS: CONDENSED MATTER

J. Phys.: Condens. Matter **20** (2008) 423202 (36pp) doi:10.1088/0953-8984/20/42/423202

TOPICAL REVIEW

Spin effects in single-electron tunnelling

J Barnaś[1,2] **and I Weymann**[1]

[1] Department of Physics, Adam Mickiewicz University, 61-614 Poznań, Poland
[2] Institute of Molecular Physics, Polish Academy of Sciences, 60-179 Poznań, Poland

E-mail: barnas@amu.edu.pl and weymann@amu.edu.pl

Received 31 March 2008, in final form 16 June 2008
Published 18 September 2008
Online at stacks.iop.org/JPhysCM/20/423202

Abstract

An important consequence of the discovery of giant magnetoresistance in metallic magnetic multilayers is a broad interest in spin-dependent effects in electronic transport through magnetic nanostructures. An example of such systems are tunnel junctions—single-barrier planar junctions or more complex ones. In this review we present and discuss recent theoretical results on electron and spin transport through ferromagnetic mesoscopic junctions including two or more barriers. Such systems are also called ferromagnetic single-electron transistors. We start from the situation when the central part of a device has the form of a magnetic (or nonmagnetic) metallic nanoparticle. Transport characteristics then reveal single-electron charging effects, including the Coulomb staircase, Coulomb blockade, and Coulomb oscillations. Single-electron ferromagnetic transistors based on semiconductor quantum dots and large molecules (especially carbon nanotubes) are also considered. The main emphasis is placed on the spin effects due to spin-dependent tunnelling through the barriers, which gives rise to spin accumulation and tunnel magnetoresistance. Spin effects also occur in the current–voltage characteristics, (differential) conductance, shot noise, and others. Transport characteristics in the two limiting situations of weak and strong coupling are of particular interest. In the former case we distinguish between the sequential tunnelling and cotunnelling regimes. In the strong coupling regime we concentrate on the Kondo phenomenon, which in the case of transport through quantum dots or molecules leads to an enhanced conductance and to a pronounced zero-bias Kondo peak in the differential conductance.

(Some figures in this article are in colour only in the electronic version)

Contents

1. Introduction 2
   1.1. Basic concepts 3
   1.2. Transport regimes 3
2. Ferromagnetic single-electron transistors based on metallic nanoparticles 4
   2.1. Transport in the sequential tunnelling regime 5
   2.2. Contribution to the conductance due to cotunnelling processes 7
   2.3. Discrete energy structure of the island 8
   2.4. Shot noise in ferromagnetic SETs 9
3. Transport in double-island devices 10
   3.1. Fast spin relaxation: no spin accumulation 11
   3.2. Slow spin relaxation: spin accumulation 12
4. Spin-polarized transport through single-level quantum dots connected to ferromagnetic leads 13
   4.1. Quantum dots weakly coupled to ferromagnetic leads: collinear magnetizations 14
   4.2. Transport through quantum dots in the Coulomb blockade regime: collinear magnetizations 18
   4.3. Systems with noncollinear magnetizations 23
5. Transport through multi-level quantum dots connected to ferromagnetic leads 25
   5.1. Sequential transport in two-level dots 25
   5.2. Cotunnelling in two-level quantum dots 28
   5.3. Multi-level quantum dots based on single-wall carbon nanotubes 29

6. Kondo effect in quantum dots coupled to ferromagnetic leads 30
6.1. Poor man's scaling approach 31
6.2. Numerical renormalization group 31
6.3. Nonequilibrium transport: zero-bias anomaly 31
7. Concluding remarks 33
Acknowledgments 33
References 33

1. Introduction

In the last few decades one can observe a common pursuit towards miniaturization of electronic systems. According to the empirical Moore's law, the number of transistors per microchip is doubled every two years. It is however obvious that the possibility of further miniaturization will be stopped in the near future due to the loss of chip stability when the device components achieve critical dimensions in the nanometre range. Thus, the most challenging task facing contemporary science and technology is to implement structures, alternative to the silicon-based devices, whose size could be reduced further.

The same tendency can also be observed in the development of hard discs, whose memory cells become smaller and smaller every year. This generates new challenges related to information reading/writing. An important step towards further miniaturization was the discovery of the giant magnetoresistance (GMR) effect. The GMR was discovered in 1988 in artificially layered metallic structures consisting of ferromagnetic 3d films separated by nonmagnetic metallic layers [1, 2]. It turned out that the electrical resistance of magnetic metallic multilayers depends on their magnetic state, and usually drops when the magnetic configuration varies from antiparallel alignment to the parallel one [1–4]. The GMR effect occurs for a current flowing in the film plane as well as perpendicular to it. This phenomenon turned out to be very useful for applications in highly sensitive read heads, and allowed reading information from smaller memory cells using their weak magnetic field.

The discovery of GMR initiated a broad interest in spin-polarized electronic transport in nanoscopic systems. It turned out that electron spin provides an additional degree of freedom, which considerably broadens the range of applications of mesoscopic systems in novel electronic devices. The spin-based nanoelectronics—called now spin electronics or shortly spintronics—is a relatively new area of mesoscopic physics dealing with the interplay of charge and spin degrees of freedom [5–12]. Although a lot of theoretical and experimental work on the spintronic properties of mesoscopic systems has been carried out, this field is still in an early stage of development.

An effect similar to the aforementioned GMR also occurs when nonmagnetic metallic layer in a trilayer structure is replaced with a nonmagnetic insulating barrier, and the current flows owing to the phenomenon of quantum-mechanical tunnelling through the barrier. This effect was discovered in 1975 in ferromagnetic planar junctions by Julliére [13], and is of current interest due to applications in magnetic storage technology (magnetic random access memories) and in spin-electronics devices [5–12]. As in the case of GMR, the tunnel magnetoresistance (TMR) consists of a decrease (increase is also possible) in the junction resistance when the magnetic configuration of the junction changes from the antiparallel to parallel one. Tunnelling in complex junctions, particularly in mesoscopic ones, where charging effects become important, is still not fully explored. A specific kind of such systems are double-barrier junctions with a small central electrode (called an island). Such systems are known as single-electron transistors (SETs), mainly because electrons in a biased device flow one by one through the system and the transfer of single electrons can be controlled by a gate voltage. Electronic transport in such devices was extensively studied in the past decade, but mainly in the nonmagnetic limit [14–22].

Recent experiments on magnetic nanostructured materials revealed new phenomena associated with the interplay of ferromagnetism and discrete charging effects. A typical example is a ferromagnetic single-electron transistor, i.e., a small metallic nanoparticle (semiconducting quantum dots or molecules are also possible) coupled by tunnel barriers to ferromagnetic electrodes [23, 24]. The first ferromagnetic single-electron transistors were fabricated by Ono *et al* [25, 26] and later by Brückl *et al* [27]. Transport in ferromagnetic single-electron transistors with nonmagnetic metallic islands—both normal and superconducting—was also measured [28–31]. One should bear in mind, that the interplay of spin and charge effects had already been studied a long time ago in granular systems, in which magnetic nanoparticles were randomly dispersed in a nonmagnetic matrix [32]. Recently granular films were investigated again by several groups [33–40], but both the size of the grains and also their location were strictly controlled.

In the case of sufficiently large metallic islands (but still in the nanometre range), the discrete structure of the electronic states in the grain is not resolved and is irrelevant. To observe the discrete electronic states in transport characteristics one should either reduce the size of the metallic nanoparticles [41], or use semiconducting quantum dots based on a two-dimensional electron gas [42–45]. An alternative strategy is to use ferromagnetic semiconducting materials instead of metallic ones as the electrodes [46]. Magnetic impurities in the middle of the tunnel barrier of a ferromagnetic tunnel junction [47–50] can also be considered as quantum dots with a very strong Coulomb interaction. Another group of single-electron devices are molecular ferromagnetic transistors [51] and, especially, ferromagnetically contacted carbon nanotubes [52–62].

In the following we will review basic transport characteristics of ferromagnetic single-electron transistors in the sequential tunnelling, cotunnelling, and strong coupling (Kondo) regimes. In particular, we will consider properties of the device such as charge and spin currents, tunnel magnetoresistance, spin accumulation, shot noise, Kondo effect, and others. In section 2 we review the basic principles of single-electron transport in the case of a large metallic island attached to ferromagnetic leads. The size of the island is however small enough so that the charging energy is the dominant energy scale in the system. The

limits of fast and slow spin relaxation in the island are also discussed. Then we consider shot noise and the role of discrete electronic structure in such devices. In section 3 we consider devices based on double metallic islands. In turn, in section 4 we deal with electronic transport through single-level quantum dots (QDs) in the sequential tunnelling and cotunnelling regimes. Transport through multi-level QDs, including transport through two-level quantum dots and carbon nanotubes attached to ferromagnetic leads is discussed in section 5. Transport through quantum dots in the Kondo regime is briefly addressed in section 6. Final conclusions are in section 7.

1.1. Basic concepts

The systems considered in this review consist of a mesoscopic central part (island) coupled by tunnel barriers to external ferromagnetic leads. The central part is characterized by an addition energy, which corresponds to the energy needed to add a single electron, and includes contributions from the electrostatic charging energy and the discrete single-particle-level separation. If the charging energy is the most relevant energy scale, the systems exhibit single-electron charging effects [15, 63–69]. An electron can tunnel to the central part only when the energy provided by the transport voltage surpasses the corresponding charging energy; otherwise, the current is exponentially suppressed and the system is in the Coulomb blockade regime [14, 70, 71]. Once the bias voltage is larger than the threshold voltage, the electrons can tunnel one by one through the system leading to a step-like current–voltage characteristics—the so-called Coulomb staircase. The blockade can also be overcome by applying a gate voltage V_g that leads to a sawtooth-like variation of electric current with V_g—the so-called Coulomb oscillations [15, 63, 64, 67, 72].

When the electrodes are made of a ferromagnetic material, the system exhibits further interesting phenomena resulting from the interplay of charge and spin degrees of freedom [73, 74]. In particular, the tunnelling current flowing through the system depends on the relative alignment of the magnetic moments of ferromagnetic electrodes, giving rise to the TMR effect [25, 26], which is described quantitatively by the ratio

$$\mathrm{TMR} = \frac{R_{\mathrm{AP}} - R_{\mathrm{P}}}{R_{\mathrm{P}}} = \frac{I_{\mathrm{P}} - I_{\mathrm{AP}}}{I_{\mathrm{AP}}}, \tag{1}$$

where R_{P} and R_{AP} denote the total system resistance in the parallel and antiparallel magnetic configurations, respectively, and I_{P}, I_{AP} are the corresponding currents. A simple theoretical model of TMR was introduced by Jullière [13], who considered a single planar ferromagnetic tunnel junction and showed that TMR in such a device is given by $\mathrm{TMR}^{\mathrm{Jull}} = 2p_{\mathrm{L}}p_{\mathrm{R}}/(1 - p_{\mathrm{L}}p_{\mathrm{R}})$, where the spin polarization p_r of the lead r ($r = \mathrm{L}, \mathrm{R}$ for the left/right lead) is defined as

$$p_r = \frac{\rho_{r+} - \rho_{r-}}{\rho_{r+} + \rho_{r-}}, \tag{2}$$

with $\rho_{r\pm}$ being the spin-dependent density of states of lead r for the spin-majority (+) and spin-minority (−) electrons.

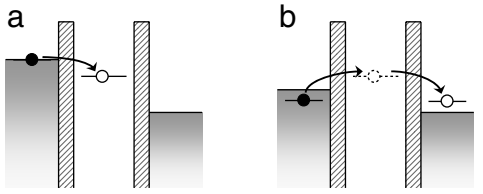

Figure 1. A sketch illustrating (a) a single first-order (sequential tunnelling) process, and (b) a second-order (cotunnelling) transport process.

1.2. Transport regimes

In the following considerations we will distinguish between the three different transport regimes:

Sequential tunnelling. In the regime of weak coupling between the island and leads, and out of the Coulomb blockade, electron transport is dominated by processes of the first order in the coupling parameter. Electrons flow then consecutively one by one due to the tunnelling events, and the transition rate from an initial state $|i\rangle$ to a final state $|f\rangle$ can be determined from the Fermi golden rule,

$$\alpha_{i\to f} = \frac{2\pi}{\hbar}\,|\langle i|H_{\mathrm{T}}|f\rangle|^2\,\delta(\varepsilon_i - \varepsilon_f), \tag{3}$$

where H_{T} is the relevant tunnelling Hamiltonian, and ε_i (ε_f) is the energy of the initial (final) state. This transport regime is known as the sequential tunnelling regime [14, 15]. An example of a single first-order process is sketched in figure 1(a).

Cotunnelling. Although the sequential tunnelling in the Coulomb blockade regime is exponentially suppressed, the current still flows due to higher-order tunnelling processes involving tunnelling of a single, two or more electrons *via* intermediate virtual states [75–77]. These processes are known as cotunnelling. An exemplary cotunnelling process is illustrated in figure 1(b).

The second-order perturbation theory gives the cotunnelling rate from an initial state $|i\rangle$ to a final state $|f\rangle$ [76]

$$\alpha_{i\to f} = \frac{2\pi}{\hbar}\left|\sum_q \frac{\langle i|H_{\mathrm{T}}|q\rangle\langle q|H_{\mathrm{T}}|f\rangle}{\varepsilon_i - \varepsilon_q}\right|^2 \delta(\varepsilon_i - \varepsilon_f) \tag{4}$$

where the summation is over all virtual states $|q\rangle$, and ε_α is the energy of the state α ($\alpha = i, f, q$). In the Coulomb blockade regime this tunnelling rate is only algebraically suppressed, contrary to the sequential transport processes which are then suppressed exponentially. Because of that even at low temperatures and in the strong Coulomb blockade regime the rates of cotunnelling processes do not vanish. The second-order corrections become also important on resonance for intermediate coupling strengths.

Strong coupling. For strong coupling of the metallic island to electrodes, the tunnelling processes lead to logarithmic corrections to conductance, and the perturbation theory fails at the degeneracy points of two consecutive charge states. Additionally in the case of quantum dots the Kondo effect appears at low temperatures (below the Kondo temperature T_K, $T \lesssim T_K$) leading to an enhanced conductance in the linear response regime [78].

2. Ferromagnetic single-electron transistors based on metallic nanoparticles

In this section we review spin-polarized transport in a metallic ferromagnetic single-electron transistor (FM SET). The device consists of a metallic nanoparticle as the central electrode (island), which is coupled through tunnel barriers to external reservoirs of spin-polarized electrons. A gate voltage is attached capacitively to the island, which allows the control of the position of the corresponding Fermi level.

Electronic transport in nonmagnetic SETs has already been extensively studied in the past two decades [14, 15, 79–89]. Recently attention was also drawn to electron tunnelling in magnetic systems [25, 26, 73, 74, 90–92], stimulated by recent progress in nanotechnology. It has been shown theoretically that some qualitatively new effects may arise from the interplay of charging effects and spin degrees of freedom. These include, for example, oscillations of TMR with increasing bias voltage, spin accumulation, enhancement of TMR in the Coulomb blockade regime, etc [73, 74, 93–98]. The enhancement of TMR in the cotunnelling regime and the oscillations of TMR as a function of the transport voltage have also been observed experimentally [38, 39, 99, 100].

The capacitance C of few-nanometre-size particles is of the order of 10^{-18} F [39, 41, 101]. Consequently, the corresponding charging energy, $E_C = e^2/2C$, establishes a new relevant energy scale. If the charging energy is larger than the thermal energy, $E_C \gg k_B T$, where T denotes the temperature and k_B is the Boltzmann constant, the effects due to discreteness of charge become observable in transport characteristics [14, 15].

The single-electron transistors considered in this section are illustrated schematically in figure 2, where part (a) shows a device whose all three electrodes are ferromagnetic, whereas part (b) shows a system with ferromagnetic source and drain electrodes and a nonmagnetic island. Generally, magnetic moments of the leads may form an arbitrary magnetic configuration. However, we focus on systems whose moments form either a parallel (P) or an antiparallel (AP) magnetic configuration, as shown in figure 2. In the system shown in part (a) the magnetic moments of external electrodes point in the same direction, while magnetic moment of the island is either parallel or antiparallel to them. In the system shown in part (b), magnetic moments of external electrodes in the parallel configuration are aligned, while in the antiparallel configuration they are anti-aligned. The two magnetic alignments can be easily achieved by sweeping magnetic field through the hysteresis loop, provided the respective ferromagnetic components have different coercive fields. One may also make use of exchange anisotropy to fix the magnetic moment of a particular layer and rotate the magnetic moment of the second layer with a weak magnetic field. Generally, there is a chance that electron tunnelling through a barrier will change its spin orientation. However, we consider only spin-conserving tunnelling processes through the two barriers. We also assume that the islands are relatively large, so the effects due to quantization of the corresponding energy levels can be neglected. For smaller islands, however, the discrete energy spectrum may modify transport characteristics [40, 102, 103], and this will be considered later (see section 2.3).

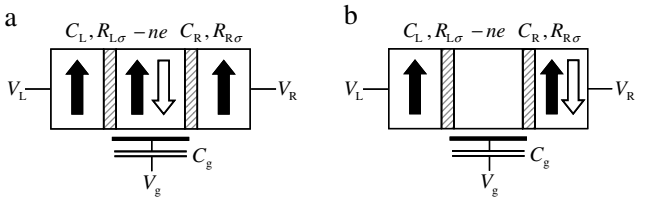

Figure 2. Schematics of ferromagnetic single-electron transistors. The parallel and antiparallel magnetic configurations of the system are also specified. The island is separated from external electrodes by tunnel barriers. Each barrier is characterized by its spin-dependent resistance $R_{r\sigma}$ and capacitance C_r ($r = L, R$). The system is symmetrically biased, $V_L = V/2$, $V_R = -V/2$, and there is also a gate voltage V_g applied to the island.

To describe charge and spin transport we need to specify a model Hamiltonian of the system. First, the electrostatic energy required to add n excess electrons to the island, while keeping constant voltages V_L and V_R in the left and right electrodes and the gate voltage V_g, is given by [104]

$$H_{ch} = E_C \left(n - \frac{Q_g}{e} \right)^2, \tag{5}$$

where a constant term (independent of n) is irrelevant and has been dropped. Here, the total island's capacitance C is the sum of the capacitances of the left and right junctions and of the gate, $C = C_L + C_R + C_g$. The external charge $Q_g \equiv C_L V_L + C_R V_R + C_g V_g$ accounts for the effect of applied voltages, and can be continuously tuned. The total Hamiltonian of the device then takes the general form

$$H = \sum_{r=L,R} H_r + H_I + H_{ch} + H_T \equiv H_0 + H_T. \tag{6}$$

Here H_0 describes the decoupled leads and island, while H_T takes into account the lead–island coupling. The ferromagnetic leads and the island are described by

$$H_r = \sum_{k\sigma} \varepsilon_{rk\sigma} c^\dagger_{rk\sigma} c_{rk\sigma}, \tag{7}$$

for $r = L, R, I$, where $c_{rk\sigma}$ are the Fermi operators for electrons with a wavevector $\mathbf{k}$ and spin σ in the electrodes and island ($r = L, R, I$), and $\varepsilon_{rk\sigma}$ is the corresponding single-particle energy. The last part of the Hamiltonian,

$$H_T = \sum_{r=L,R} \sum_{kq\sigma} t_{rkq\sigma} c^\dagger_{rk\sigma} c_{Iq\sigma} + \text{h.c.} \tag{8}$$

describes tunnelling processes between the leads and island, with $t_{rkq\sigma}$ being the relevant matrix elements.

2.1. Transport in the sequential tunnelling regime

When the resistances of both tunnel barriers are much larger than the quantum resistance, $R_r \gg R_Q \equiv h/e^2$, and the system is not in the Coulomb blockade regime, transport is dominated by sequential tunnelling processes. As a consequence, the charge is well localized in the island and the *orthodox* tunnelling theory is applicable [14, 15].

In order to calculate electric current in the sequential transport regime, one may use the method based on the master equation which is a detailed balance of electrons tunnelling to and off the island. In the stationary case the master equation reads

$$\begin{aligned} 0 = &-\sum_{\sigma}\left[\Gamma^{+}_{\mathrm{L}\sigma}(n)+\Gamma^{-}_{\mathrm{L}\sigma}(n)+\Gamma^{+}_{\mathrm{R}\sigma}(n)+\Gamma^{-}_{\mathrm{R}\sigma}(n)\right]P(n,V)\\ &+\sum_{\sigma}\left[\Gamma^{+}_{\mathrm{L}\sigma}(n-1)+\Gamma^{+}_{\mathrm{R}\sigma}(n-1)\right]P(n-1,V)\\ &+\sum_{\sigma}\left[\Gamma^{-}_{\mathrm{L}\sigma}(n+1)+\Gamma^{-}_{\mathrm{R}\sigma}(n+1)\right]P(n+1,V), \end{aligned} \tag{9}$$

where $P(n, V)$ is the probability to find the island in a state with n additional electrons when a bias voltage V ($V = V_{\mathrm{L}} - V_{\mathrm{R}}$) is applied, and $\Gamma^{\pm}_{r\sigma}(n)$ is the spin-dependent rate for tunnelling of electrons with spin σ from the lead r to island (upper sign) and from the island to lead r (lower sign), when the island is occupied by n excess electrons. These tunnelling rates depend on the bias voltage (not indicated explicitly), and can be expressed by means of the Fermi golden rule as

$$\Gamma^{\pm}_{r\sigma}(n) = \frac{1}{e^2 R_{r\sigma}} \frac{\Delta E^{\pm}_{r\sigma}(n)}{\exp\left[\Delta E^{\pm}_{r\sigma}(n)/k_{\mathrm{B}}T\right]-1}, \tag{10}$$

where $\Delta E^{\pm}_{r\sigma}(n)$ describes a change in the electrostatic energy of the system caused by the corresponding tunnelling event, when in the initial state there were n additional electrons on the island. In the above equation $R_{r\sigma}$ denotes the spin-dependent tunnel resistance of the rth barrier, given by

$$R_{r\sigma} = \frac{\hbar}{2\pi e^2 \rho_{r\sigma}\rho_{\mathrm{I}\sigma}|t_{r\sigma}|^2}, \tag{11}$$

where $t_{r\mathbf{kq}\sigma} = t_{r\sigma}$ has been assumed for simplicity. The spin dependence of the resistance is a consequence of the spin-dependent density of electron states at the Fermi level in the respective electrodes and the corresponding tunnelling matrix elements. In particular, in equation (11) it is due to the spin-dependent density of states of the rth lead, $\rho_{r\sigma}$, spin-dependent density of states of the island, $\rho_{\mathrm{I}\sigma}$, as well as due to the spin-dependent tunnelling matrix elements $t_{r\sigma}$.

In a stationary state, the net transition rate between the charge states with n and $n+1$ excess electrons on the island vanishes. The probability $P(n, V)$ can be then determined from the following recursion relation [83, 84]

$$P(n+1,V)\sum_{\sigma} y^{\sigma}(n+1) = P(n,V)\sum_{\sigma} x^{\sigma}(n), \tag{12}$$

where $x^{\sigma}(n) = \sum_{r=\mathrm{L,R}} \Gamma^{+}_{r\sigma}(n)$ and $y^{\sigma}(n) = \sum_{r=\mathrm{L,R}} \Gamma^{-}_{r\sigma}(n)$, corresponding to transition rates for tunnelling to and off the island, respectively.

Generally, the energy of an electron after a tunnelling event is relaxed to the relevant Fermi level in a short timescale. One can assume that the energy-relaxation time is the shortest timescale, shorter than the time between two successive tunnelling events. However, such a restriction cannot be imposed on the spin-relaxation time which can be relatively long. In a general case, a nonequilibrium magnetic moment may accumulate on the island due to the spin dependence of tunnelling processes, which leads to spin splitting of the corresponding Fermi level. For arbitrary spin-relaxation times, the splitting of the Fermi level can be determined from the spin balance [96, 105]

$$\frac{1}{e}(I^{\sigma}_{\mathrm{R}} - I^{\sigma}_{\mathrm{L}}) - \frac{\rho_{\mathrm{I}\sigma}\Omega_{\mathrm{I}}}{\tau_{\mathrm{sf}}}\Delta E^{\sigma}_{\mathrm{F}} = 0, \tag{13}$$

where Ω_{I} is the island's volume, $-e$ is the electron charge ($e > 0$), τ_{sf} denotes the spin-relaxation time on the island, while I^{σ}_{L} and I^{σ}_{R} are the currents flowing through the left and right junctions in the spin channel σ. The last term in equation (13) takes into account intrinsic spin-flip processes on the island. From this condition it is possible to calculate self-consistently the shifts of the Fermi levels due to spin accumulation for both spin orientations.

The electric current flowing through the left junction can be calculated from the following formula:

$$I_{\mathrm{L}} = \sum_{\sigma} I^{\sigma}_{\mathrm{L}} = -e\sum_{\sigma}\sum_{n=-\infty}^{\infty}\left[\Gamma^{+}_{\mathrm{L}\sigma}(n) - \Gamma^{-}_{\mathrm{L}\sigma}(n)\right]P(n,V). \tag{14}$$

A similar formula also holds for I_{R}. In the stationary state the currents flowing through both junctions are equal, $I_{\mathrm{L}} = I_{\mathrm{R}} \equiv I$.

In the following we discuss two limiting cases: the limit of fast spin relaxation and the limit of slow spin relaxation on the island. In the former case the spin of an electron tunnelling to the island relaxes before a next tunnelling event takes place. In the latter case, on the other hand, the electron spin is conserved for a time much longer than the time between successive tunnelling events.

2.1.1. Fast spin relaxation. In the limit of fast spin relaxation, SETs with nonmagnetic islands behave like nonmagnetic junctions, exhibiting no TMR effect. Therefore, the following discussion in this subsection is limited to FM SETs with ferromagnetic islands, see figure 2(a). Generally, one may assume that the spin-dependent resistances for the parallel ($R^{\mathrm{P}}_{r\sigma}$) and antiparallel ($R^{\mathrm{AP}}_{r\sigma}$) configurations fulfil the condition $R^{\mathrm{P}}_{r\sigma}R^{\mathrm{P}}_{r\bar{\sigma}} = R^{\mathrm{AP}}_{r\sigma}R^{\mathrm{AP}}_{r\bar{\sigma}}$, where $\bar{\sigma} \equiv -\sigma$. This formula follows from equation (11) when assuming that all spin effects are included into the spin-dependent density of states (transfer matrix element are independent of spin and magnetic configuration). Moreover, since there is no spin accumulation on the island in the limit of fast spin relaxation, there is no associated spin splitting of the Fermi level, $\Delta E^{\sigma}_{\mathrm{F}} = 0$.

The current flowing through the system in the parallel and antiparallel configurations is displayed in figure 3(a). For both magnetic configurations, the I–V curves reveal the well-known Coulomb steps. Moreover, these two curves are

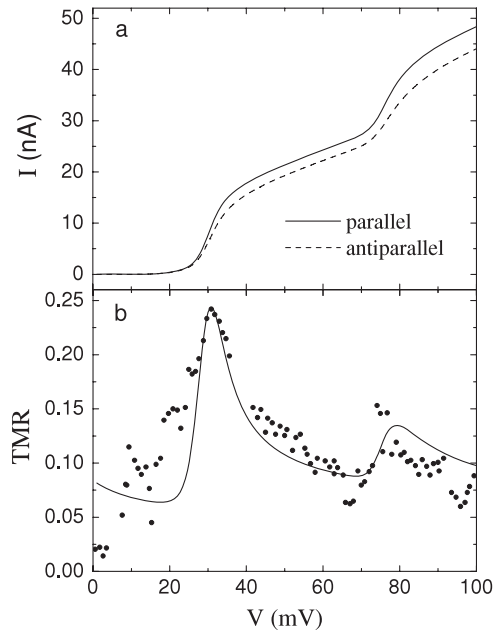

Figure 3. Current in the parallel and antiparallel magnetic configurations (a) and the resulting TMR (b) as a function of the bias voltage for a FM SET with a ferromagnetic island in the limit of fast spin relaxation. The parameters are: $T = 9$ K, $R^{\mathrm{P}}_{\mathrm{L}\uparrow} = 0.65$ MΩ, $R^{\mathrm{P}}_{\mathrm{L}\downarrow} = 0.065$ MΩ, $R^{\mathrm{P}}_{\mathrm{R}\uparrow} = 5$ MΩ, $R^{\mathrm{P}}_{\mathrm{R}\downarrow} = 2.5$ MΩ, $R^{\mathrm{AP}}_{r\downarrow} = R^{\mathrm{AP}}_{r\uparrow} = (R^{\mathrm{P}}_{r\uparrow} R^{\mathrm{P}}_{r\downarrow})^{1/2}$ (for $r = \mathrm{L}, \mathrm{R}$), $C_{\mathrm{L}} = 0.1$ aF, $C_{\mathrm{R}} = 1$ aF, $C_{\mathrm{g}} = 5.1$ aF, $V_{\mathrm{g}} = 0$, and the offset charge $Q_0 = 0.025e$. The dots in part (b) present the experimental data taken from [39].

different; the current flowing in the parallel configuration is generally larger than the current flowing in the antiparallel configuration, see figure 3(a). This difference leads in turn to a nonzero TMR effect, as shown in figure 3(b). The TMR effect has a component that oscillates as a function of the bias voltage. The amplitude of these oscillations, however, decreases as the transport voltage increases. For the parameters assumed here, TMR reaches a local maxima at the voltages corresponding to the positions of Coulomb steps. However, this is not a general rule, and for other parameters TMR can have local minima at the Coulomb steps. The global maximum value of TMR in figure 3(b) appears at the first step, i.e., at the threshold voltage. When the temperature increases, the effects due to discrete charging, i.e. the Coulomb steps and enhancement of TMR at the Coulomb steps become diminished and disappear at $k_{\mathrm{B}}T \approx E_{\mathrm{C}}$ [98]. The oscillatory behaviour of the TMR effect with increasing transport voltage was observed experimentally, for example by Ernult *et al* [39], see the dots in figure 3(b). The curves presented in figure 3 are calculated for the parameters corresponding to those in [39]. To get a good agreement with experimental observations, a nonzero offset charge Q_0 on the island (due to external charges) has been assumed. As can be seen in figure 3(b), there is a satisfactory agreement between the theoretical curve and experimental data for voltages above the threshold, $V \gtrsim 30$ mV, while in the Coulomb blockade regime transport calculated using the sequential tunnelling approximation is not properly described.

2.1.2. Slow spin relaxation. In the case of a FM SET with a nonmagnetic island, see figure 2(b), a nonzero TMR in the sequential tunnelling regime can exist only when the spin-relaxation time is sufficiently long, i.e. significantly longer than the time between successive tunnelling events. We note that the longest spin-relaxation times were measured for aluminium and copper [106, 107] (for example, the relaxation time for copper was estimated to be of the order of 10^{-7} s). If this is the case, a nonequilibrium magnetic moment builds up on the island due to spin accumulation. This moment leads a nonvanishing TMR. In other words, the island becomes magnetized in a nonequilibrium situation, and the created moment depends on the bias and gate voltages.

Since the density of states at the Fermi level in a nonmagnetic island is independent of the spin orientation, one finds $\Delta E^{\sigma}_{\mathrm{F}} = -\Delta E^{\bar{\sigma}}_{\mathrm{F}}$. In addition to this, the resistances in the antiparallel configuration are $R^{\mathrm{AP}}_{\mathrm{L}\sigma} = R^{\mathrm{P}}_{\mathrm{L}\sigma}$ and $R^{\mathrm{AP}}_{\mathrm{R}\sigma} = R^{\mathrm{P}}_{\mathrm{R}\bar{\sigma}}$, see also figure 2(b).

Typical transport characteristics of a FM SET with nonmagnetic island in the limit of slow spin relaxation are shown in figure 4 as a function of the bias voltage. The splitting of the Fermi level is displayed in figure 4(a) for both magnetic configurations. As one expects, the splitting takes place only in the antiparallel alignment, while in the parallel configuration there is no spin accumulation. In the former case the ratio of tunnelling rates for electrons with opposite spin orientations becomes the same for electrons tunnelling to and off the island only when a nonequilibrium magnetic moment is built on the island. In the parallel configuration, however, this condition is already fulfilled without any spin accumulation. However, this is true only in the case where both junctions are characterized by equal spin asymmetries. When the spin asymmetries of both electrodes are different, spin accumulation also occurs in the parallel configuration.

As illustrated in figure 4(a), behaviour of the Fermi level splitting with increasing transport voltage can be decomposed into two components. One component monotonously increases, while the second one oscillates with increasing bias voltage. This oscillatory behaviour can be accounted for in the following way. Let us assume that the voltage is slightly above that corresponding to a certain Coulomb step and begins to increase. Then, the spin accumulation also increases, until a local maximum value is reached. The local maximum occurs at a voltage at which the chemical potential of the depleted spin channel approaches the value which allows the next charge state in the island. This, in turn, enhances the tunnelling rate (onto the island) of electrons corresponding to the depleted spin channel, and consequently reduces the spin splitting of the Fermi level. When the voltage increases further, a local minimum in the spin accumulation is then reached at a voltage, where the chemical potential of the second (accumulated) spin channel approaches the value which allows the next charge state on the island. The same scenario repeats at each Coulomb step leading to the oscillatory component in the spin accumulation. In the sequential tunnelling regime, where only the first-order tunnelling processes are taken into account, spin accumulation is exponentially small in the Coulomb blockade regime, as can be seen in figure 4(a).

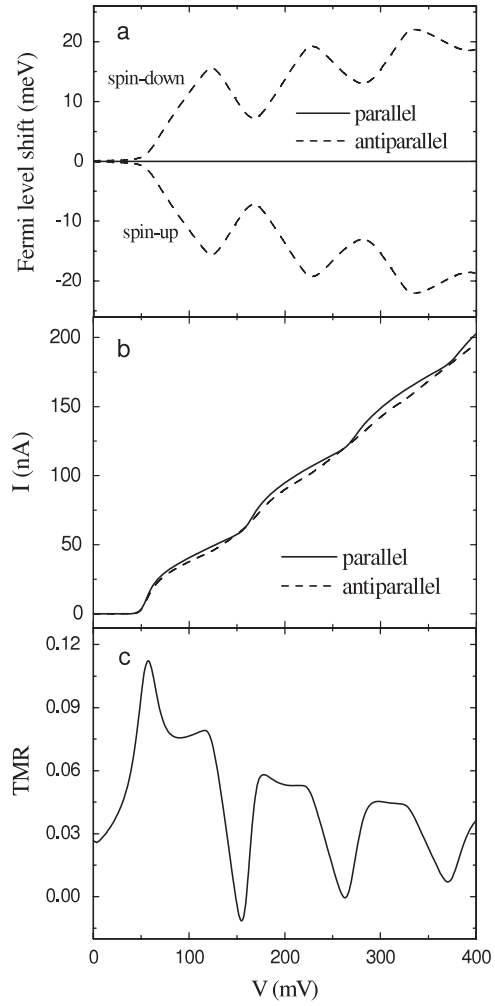

Figure 4. Basic characteristics of a FM SET with a nonmagnetic island as a function of the bias voltage in the limit of slow spin relaxation on the island: (a) spin splitting of the Fermi level, (b) I–V characteristics, and (c) tunnel magnetoresistance. The parameters are: $k_BT = 0.05\,E_C$, $R^P_{L\uparrow} = 5$ MΩ, $R^P_{L\downarrow} = 2.5$ MΩ, $R^P_{R\uparrow} = 0.3$ MΩ, $R^P_{R\downarrow} = 0.15$ MΩ, $C_L = C_R = C_g = 1$ aF, and $V_g = 0$.

The current as a function of the bias voltage for the parallel and antiparallel configurations is shown in figure 4(b). As before, characteristic Coulomb steps are clearly visible. Moreover, owing to different stationary spin accumulations in the parallel and antiparallel configurations, the current in the parallel configuration is also different from that in the antiparallel configuration. This gives rise to the TMR effect which is presented in figure 4(c). Now, the bias dependence is more complex than it was in the case of FM SETs with magnetic islands in the absence of spin accumulation. It is interesting to note, that TMR can change sign in the vicinity of the Coulomb steps in current–voltage curves, which is a consequence of different spin accumulations in the two magnetic configurations.

Generally, it is more difficult to obey the slow spin-relaxation limit in ferromagnetic islands than in nonmagnetic ones. Anyway, some experimental data show that this is achievable. In such a case the spin accumulation builds up in the magnetic island and has significant influence on transport characteristics. In [93, 105] it has been shown that spin accumulation modifies the 'staircase'-like variation of the electric current with the bias voltage. Since the spin accumulation depends on the magnetic configuration of the junction, this can also lead to an enhanced TMR effect. Moreover, in some voltage regions TMR can change sign. In addition, the Coulomb steps for the two magnetic configurations become slightly shifted, as was also observed experimentally [49]. The difference between current–voltage curves in the fast and slow spin-relaxation limits varies continuously with spin-relaxation rates. This difference was used very recently to evaluate the spin-relaxation time in Co nanoparticles [40].

2.2. Contribution to the conductance due to cotunnelling processes

The electric current and spin accumulation in the limit of sequential tunnelling (see the preceding subsection) are exponentially small in the Coulomb blockade regime. However, charge transport may occur not only due to spin-dependent sequential tunnelling, but also due to spin-dependent cotunnelling processes [74, 97, 108], which give a dominant contribution in the Coulomb blockade regime and also lead to spin accumulation [108, 109]. Close to resonance (in the vicinity of the threshold voltage) both sequential and cotunnelling currents may be comparable. The current I is then equal to the sum of first-, $I^{(1)}$, and second-, $I^{(2)}$, order contributions, $I = I^{(1)} + I^{(2)}$.

To calculate cotunnelling current far from the resonance one could use equation (4). This formula, however, cannot be used when voltage approaches the threshold voltage (at resonance). To calculate current and associated spin accumulation in the whole voltage range, the real-time diagrammatic formalism [97, 104, 110, 111] has been used. The spin accumulation on the island (or equivalently spin splitting of the electrochemical potential) is then determined from the spin balance equation, similarly to in the sequential tunnelling regime, see equation (13).

The differential conductance in the whole (sequential and cotunnelling) transport regime is shown in figure 5 for SETs with Ni and Fe electrodes and for nonmagnetic islands (in the limit of slow spin relaxation). The upper part corresponds to the parallel configuration while the lower one corresponds to the antiparallel one. First, we find a well-resolved splitting of the conductance peaks in the antiparallel alignment, while no splitting can be seen in the parallel configuration. This splitting in the conductance peaks is a direct consequence of the spin splitting of the corresponding electrochemical potential of the island, and therefore can be used to detect and measure spin accumulation. The absence of conductance splitting in the parallel configuration is simply a consequence of the absence of spin accumulation in this configuration. Such a splitting of the conductance peaks in the cotunnelling regime was recently observed experimentally [49]. Generally, there are several experimental techniques by which the spin accumulation can be detected indirectly [107, 112]. The peculiarities of transport characteristics of FM SETs offer new possibilities.

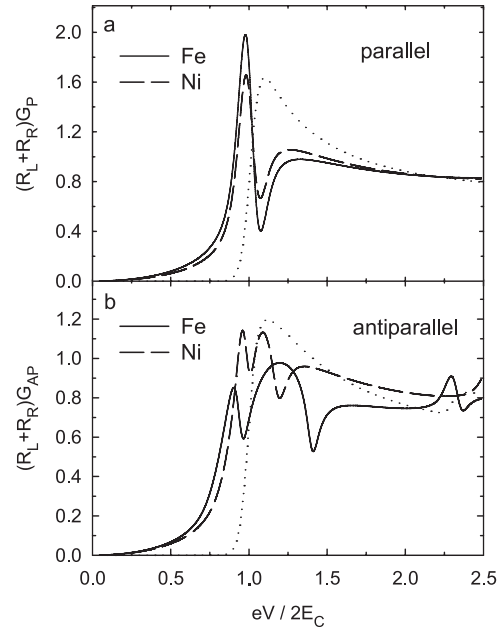

Figure 5. Differential conductance in FM SETs with nonmagnetic islands as a function of the bias voltage V in the (a) parallel and (b) antiparallel configurations, calculated in the whole (sequential and cotunnelling) transport regime in the limit of slow spin relaxation in the island. The curves have been calculated for $k_BT/E_C = 0.02$ and symmetric junctions with $R_{R\uparrow} = 5h/e^2$. The spin polarization is $p = 0.23$ and $p = 0.40$ for Ni and Fe electrodes, respectively. The dotted line corresponds to the sequential tunnelling limit in the SET with Fe electrodes. Reprinted figure with permission from [97]. Copyright 2002 by the American Physical Society.

2.3. Discrete energy structure of the island

The discussion up to now was limited to the case when addition of a single electron costs only electrostatic energy. When, however, the size of metallic island becomes further reduced, the electron spectrum of the island cannot be considered as a continuous one, and the discrete structure of the energy levels plays an important role. Addition of an electron then costs, not only the electrostatic charging energy, but also the energy equal to the level spacing ΔE. In this subsection we briefly describe the effect of discreteness on the transport characteristics. The relevant approach was developed in [102, 103]. The electron transport in the stationary state is then governed by the solution of the generalized master equation [102, 113]

$$\begin{aligned}0 = &-\left\{\Gamma(n_\uparrow,n_\downarrow)+\Omega_{\uparrow,\downarrow}(n_\uparrow,n_\downarrow)+\Omega_{\downarrow,\uparrow}(n_\uparrow,n_\downarrow)\right\}\\ &\times P(n_\uparrow,n_\downarrow,V)+\Gamma^+_\uparrow(n_\uparrow-1,n_\downarrow)P(n_\uparrow-1,n_\downarrow,V)\\ &+\Gamma^+_\downarrow(n_\uparrow,n_\downarrow-1)P(n_\uparrow,n_\downarrow-1,V)\\ &+\Gamma^-_\uparrow(n_\uparrow+1,n_\downarrow)P(n_\uparrow+1,n_\downarrow,V)\\ &+\Gamma^-_\downarrow(n_\uparrow,n_\downarrow+1)P(n_\uparrow,n_\downarrow+1,V)\\ &+\Omega_{\uparrow,\downarrow}(n_\uparrow-1,n_\downarrow+1)P(n_\uparrow-1,n_\downarrow+1,V)\\ &+\Omega_{\downarrow,\uparrow}(n_\uparrow+1,n_\downarrow-1)P(n_\uparrow+1,n_\downarrow-1,V),\end{aligned}\tag{15}$$

where $P(n_\uparrow, n_\downarrow, V)$ denotes the probability of finding $n_\uparrow$ and $n_\downarrow$ excess electrons on the island ($n = n_\uparrow + n_\downarrow$ is the total number of excess electrons). The first term in equation (15) describes how the probability of a given charge and spin state decays due to electron tunnelling to and from the island, whereas other terms describe the rate at which this probability increases. The Ω-terms account for spin-flip relaxation processes. The coefficients entering equation (15) are defined as $\Gamma^\pm_\sigma(n_\uparrow,n_\downarrow) = \sum_{r=L,R}\Gamma^\pm_{r\sigma}(n_\uparrow,n_\downarrow)$ and $\Gamma(n_\uparrow,n_\downarrow) = \sum_\sigma[\Gamma^+_\sigma(n_\uparrow,n_\downarrow)+\Gamma^-_\sigma(n_\uparrow,n_\downarrow)]$, where $\Gamma^\pm_{r\sigma}(n_\uparrow,n_\downarrow)$ are the tunnelling rates for electrons with spin σ, tunnelling to (+) the island from the lead $r = \mathrm{L}, \mathrm{R}$ or backward (−). These coefficients are given by [102, 103]

$$\begin{aligned}\Gamma^\pm_{r\sigma}(n_\uparrow,n_\downarrow) &= \sum_i \gamma^r_{i\sigma}F^\mp_\sigma(E_{i\sigma}|n_\uparrow,n_\downarrow)\\ &\quad\times\ f^\pm(E_{i\sigma}+E^\pm_r(n)-E_\mathrm{F}),\\ \Omega_{\sigma\bar\sigma}(n_\uparrow,n_\downarrow) &= \sum_i\sum_j \omega_{i\sigma,j\bar\sigma}F^+_\sigma(E_{i\sigma}|n_\uparrow,n_\downarrow)\\ &\quad\times\ F^-_{\bar\sigma}(E_{j\bar\sigma}|n_\uparrow,n_\downarrow).\end{aligned}\tag{16}$$

Here, $f^+(E)$ is the Fermi function ($f^- = 1 - f^+$), whereas $F^+_\sigma(E_{i\sigma}|n_\uparrow,n_\downarrow)$ ($F^-_\sigma = 1 - F^+_\sigma$) describes the probability that the energy level $E_{i\sigma}$ is occupied by an electron with spin σ for a particular configuration $(n_\uparrow, n_\downarrow)$. The parameter $\gamma^r_{i\sigma}$ is the bare tunnelling rate of electrons between the lead r and the energy level $E_{i\sigma}$ of the island, and $\omega_{i\sigma,j\bar\sigma}$ is the transition probability from the state $i\sigma$ to $j\bar\sigma$ of the island due to the spin-flip processes. The energies $E^\pm_\mathrm{L}(n)$ and $E^\pm_\mathrm{R}(n)$ are given by $E^\pm_\mathrm{L}(n) = C_\mathrm{R}/C\ eV + U^\pm(n)$ and $E^\pm_\mathrm{R}(n) = -C_\mathrm{L}/C\ eV + U^\pm(n)$ where $U^\pm(n) = E_\mathrm{C}[2(n-n_x)\pm 1]$ and $n_x = C_\mathrm{g}V_\mathrm{g}/e$.

From the solution $P(n_\uparrow, n_\downarrow, V)$ of the master equation (equation (15)), one can determine the current flowing through the island,

$$\begin{aligned}I_\mathrm{L} = -e\sum_\sigma\sum_{n_\uparrow,n_\downarrow}P(n_\uparrow,n_\downarrow,V)\{&\Gamma^+_{\mathrm{L}\sigma}(n_\uparrow,n_\downarrow)\\ &-\Gamma^-_{\mathrm{L}\sigma}(n_\uparrow,n_\downarrow)\}.\end{aligned}\tag{17}$$

For further discussion we assume that the discrete energy levels $E_{i\sigma}$ are spin degenerate (nonmagnetic situation) and equally separated with the level spacing ΔE.

To emphasize the role of spin accumulation let us assume that the intrinsic spin-relaxation time on the island is long enough to neglect all intrinsic spin-flip processes. The corresponding I–V characteristics for the parallel and antiparallel alignments are shown in figure 6(a). In both cases the electric current is blocked below a threshold voltage, and a typical 'Coulomb staircase' appears above it, with additional small steps due to the discrete levels of the island. The effects due to discrete charging and discrete electronic structure are more clearly seen in the differential conductance shown in figure 6(b), where the small peaks correspond to new discrete levels taking part in transport. The difference between the I–V characteristics for the parallel and antiparallel configurations is due to a different spin accumulation in both geometries. In figure 6(c) we see the average value of the difference between the numbers of spin-up and spin-down excess electrons on the island, $\langle M\rangle \equiv \langle n_\uparrow - n_\downarrow\rangle$, i.e., the spin accumulation. There is no significant spin accumulation in the parallel configuration. The number $M \equiv n_\uparrow - n_\downarrow$ of spins accumulated on the island fluctuates with time around its average value $\langle M\rangle$, as shown in figure 6(d), where the standard deviation $(\langle M^2\rangle - \langle M\rangle^2)^{1/2} \equiv [\langle(n_\uparrow - n_\downarrow)^2\rangle - \langle n_\uparrow - n_\downarrow\rangle^2]^{1/2}$ is plotted against the voltage V.

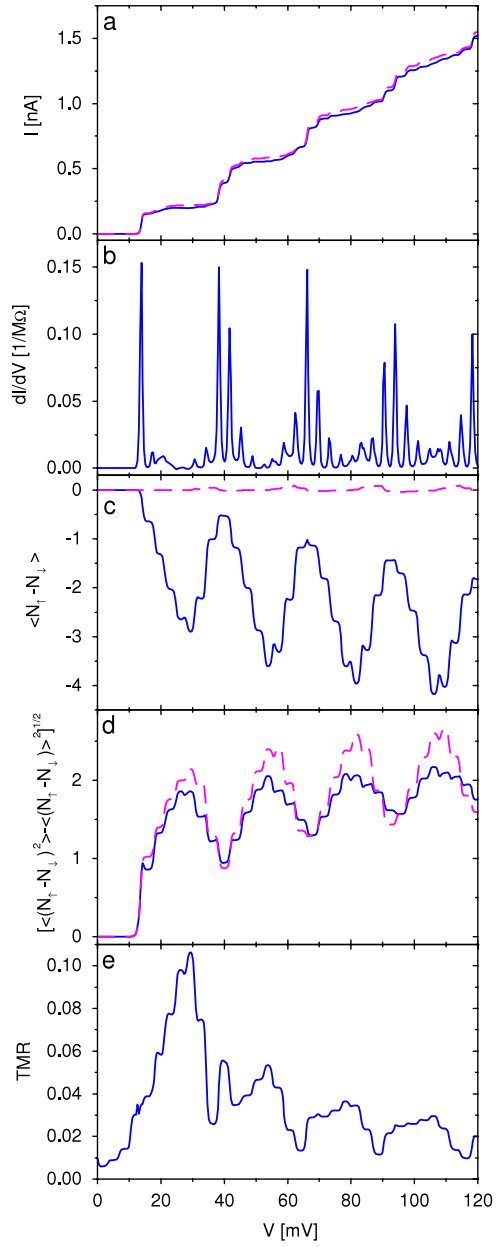

Figure 6. The influence of discrete electronic structure on transport characteristics in a FM SET with nonmagnetic island in the limit of slow spin relaxation. Voltage dependence of the tunnel current I (a), the differential conductance $G = \mathrm{d}I/\mathrm{d}V$ (b), spin accumulation $\langle n_\uparrow - n_\downarrow \rangle$ (c), standard deviation $[\langle (n_\uparrow - n_\downarrow)^2 \rangle - \langle n_\uparrow - n_\downarrow \rangle^2]^{1/2}$ (d), and tunnel magnetoresistance TMR (e), calculated at $T = 2.3$ K. The solid and dashed curves in (a), (c) and (d) correspond to the antiparallel and parallel configurations, respectively. The other parameters are: $\Delta E = 3$ meV, $C_\mathrm{L}/C_\mathrm{L} = 5$, $E_C = 10$ meV, $R_{\mathrm{L}\uparrow} = 2R_{\mathrm{L}\downarrow} = 200$ MΩ, $R_{\mathrm{R}\uparrow} = 2R_{\mathrm{R}\downarrow} = 4$ MΩ and $R_{\mathrm{R}\uparrow} = 2$ MΩ for the parallel alignment ($2R_{\mathrm{R}\uparrow} = R_{\mathrm{R}\downarrow} = 4$ MΩ for the antiparallel alignment). Reproduced with permission from [102]. Copyright 1999 Elsevier.

It is worth noting that although there is almost no spin accumulation in the parallel configuration, the corresponding fluctuations are relatively large.

The difference between the I–V curves in the parallel and antiparallel configurations leads to the tunnel magnetoresistance, shown in figure 6(e). The broad peaks correspond to the Coulomb steps, while the fine structure originates from the discrete structure of the density of states of the island.

One can extend the presented formalism also to the case of a FM SET with a ferromagnetic island [114] and calculate nonequilibrium spin accumulation on the island (when spin-relaxation time is sufficiently long). Using a similar approach Inoue and Brataas [115] analysed current-induced magnetization reversal induced by spin accumulation rather than by spin torque. They found that magnetization reversal is possible when a free energy change due to nonequilibrium spin accumulation is comparable to the anisotropy energy.

2.4. Shot noise in ferromagnetic SETs

From the application point of view, an important transport characteristics of the system is the corresponding current noise. Functionality of a system depends on the relevant noise to signal ratio, which should be as small as possible. However, the noise is also a source of additional information on the system properties like quantum and Coulomb correlations [116]. The shot noise in ferromagnetic single-electron transistors was studied theoretically in [117], where the method developed for spinless electrons in single-electron transistors [118–122] was extended to magnetic systems.

The time correlation function of any two quantities X and Y can be expressed as [123]

$$\langle X(t)Y(0)\rangle = \sum_{n'_\uparrow,n'_\downarrow;n_\uparrow,n_\downarrow} X_{n'_\uparrow,n'_\downarrow} P(n'_\uparrow, n'_\downarrow; t|n_\uparrow, n_\downarrow; 0) \times Y_{n_\uparrow,n_\downarrow} P^0(n_\uparrow, n_\downarrow), \tag{18}$$

where, $P(n'_\uparrow, n'_\downarrow; t|n_\uparrow, n_\downarrow; 0)$ is the conditional probability of finding the system in the final state with $n'_\uparrow$ and $n'_\downarrow$ excess electrons at time t, if there was $n_\uparrow$ and $n_\downarrow$ excess electrons at the initial time $t = 0$. The probability P^0 can be determined from equation (15).

Following this procedure, the current–current correlation function in a FM SET considered in the preceding subsection has been calculated in [117]. The corresponding Fourier transform can be presented as

$$S_\mathrm{II}(\omega) = S_\mathrm{II}^\mathrm{Sh} + S_\mathrm{II}^\mathrm{c}(\omega), \tag{19}$$

where $S_\mathrm{II}^\mathrm{Sh}$ is the Schottky value (the frequency-independent part), while the second term in equation (19) is the frequency-dependent component.

Figure 7(a) shows the bias dependence of the zero-frequency current noise $S_\mathrm{II}(\omega = 0)$. The current noise is smaller in the antiparallel configuration than in the parallel one. This is because in the presence of spin accumulation (which is significant only in the antiparallel alignment) the amplitude of fluctuations is smaller. In figure 7(b) $S_\mathrm{II}(\omega = 0)$ is split into two parts; the frequency-independent component $S_\mathrm{II}^\mathrm{Sh}$ and the contribution $S_\mathrm{II}^\mathrm{c}(\omega = 0)$ arising from the frequency-dependent part of the current noise, see equation (19). The component $S_\mathrm{II}^\mathrm{Sh}$ is almost constant $\approx 2eI(C_1^2 + C_2^2)/C^2$ at the plateaux of the I–V curve and increases with the opening of new channels. Dynamical correlations between the currents are described by $S_\mathrm{II}^\mathrm{c}(\omega)$. Its value in the limit $\omega \to 0$ can be positive between the I–V steps and negative when new channels become open.

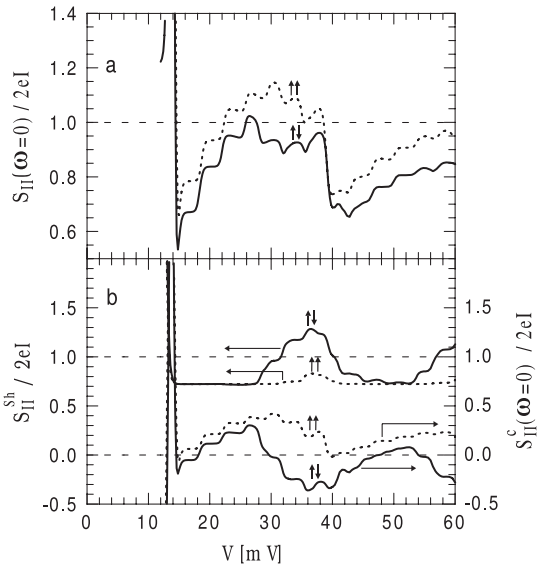

Figure 7. Voltage dependence of the current shot noise at $\omega = 0$ (a) in a FM SET with nonmagnetic island and in the slow spin-relaxation limit for $4R_{L\uparrow} = R_{L\downarrow} = 8$ MΩ, $R_{R\uparrow} = 4R_{R\downarrow} = 240$ MΩ for the antiparallel alignment ($R_{L\uparrow} = 4R_{L\downarrow} = 8$ MΩ, for the parallel configuration) (other parameters as in figure 6). In part (b) $S_{II}(\omega = 0)$ is split into two components: S_{II}^{Sh} (upper curves) and $S_{II}^{c}(\omega = 0)$ (lower curves). Reprinted figure with permission from [117]. Copyright 1999 by the American Physical Society.

This is evident for the antiparallel alignment at $V \approx 26$ mV, when opening a tunnelling channel for electrons with $\sigma = \downarrow$ leads to negative dynamical correlations. This effect is almost compensated by an increase in S_{II}^{Sh}, and therefore one gets only a small reduction of the current noise $S_{II}(\omega = 0)$.

In the power spectrum of the current $S_{II}^{c}(\omega)$ one can distinguish two distinct relaxation times, one in the high and another one in the low-frequency regions [117]. In a wide voltage range the corresponding relaxation times are very close to the effective relaxation times for the charge and spin noise.

The asymmetry between the tunnelling channels for electrons with the opposite spins leads to activation of the spin component in the current noise. In [117] the components $S_{II\,\mathrm{charge}}^{c}$ and $S_{II\,\mathrm{spin}}^{c}$, corresponding to the charge and spin noise, respectively, have been extracted from S_{II}^{c}. It has been shown that the charge component is almost constant whereas the spin component increases with spin polarization p of the leads, and for $p \to 1$ can be much larger than the charge component. The analysis showed that both charge and spin fluctuations are relevant for the shot noise in FM SETs. It has been also pointed out that a super-Poissonian shot noise, the Fano factor $S_{II}(0)/2eI > 1$, can occur due to lifting of the spin degeneracy.

3. Transport in double-island devices

Some new features of transport characteristics appear in spin-polarized electronic transport through double-island structures [38, 40, 92, 99, 124]. A typical double-island device, shown schematically in figure 8, consists of two metallic islands separated from each other and from external reservoirs by tunnel barriers. A gate voltage is additionally

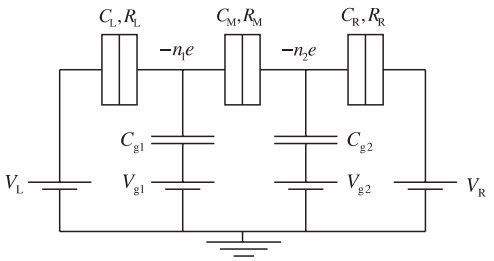

Figure 8. Schematic of a double-island device. The first (1) and second (2) islands are capacitively coupled to two gate voltages, V_{g1} and V_{g2}, and separated from each other and from the left and right electrodes by tunnel barriers.

attached capacitively to each island. Generally, both islands and external electrodes can be either magnetic or nonmagnetic [25, 38, 125]. In the following, we consider the situations when at least two electrodes (external or central) are ferromagnetic, and their magnetic moments form only collinear (parallel and antiparallel) configurations. Apart from this, we limit discussion to continuous density of states in the islands.

The Hamiltonian of the double-island systems is similar to that used for single-island devices, but now the electrostatic energy is given by [124, 126]

$$H_{ch} = E_{C_1}\left(n_1 - \frac{Q_{g1}}{e}\right)^2 + E_{C_2}\left(n_2 - \frac{Q_{g2}}{e}\right)^2 + 2E_{C_M}\left(n_1 - \frac{Q_{g1}}{e}\right)\left(n_2 - \frac{Q_{g2}}{e}\right), \tag{20}$$

where $n_{1(2)}$ is the number of excess electrons on the first (second) island and $Q_{g1(g2)}$ describes the respective charge induced by applied voltages, $Q_{g1(g2)} = C_{L(R)}V_{L(R)} + C_{g1(g2)}V_{g1(g2)}$. Apart from this, E_{C_1} and E_{C_2} denote the charging energies of the corresponding islands, whereas E_{C_M} describes electrostatic coupling of the islands,

$$E_{C_1(C_2)} = \frac{e^2}{2C_{1(2)}}\left(1 - \frac{C_M^2}{C_1C_2}\right)^{-1}, \tag{21}$$

$$E_{C_M} = \frac{e^2}{2C_M}\left(\frac{C_1C_2}{C_M^2} - 1\right)^{-1}, \tag{22}$$

with $C_{1(2)}$ being the total capacitance of the first (second) island, $C_{1(2)} = C_{L(R)} + C_{g1(g2)} + C_M$, and C_M denoting the capacitance of the middle junction.

To find the stationary current flowing through the system one then needs to know the probabilities $P(n_1, n_2, V)$ of finding the system in the charge state with n_1 and n_2 additional electrons on the first and second islands, respectively, when a bias voltage V is applied. These probabilities can be calculated in a recursive way from the following steady-state master equation

$$0 = -\sum_\sigma \left[\Gamma_{L1}^\sigma(n_1, n_2) + \Gamma_{1L}^\sigma(n_1, n_2) + \Gamma_{12}^\sigma(n_1, n_2) + \Gamma_{21}^\sigma(n_1, n_2) + \Gamma_{2R}^\sigma(n_1, n_2) + \Gamma_{R2}^\sigma(n_1, n_2)\right]P(n_1, n_2, V) + \sum_\sigma \Gamma_{L1}^\sigma(n_1 - 1, n_2)P(n_1 - 1, n_2, V)$$

$$+\sum_{\sigma}\Gamma^{\sigma}_{1\mathrm{L}}(n_1+1,n_2)P(n_1+1,n_2,V)$$
$$+\sum_{\sigma}\Gamma^{\sigma}_{12}(n_1+1,n_2-1)P(n_1+1,n_2-1,V)$$
$$+\sum_{\sigma}\Gamma^{\sigma}_{21}(n_1-1,n_2+1)P(n_1-1,n_2+1,V)$$
$$+\sum_{\sigma}\Gamma^{\sigma}_{\mathrm{R}2}(n_1,n_2-1)P(n_1,n_2-1,V)$$
$$+\sum_{\sigma}\Gamma^{\sigma}_{2R}(n_1,n_2+1)P(n_1,n_2+1,V), \qquad (23)$$

with the normalization condition $\sum_{n_1,n_2}P(n_1,n_2,V)=1$. The corresponding transition rates are given by equation (10), with the respective changes in the total system electrostatic energy. For example for tunnelling from the first island to the second one, the change in the electrostatic energy can be written as

$$\Delta E^{\sigma}_{12}(n_1,n_2)=E(n_1-1,n_2+1)-E(n_1,n_2)-\Delta E^{\sigma}_{\mathrm{F}1}+\Delta E^{\sigma}_{\mathrm{F}2}. \qquad (24)$$

Here, $\Delta E^{\sigma}_{\mathrm{F}1}$ and $\Delta E^{\sigma}_{\mathrm{F}2}$ denote the corresponding shifts of the chemical potentials for spin σ in the first and second islands, respectively. The spin asymmetry of tunnelling through the barrier r will be characterized in this section by the asymmetry factor α_r, defined as $\alpha_r = R_{r\uparrow}/R_{r\downarrow}$. This asymmetry factor corresponds to the ratio of the respective spin-dependent densities of states. In particular, for FM/NM junctions it is given by $\alpha=\rho_{\downarrow}/\rho_{\uparrow}$ and for FM/FM junctions by $\alpha=\rho^2_{\downarrow}/\rho^2_{\uparrow}$, provided that the two ferromagnetic electrodes are built of the same material. We note that the relation between spin-dependent barrier resistances in the parallel and antiparallel configurations of magnetic moments on the opposite sides of the barrier is the same as that described in section 2. When a bias voltage is applied to the system, a nonequilibrium spin accumulation may appear on the islands. Generally, the shifts of the Fermi level for both spin orientations are different. However, one can assume that the ratio of the Fermi level shifts for the spin-up and spin-down electrons, defined as $\beta_j=-\Delta E^{\uparrow}_{\mathrm{F}j}/\Delta E^{\downarrow}_{\mathrm{F}j}$, fulfils the relation $\beta_j=\rho_{\mathrm{I}j\uparrow}/\rho_{\mathrm{I}j\downarrow}$, for the first ($j=1$) and second ($j=2$) island, respectively, with $\rho_{\mathrm{I}j\sigma}$ being the spin-dependent density of states of the jth island. As a consequence, for nonmagnetic islands one directly gets, $\beta_1=\beta_2=1$.

The electric current flowing through the system can be determined from the following formula:

$$I_{\mathrm{L}}=-e\sum_{\sigma}\sum_{n_1,n_2=-\infty}^{\infty}[\Gamma^{\sigma}_{\mathrm{L}1}(n_1,n_2)-\Gamma^{\sigma}_{1\mathrm{L}}(n_1,n_2)]P(n_1,n_2,V), \qquad (25)$$

which corresponds to the current flowing through the left junction, but $I_{\mathrm{L}}=I_{\mathrm{R}}\equiv I$ in the stationary state.

3.1. Fast spin relaxation: no spin accumulation

Consider first transport characteristics of a system built of two ferromagnetic islands and nonmagnetic external electrodes, as shown in figure 9. Different magnetic configurations of the system are specified in the inset of figure 9(c). When

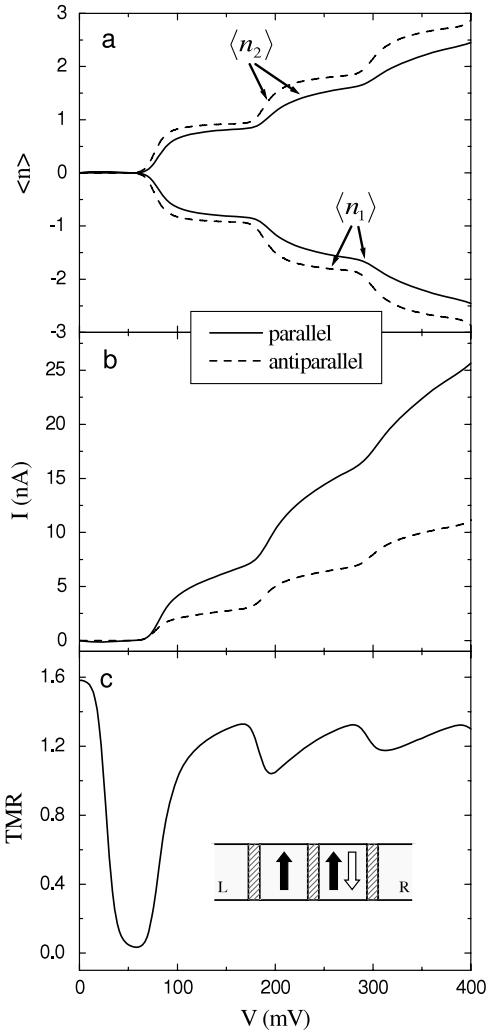

Figure 9. The average electron number on the islands (a), currents (b) in the parallel and antiparallel configurations and the resulting TMR (c) as a function of the bias voltage. The parameters are: $C_1=C_2\equiv C=3C_{\mathrm{M}}=3$ aF, $k_{\mathrm{B}}T/(e^2/2C)=0.05$. The spin asymmetries of resistances in the parallel configuration are $\alpha_{\mathrm{L}}=\alpha_{\mathrm{R}}=5$, $\alpha_{\mathrm{M}}=25$, whereas the total junction resistances are $R^{\mathrm{P}}_{\mathrm{L}}=R^{\mathrm{P}}_{\mathrm{R}}=R^{\mathrm{P}}_{\mathrm{M}}/10=1$ MΩ. In the antiparallel configuration, $R^{\mathrm{AP}}_{\mathrm{L}\sigma}=R^{\mathrm{P}}_{\mathrm{L}\sigma}$, $R^{\mathrm{AP}}_{\mathrm{M}\uparrow}=R^{\mathrm{AP}}_{\mathrm{M}\downarrow}=(R^{\mathrm{P}}_{\mathrm{M}\uparrow}R^{\mathrm{P}}_{\mathrm{M}\downarrow})^{1/2}$, and $R^{\mathrm{AP}}_{\mathrm{R}\sigma}=R^{\mathrm{P}}_{\mathrm{R}\bar{\sigma}}$.

the spin-relaxation time in the islands is much shorter than the time between two successive tunnelling events, no spin accumulation builds up on the islands. Since there is an asymmetry between the two barrier resistances, some charge accumulates on the islands, as displayed in figure 9(a). First of all, the magnitude of excess charge on the islands increases with increasing voltage. For the barrier asymmetry assumed in figure 9, the electrons tunnel more easily to the second island from the right lead than out of the second island to the first one. As a consequence, the electrons accumulate on the second island. On the other hand, the electrons more easily tunnel out of the first island to the left lead than from the second island to the first one. Thus, the number of excess electrons on the first island decreases with increasing bias voltage—holes are accumulated on the first island. This occurs in both magnetic configurations. The electric current flowing through

the system in the parallel and antiparallel configurations is shown in figure 9(b). The Coulomb steps due to discrete charging are clearly evident, and the difference in currents flowing in the parallel and antiparallel configurations gives rise to the tunnel magnetoresistance, shown in figure 9(c). The TMR effect oscillates as a function of the bias voltage and the amplitude of these oscillations decreases as the voltage is increased in a similar way as in the case of single-island FM SETs, see figure 3(b). Moreover, some dips now occur in the TMR at the voltages corresponding to the steps in the current–voltage characteristics.

3.2. Slow spin relaxation: spin accumulation

When the spin-relaxation time is longer than the time between two successive tunnelling events, a nonequilibrium magnetic moment appears on each island. The corresponding shifts of the Fermi level due to spin accumulation can be calculated from spin current conservation, see equation (13), written for each island [124].

Figure 10 shows the shifts of the Fermi levels and currents in the parallel and antiparallel configurations, as well as the resulting TMR calculated in the limit of long spin-relaxation time for the system built of ferromagnetic electrodes and nonmagnetic islands. The magnetic moments of external electrodes can form either parallel or antiparallel configurations, as illustrated in the inset of figure 10(c). First of all, the nonequilibrium spin accumulation, shown in figure 10(a), exists not only in the antiparallel configuration but also in the parallel one. In the antiparallel configuration the shifts of the Fermi level for a given spin orientation are equal on both islands, whereas in the parallel configuration they are opposite. The effects due to discrete charging lead to an oscillatory behaviour of the Fermi level shift, in a similar way to in the case of single-island FM SETs with nonmagnetic islands discussed above. The currents flowing through the system in both magnetic configurations are shown in figure 10(b). Due to nonequilibrium spin accumulation induced on the islands, these currents are different, which leads to nonzero tunnel magnetoresistance, as displayed in figure 10(c). It is interesting to note, that TMR now changes sign in certain transport voltage regions. These effects are clearly due to magnetic moments accumulated on the islands. If the spin-relaxation time becomes shorter than the time between successive tunnelling events, spin accumulation disappears and, consequently, TMR also vanishes.

Recently, several experiments on spin-polarized transport through granular systems have been reported [37, 38, 40, 92, 99]. For example, in [92], the tunnelling current was driven from a tip of scanning tunnelling microscope through ferromagnetic grains to a ferromagnetic electrode. Transport measurements of such devices showed pronounced Coulomb steps in the current–voltage characteristics. Moreover, negative differential conductance was observed. It was further proposed that the negative differential conductance could be a consequence of a nonequilibrium spin accumulation. Such systems can be modelled theoretically by double-island devices whose two islands and the right electrode are ferromagnetic,

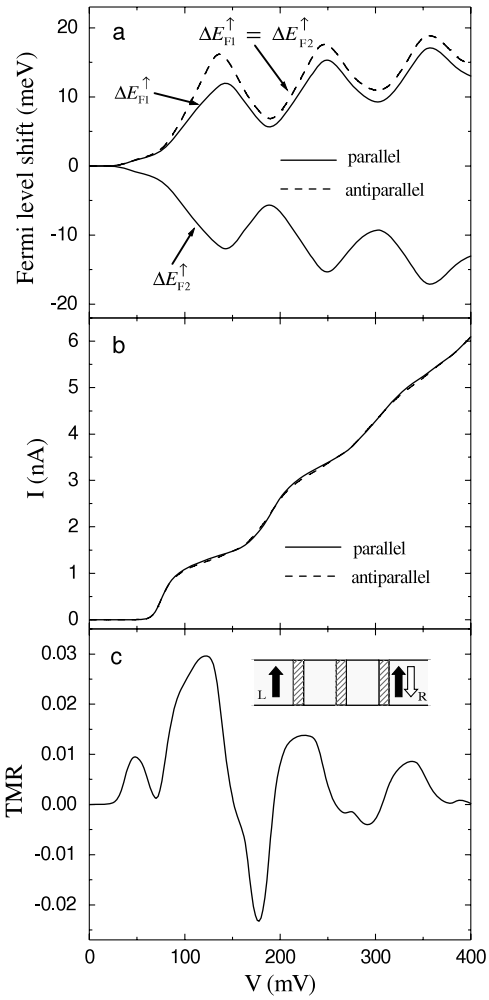

Figure 10. The shifts of the Fermi levels for spin-up electrons (a), currents in the parallel and antiparallel configurations (b) and TMR (c) as a function of the bias voltage. The parameters are: $C_1 = C_2 \equiv C = 3C_M = 3$ aF, $k_BT/(e^2/2C) = 0.05$, $\beta_1 = \beta_2 = 1$, $\tau_{sf1} \to \infty$, $\tau_{sf2} = \to \infty$, $\alpha_L = \alpha_R = 5$, $\alpha_M = 1$, whereas $R_L^P = R_R^P = R_M^P/50 = 1$ MΩ. In the antiparallel configuration, $R_{L\sigma}^{AP} = R_{L\sigma}^{P}$, $R_{R\sigma}^{AP} = R_{R\bar{\sigma}}^{P}$.

whereas the left electrode is nonmagnetic, corresponding to the nonmagnetic tip of scanning tunnelling microscope, see the inset of figure 11(c). Transport characteristics of such a device are displayed in figure 11 for the parameters taken from [92]. The shifts of the Fermi level for spin-up electrons are shown in figure 11(a). These shifts are different in both magnetic configurations. Generally, spin accumulation on the first island is larger than the accumulation on the second island. The reason for this is the fact that the rate for electron tunnelling from the first island to the left lead is smaller than the rate for tunnelling of electrons to or from the second island, which is due to asymmetry of barriers. The currents flowing through the system in the parallel and antiparallel configurations are illustrated in figure 11(b). Moreover, negative differential conductance occurs in both magnetic configurations, however, it is more pronounced in the antiparallel configuration, as shown in figure 11(c). It can be seen that negative differential conductance increases with increasing bias voltage. The

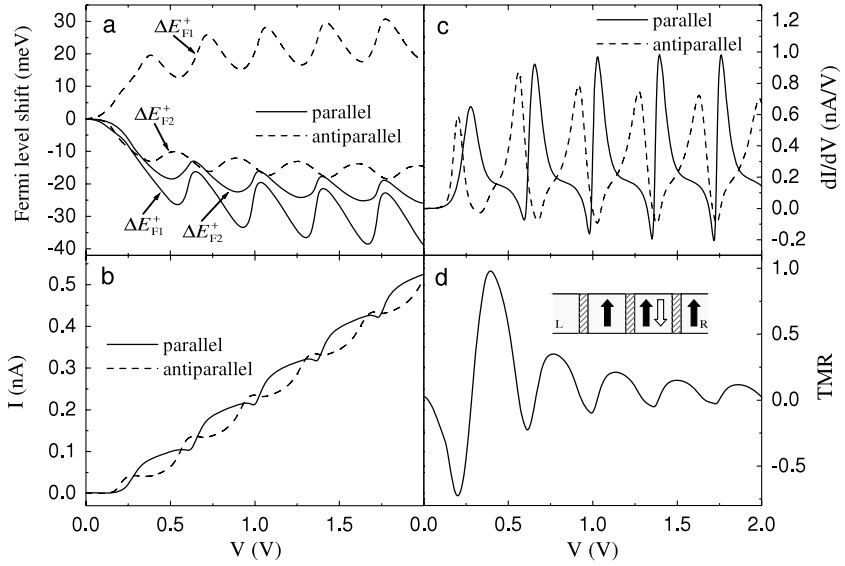

Figure 11. The shifts of the Fermi levels for majority-spin electrons (a), currents (b) and differential conductance (c) in the parallel and antiparallel configurations, and the resulting TMR (d) as a function of the bias voltage. The parameters are: $T = 140$ K, $C_L = 0.45$ aF, $C_M = 0.2$ aF, $C_R = 0.35$ aF, $C_{g1} = C_{g2} = 0$, $\alpha_L^2 = \alpha_M = \alpha_R = 25$, and $\beta_1 = \beta_2 = 0.2$, whereas $\tau_{sf1} = \tau_{sf2} = \infty$. The total junction resistances are $R_L = 3500$ MΩ, $R_M = R_R = 1$ MΩ. In the antiparallel configuration, $R_{L\sigma}^{AP} = R_{L\sigma}^{P}$, and $R_{r\uparrow}^{AP} = R_{r\downarrow}^{AP} = (R_{r\uparrow}^{P} R_{r\downarrow}^{P})^{1/2}$, for $r = M, R$. Reprinted figure with permission from [124]. Copyright 2006 by the American Physical Society.

resulting TMR effect is displayed in figure 11(d). It is interesting to note that TMR oscillates between negative and positive values.

Oscillations of the sign of TMR and differential conductance result from spin accumulations in both islands and are absent in the limit of fast spin relaxation (no spin accumulation) in the islands. The results presented in figure 11 correspond to the long spin-relaxation limit. In such a limit, some spin accumulation may occur even for a very small current flowing through the system, giving rise to NDC and oscillations of the TMR sign for small bias voltages. However, both effects disappear when the spin-relaxation time is shorter than the time between successive tunnelling events. Thus, for a finite relaxation time, one may expect absence of NDC and TMR oscillations for small voltages and the onset of these effects at larger voltages. This is because at some voltage there is a crossover from the fast to slow spin-relaxation limits. In fact such a behaviour is consistent with the experimental data of [92].

The disappearance of NDC with decreasing spin-relaxation time τ_{sf} is shown explicitly in figure 12, where the bias dependence of differential conductance is presented for different values of the spin-relaxation time. This figure clearly shows that NDC disappears when spin-relaxation time decreases, in agreement with the above discussion. In the limit of fast spin-relaxation time, the differential conductance is positive, although its periodic modulation still remains.

Similarly, periodic oscillations of the sign of TMR also disappear with decreasing spin-relaxation time τ_{sf}. This behaviour is shown in figure 13, where the bias dependence of TMR is shown for several values of τ_{sf}. First, the transitions to negative TMR disappear with decreasing τ_{sf}. The TMR becomes then positive, although some periodic modulations

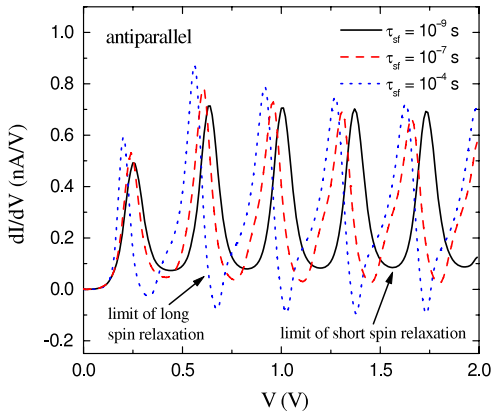

Figure 12. Differential conductance in the antiparallel configuration as a function of the bias voltage calculated for different values of the spin-relaxation time $\tau_{sf1} = \tau_{sf2} = \tau_{sf}$ and for $\rho_{I1}^{+}\Omega_{I1} = \rho_{I2}^{+}\Omega_{I2} = 1000\ \mathrm{eV}^{-1}$. The other parameters as well as magnetic configuration of the system are the same as in figure 11. Reprinted figure with permission from [124]. Copyright 2006 by the American Physical Society.

survive. Second, the phase of the modulations shifts by about π when the spin relaxation varies from fast to slow limits.

In the case of the systems analysed, the negative differential conductance occurs due to nonequilibrium spin accumulation on the islands. However, it is worth noting that negative differential conductance may also exist in single-electron devices built of nonmagnetic materials [127, 128].

4. Spin-polarized transport through single-level quantum dots connected to ferromagnetic leads

In the previous two sections we considered spin-dependent transport through single-electron devices, whose central

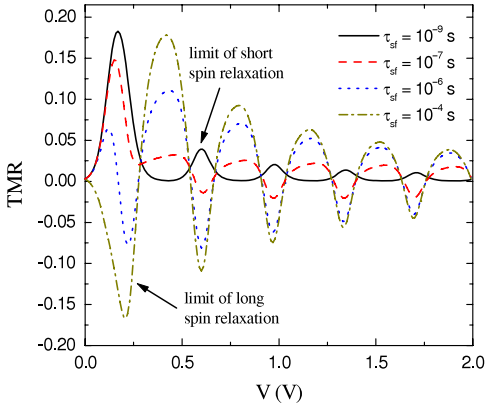

Figure 13. TMR as a function of the bias voltage calculated for different values of spin-relaxation time $\tau_{sf1} = \tau_{sf2} = \tau_{sf}$ and for $\rho_{l1}^{+}\Omega_{l1} = \rho_{l2}^{+}\Omega_{l2} = 1000\ \mathrm{eV}^{-1}$. The other parameters as well as magnetic configuration of the system are the same as in figure 11. Reprinted figure with permission from [124]. Copyright 2006 by the American Physical Society.

electrodes (islands) were described by continuous (or discrete with small level separation) energy spectrum, and the most relevant and dominant energy scale was the electrostatic charging energy. In ultra-small metallic islands (nanoparticles) or in semiconducting quantum dots, the level spacing is comparable with the charging energy or even larger. This also happens in the case of a molecule attached to metallic leads. In this limit one arrives at slightly more sophisticated single-electron devices [18, 129, 130].

In this section we consider a FM SET based on a semiconductor quantum dot coupled to ferromagnetic leads. This model also applies to molecules attached to ferromagnetic electrodes. Single-electron transistors based on quantum dots are of current interest not only because of the new and interesting physics emerging in those systems, but, more importantly, due to possible future applications and due to the possibility of manipulation of a single-electron charge and a single-electron spin [18, 41, 131, 132]. Furthermore, quantum dots are also interesting for future applications in quantum computing [133, 134].

Transport properties of quantum dots coupled to nonmagnetic leads have already been extensively studied both theoretically and experimentally [18, 66, 71, 72, 131, 132, 135, 136]. However, further interesting effects occur in the case of quantum dots coupled to ferromagnetic leads, e.g. spin accumulation, parity effect on tunnel magnetoresistance, zero-bias anomaly in the Coulomb blockade regime, exchange field, splitting of the Kondo anomaly, and others. Most of the works concerned the theoretical description of spin-polarized transport in the weak coupling regime, as well as in the strong coupling regime, where the Kondo physics emerges [137–145]. Sequential transport through a single-level quantum dot coupled to ferromagnetic leads was studied for both collinear [146, 147] and noncollinear [148–153] configurations of the electrodes' magnetic moments. Spin-polarized transport in the cotunnelling regime has also been addressed for collinear systems [154–157], as well as for systems magnetized noncollinearly [158–161]. Furthermore, resonant tunnelling was also considered [142, 162].

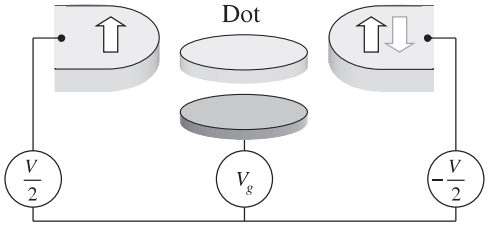

Figure 14. Schematic of a quantum dot coupled to ferromagnetic leads. The magnetic moments of external electrodes can be aligned either in parallel or antiparallel. The system is symmetrically biased and there is a gate voltage attached to the dot.

Quantum dots coupled to ferromagnetic leads may be realized experimentally in various ways, including ultra-small metallic (e.g. aluminium) nanoparticles [41], single molecules [51], granular structures [163], self-assembled dots in ferromagnetic semiconductors [46], carbon nanotubes [52–62], and magnetic tunnel junctions [49]. Quite recently, semiconductor quantum dots based on a two-dimensional electron gas were successfully attached to ferromagnetic leads [42–45].

4.1. Quantum dots weakly coupled to ferromagnetic leads: collinear magnetizations

Let us begin our discussion with the case when the dot is weakly coupled to the leads. One can then use a perturbative approach in which the coupling is considered as a small perturbation to the unperturbed quantum dot and the leads. Transport is then dominated either by the first-order or by the second-order (cotunnelling) contributions. Later on we consider a more general situation where the coupling may be strong and a new Kondo physics emerges at low temperatures.

4.1.1. Model and method. A schematic of a quantum dot coupled to ferromagnetic leads is presented in figure 14. The magnetizations of the leads can be either parallel or antiparallel. There is also a gate voltage attached to the dot. The system is modelled by an Anderson-like Hamiltonian of the general form [164]

$$H = H_{\mathrm{L}} + H_{\mathrm{R}} + H_{\mathrm{D}} + H_{\mathrm{T}}, \tag{26}$$

where the first and second terms describe the left and right reservoirs of noninteracting electrons, $H_r = \sum_{\mathbf{q}\sigma} \varepsilon_{r\mathbf{q}\sigma} c^{\dagger}_{r\mathbf{q}\sigma} c_{r\mathbf{q}\sigma}$ for $r = \mathrm{L}, \mathrm{R}$ (see equation (7)). The third term of the Hamiltonian, H_{D}, represents the dot and includes two components: one describes noninteracting electrons in the dot level and the other represents the Coulomb interaction of two electrons residing in this level,

$$H_{\mathrm{D}} = \sum_{\sigma=\uparrow,\downarrow} \varepsilon_{\sigma} d^{\dagger}_{\sigma} d_{\sigma} + U d^{\dagger}_{\uparrow} d_{\uparrow} d^{\dagger}_{\downarrow} d_{\downarrow}, \tag{27}$$

where U is the correlation energy, $\varepsilon_{\sigma} = \varepsilon \mp \Delta/2$ is the energy of an electron in the dot with spin σ, and $d^{\dagger}_{\sigma}$ (d_{σ}) is the corresponding creation (annihilation) operator. The position of the dot level can be tuned by the gate voltage, but

is independent of the symmetrically applied transport voltage. Generally, the dot level may be spin-split, for example due to a stray field of the electrodes or due to an external magnetic field. The corresponding level splitting is denoted by Δ, whereas ε is the energy of the spin-degenerate dot level. In general, four different states of the dot are possible: empty dot ($\chi = 0$), singly occupied dot with a spin-up ($\chi = \uparrow$) or spin-down ($\chi = \downarrow$) electron, and doubly occupied dot ($\chi = \mathrm{d}$), where $|\chi\rangle$ are the corresponding eigenfunctions.

The interaction between the leads and the quantum dot is incorporated in the tunnelling Hamiltonian, H_T, given by

$$H_\mathrm{T} = \sum_{r=\mathrm{L,R}} \sum_{\mathbf{q}\sigma} \left(t_{r\mathbf{q}\sigma} c^\dagger_{r\mathbf{q}\sigma} d_\sigma + t^*_{r\mathbf{q}\sigma} d^\dagger_\sigma c_{r\mathbf{q}\sigma} \right), \tag{28}$$

where $t_{r\mathbf{q}\sigma}$ are the tunnel matrix elements. Tunnelling gives rise to an intrinsic broadening Γ^σ of the dot levels, $\Gamma^\sigma = \sum_{r=\mathrm{L,R}} \Gamma^\sigma_r$. The parameters $\Gamma^\uparrow_r$ and $\Gamma^\downarrow_r$ describe contributions to the level widths due to coupling of the dot to the lead r. The respective contribution Γ^σ_r can be expressed in terms of the Fermi golden rule as $\Gamma^\sigma_r = 2\pi \sum_\mathbf{q} |t_{r\mathbf{q}\sigma}|^2 \delta(\omega - \varepsilon_{r\mathbf{q}\sigma})$. Assuming the tunnel matrix elements $t_{r\mathbf{q}\sigma}$ to be independent of the wavevector $\mathbf{q}$, one can write

$$\Gamma^\sigma_r = 2\pi |t_{r\sigma}|^2 \rho_{r\sigma}. \tag{29}$$

The coupling parameters are usually expressed in terms of the spin polarization p_r of the lead r, defined by equation (2), as $\Gamma^{\uparrow(\downarrow)}_r = \Gamma_r(1 \pm p_r)$, where $\Gamma_r = (\Gamma^\uparrow_r + \Gamma^\downarrow_r)/2$. As reported in [165], typical values of the dot-lead coupling strength Γ in the weak coupling regime are of the order of tens of μeV.

In order to investigate transport properties of the system in the whole range of parameters, one has to use a method which is more sophisticated than that based on the Fermi golden rule. Two such techniques are commonly used: the method based on the equation of motion for the electron Green functions, and the real-time diagrammatic technique. Discussion in this section is based mainly on the latter one [104, 166–170]. This technique is based on a systematic perturbation expansion of the expectation value of the current operator and the density matrix order by order in the dot-lead coupling strength Γ. Even, if we limit further considerations based on this technique to the second-order processes, this allows us to describe transport in the resonance regime, where the usual second-order perturbation term diverges. One also could go beyond the second-order theory and describe more subtle effects.

Within the real-time diagrammatic technique, the density matrix elements of the quantum dot, $P^{\chi_1}_{\chi_2}$, are given by a kinetic equation in the Liouville space

$$0 = (\varepsilon_{\chi_1} - \varepsilon_{\chi_2}) P^{\chi_1}_{\chi_2} + \sum_{\chi'_1\chi'_2} \Sigma^{\chi_1\chi'_1}_{\chi_2\chi'_2} P^{\chi'_1}_{\chi'_2}, \tag{30}$$

where $\Sigma^{\chi'_1\chi_1}_{\chi'_2\chi_2}$ is the irreducible self-energy corresponding to transition forward in time from state $|\chi'_1\rangle$ to $|\chi_1\rangle$ and then backward in time from state $|\chi_2\rangle$ to $|\chi'_2\rangle$.

When the tunnelling processes are spin-conserving and magnetic moments of the leads are collinear, the density matrix is diagonal. After performing the perturbation expansion, one gets the following first-order (sequential tunnelling) and second-order (cotunnelling) master equations:

$$0 = \sum_\chi \Sigma^{(1)}_{\chi'\chi} P^{(0)}_\chi, \tag{31}$$

$$0 = \sum_\chi \Sigma^{(2)}_{\chi'\chi} P^{(0)}_\chi + \Sigma^{(1)}_{\chi'\chi} P^{(1)}_\chi, \tag{32}$$

respectively, where the probabilities obey the normalization condition $\sum_\chi P^{(m)}_\chi = \delta_{m,0}$.

Systematic perturbation expansion of electric current with respect to the coupling strength Γ can be performed in a similar way, and the first-order and second-order contributions to current are given by the expressions [166, 169]

$$I^{(1)} = -\frac{\mathrm{i}e}{2\hbar} \sum_{\chi\chi'} \Sigma^{\mathrm{I}(1)}_{\chi'\chi} P^{(0)}_\chi, \tag{33}$$

$$I^{(2)} = -\frac{\mathrm{i}e}{2\hbar} \sum_{\chi\chi'} \Sigma^{\mathrm{I}(2)}_{\chi'\chi} P^{(0)}_\chi + \Sigma^{\mathrm{I}(1)}_{\chi'\chi} P^{(1)}_\chi, \tag{34}$$

where the coefficients $\Sigma^{\mathrm{I}(1)}_{\chi'\chi}$ and $\Sigma^{\mathrm{I}(2)}_{\chi'\chi}$ are the first- and second-order self-energies, modified as compared to $\Sigma^{(\mathrm{m})}_{\chi'\chi}$, to account for the number of electrons transferred through the barriers [156].

Transport characteristics of quantum dots are generally studied in both the linear and nonlinear response regimes [156]. It is thus important to distinguish between different transport regimes of quantum dots, which are sketched in figure 15 and labelled by the corresponding capital letters.

First of all, by changing the position of the dot level (by the gate voltage for instance) or applying the bias voltage, one can cross over from one regime to another. The three regions (A, B and A′) around zero bias correspond to the regime where sequential tunnelling is exponentially suppressed and current flows mainly due to cotunnelling. The charge state of the dot is then fixed (strictly at zero temperature) to zero electrons in the regime A, one electron in the regime B, and two electrons in the regime A′. The first-order tunnelling processes are possible once the bias voltage is increased above the threshold voltage, allowing for finite occupation of two adjacent charge states (zero and one for regime C, and one and two for regime C′).

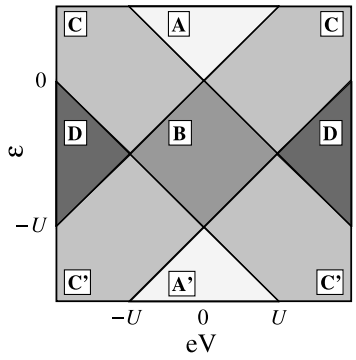

Figure 15. A sketch illustrating different transport regimes. The respective regimes are separated by solid lines and labelled correspondingly.

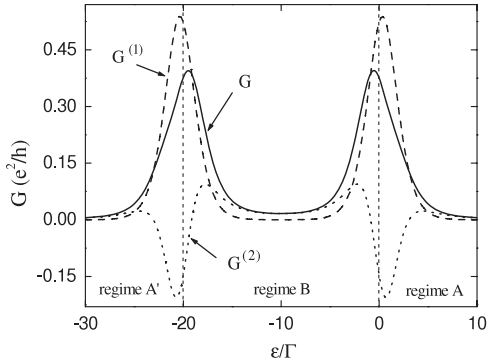

Figure 16. Linear conductance as a function of the level position. The dashed line corresponds to the first-order contribution $G^{(1)}$, the dotted line presents the second-order conductance $G^{(2)}$ and the solid line shows the sum $G^{(1)} + G^{(2)}$. The different transport regimes are also specified. The parameters are: $k_BT = \Gamma$, $U = 20\Gamma$, and $p = 0$. Reprinted with permission from [156]. Copyright 2005 by the American Physical Society.

In the regime D all four dot states $\chi = 0, \uparrow, \downarrow, \mathrm{d}$ are possible. By performing a particle–hole transformation, the behaviour in regime A′ and C′ can be mapped to that in regime A and C, respectively.

4.1.2. Case of nonmagnetic leads. To discuss the role of second-order processes we first briefly describe the case of a quantum dot coupled to nonmagnetic leads ($p_L = p_R = 0$). Figure 16 shows the first-order (dashed line) and second-order (dotted line) contributions to the linear conductance as well as the total conductance (solid line). The conductance is shown there as a function of the dot's level energy. When the dot level crosses the Fermi level of electrodes, there is a resonance peak in the linear conductance. Another resonance appears when $\varepsilon + U$ crosses the Fermi level. The resonance peaks acquire a certain width as a result of the level broadening due to coupling to the leads (thermal fluctuations also contribute). It is interesting to note, that the second-order contribution becomes negative at resonances, which indicates that the second-order processes renormalize the first-order (sequential) contribution. Except for resonances, the dot is either in the empty (regime A) or doubly occupied (regime A′) state, or in the Coulomb blockade regime (regime B). In all these three cases the cotunnelling contribution to electric current becomes dominant. It is also worth noting, that the second-order processes lead to renormalization of the dot level energy [166].

4.1.3. Case of ferromagnetic leads. When the external electrodes are ferromagnetic, qualitatively new features appear in the transport characteristics. These are particularly pronounced in the tunnel magnetoresistance, defined by equation (1). Below we describe some of them.

Tunnel magnetoresistance calculated in the first order of the dot-lead coupling strength Γ (sequential transport limit) is shown in figure 17(a) as a function of the bias and gate voltages. It is evident that then the TMR generally acquires two different values, depending on the transport region. For the regions A (and A′), B and D, the TMR value is

$$\mathrm{TMR}^{\mathrm{A,B,D}}_{\mathrm{seq}} = \frac{p^2}{1-p^2} = \frac{1}{2}\mathrm{TMR}^{\mathrm{Jull}}, \tag{35}$$

while for the region C (and C′) it is

$$\mathrm{TMR}^{\mathrm{C}}_{\mathrm{seq}} = \frac{4p^2}{3(1-p^2)} = \frac{2}{3}\mathrm{TMR}^{\mathrm{Jull}}. \tag{36}$$

This behaviour can be accounted for as follows. For the regions A (A′) and B the first-order linear conductance in the parallel and antiparallel configurations is

$$G^{(1)}_{\mathrm{P}} \sim \Gamma/2 \qquad \text{and} \qquad G^{(1)}_{\mathrm{AP}} \sim \Gamma(1-p^2)/2, \tag{37}$$

which leads to a magnetoresistance equal to $\mathrm{TMR} = \mathrm{TMR}^{\mathrm{A,B}}_{\mathrm{seq}} = p^2/(1-p^2)$. To account for the behaviour of TMR in the regions C and D let us consider the zero temperature limit. In the region C there are then three dot states taking part in transport: $\chi = 0, \uparrow, \downarrow$ (because of the particle–hole symmetry, the results are also applicable to regime C′). One then finds the first-order currents in the parallel and antiparallel configurations to be $I^{(1)}_{\mathrm{P}} \sim \Gamma/3$ and $I^{(1)}_{\mathrm{AP}} \sim \Gamma(1-p^2)/(3+p^2)$, which leads to $\mathrm{TMR}^{\mathrm{C}}_{\mathrm{seq}} = 4p^2/3(1-p^2)$. A similar analysis for the region D gives $\mathrm{TMR}^{\mathrm{D}}_{\mathrm{seq}} = p^2/(1-p^2)$.

As we already know from previous sections, first-order (sequential) transport does not properly describe the blockade regions (the regions A, A′ and B). Transport in these regions is expected to be strongly modified by the second-order

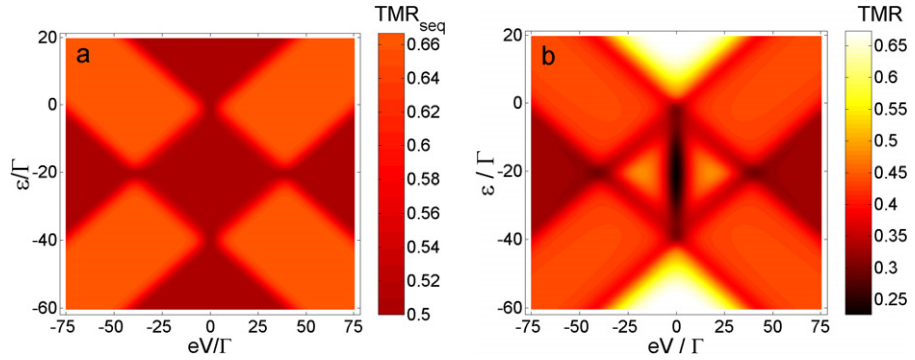

Figure 17. The first-order (a) and first-plus second-order (b) tunnel magnetoresistance as a function of the bias and gate voltages for the parameters: $k_BT = 1.5\Gamma$, $U = 40\Gamma$, and $p = 0.5$. Reprinted with permission from [156]. Copyright 2005 by the American Physical Society.

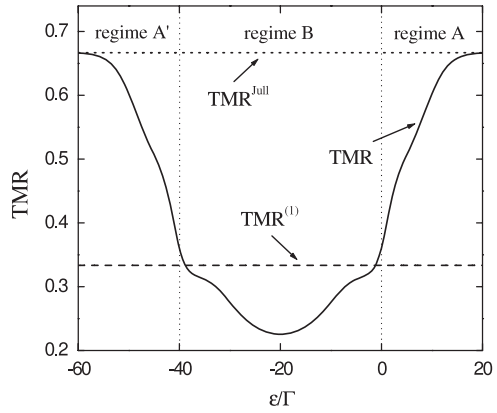

Figure 18. The total linear tunnel magnetoresistance (solid line) as a function of the level position. The dashed line represents the first-order tunnel magnetoresistance, whereas the dotted line corresponds to Jullière's value. The parameters are $k_BT = 1.5\Gamma$, $U = 40\Gamma$, and $p = 0.5$. Reprinted with permission from [156]. Copyright 2005 by the American Physical Society.

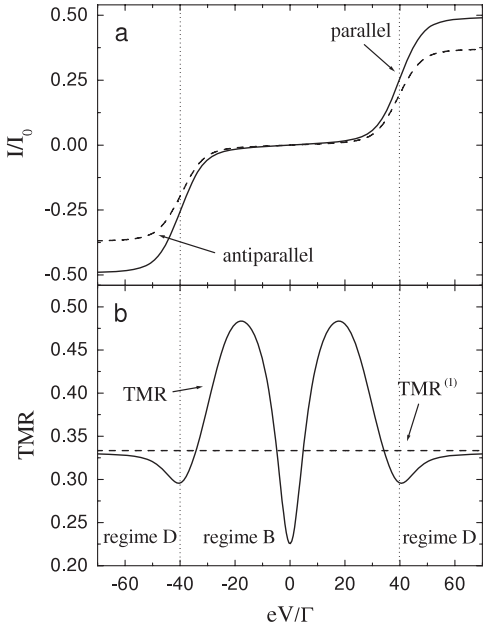

Figure 19. The total current (a) in the parallel (solid line) and antiparallel (dashed line) magnetic configurations as a function of the bias voltage in units of $I_0 = e\Gamma/\hbar$. Part (b) shows the first-order contribution to the TMR (dashed line) and the total TMR (solid line). The parameters are: $k_BT = 1.5\Gamma$, $\varepsilon = -20\Gamma$, $U = 40\Gamma$, and $p = 0.5$. Reprinted with permission from [156]. Copyright 2005 by the American Physical Society.

(cotunnelling) processes. Accordingly, the above picture is also strongly modified. The corresponding TMR is displayed in figure 17(b). Since the sequential tunnelling dominates transport above the threshold voltage (outside the blockade regions, i.e. in the regions C and D), the total TMR is only slightly modified there as compared to that in the first order. In the regions A, A′ and B, however, the first-order tunnelling processes are exponentially suppressed and the current is dominated by the second-order (cotunnelling) processes. As follows from figure 17(b), cotunnelling then has a significant influence on TMR. Apart from this, TMR in the regions A and A′ behaves differently from that in the region B.

Let us look now in more detail at the vertical cross-section of figure 17(b) along the zero bias (linear response). The corresponding linear TMR as a function of the level position (gate voltage) is shown in figure 18. By changing the position of the dot level, one crosses over from regime A through regime B to regime A′. For comparison, the Jullière's value of TMR, as well as the first-order contribution to TMR (denoted as $\mathrm{TMR}^{(1)}$) are shown there. Note, that the first-order TMR is independent of the gate voltage and is equal to a half of Jullière's value. First of all, one can note that the second-order processes modify the TMR substantially. Unlike the first-order term, the total TMR (first-order plus second-order contributions) does depend on the level position. The interesting feature of TMR shown in figure 18 is a strong parity effect. The TMR reaches a maximum when there is an even number of electrons on the dot (zero for the regime A or two for the regime A′), and has minimum for an odd (one in the regime B) number of electrons. A universal feature is that for an even electron number, TMR exactly coincides with Jullière's value. The system then behaves like a single ferromagnetic tunnel junction. Such a situation can take place when tunnelling processes are coherent. The only second-order processes that contribute to conductance in these regions are the non-spin-flip cotunnelling processes, in which the electron spin is conserved. Such processes indeed are fully coherent. The corresponding cotunnelling rates are proportional to the product of the density of states of the left and right leads, thus, one can express the second-order linear conductance as

$$G_{\mathrm{P}}^{(2)} \sim \frac{\Gamma^2}{2}(1+p^2) \qquad \text{and} \qquad G_{\mathrm{AP}}^{(2)} \sim \frac{\Gamma^2}{2}(1-p^2), \quad (38)$$

for the parallel and antiparallel configuration, respectively. As a consequence, the TMR is then equal to that of a single planar ferromagnetic tunnel junction

$$\mathrm{TMR}^{\mathrm{A}} = \frac{2p^2}{1-p^2} = \mathrm{TMR}^{\mathrm{Jull}}. \quad (39)$$

Because of the particle–hole symmetry, the same result can be obtained for regime A′.

The situation becomes, however, more complex for an odd number of electrons on the dot. Apart from the non-spin-flip processes, there are also spin-flip cotunnelling processes that change the spin of the dot. Such second-order processes give rise to spin relaxation on the dot and lead to reduction of TMR in the regime B. The dependence of TMR on the position of the energy level in the regime B reflects the relation of the spin-flip to non-spin-flip cotunnelling processes. The minimum value of TMR appears for $\varepsilon = -U/2$, see figure 18, where one finds

$$\mathrm{TMR}^{\mathrm{B}}_{\mathrm{min}} = \frac{2p^2}{3(1-p^2)} = \frac{1}{3}\mathrm{TMR}^{\mathrm{Jull}}. \quad (40)$$

Electric current flowing through the system in the nonlinear response regime is shown in figure 19(a) for both magnetic configurations and for a symmetric Anderson model ($\varepsilon = -U/2$). The corresponding TMR is also shown

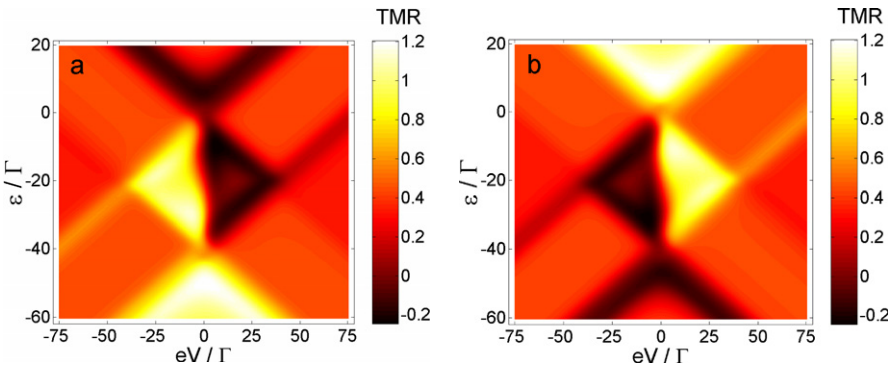

Figure 20. The total tunnel magnetoresistance as a function of the bias and gate voltages in the presence of an external magnetic field for (a) $\Delta = 4\Gamma$ and (b) $\Delta = -4\Gamma$. The parameters are: $k_BT = 1.5\Gamma$, $U = 40\Gamma$, and $p = 0.5$.

there, see figure 19(b). The contribution due to the second-order tunnelling processes is significant (or even dominant) in the Coulomb blockade regime. The sequential TMR is shown by a dashed line in figure 19(b). One can see that sequential TMR is constant as a function of the bias voltage. However, this is not a universal behaviour and occurs only for the symmetric Anderson model. Generally, first-order TMR depends on the applied bias voltage, as illustrated in figure 17(a). The second-order processes lead to a strong and nontrivial dependence of the total TMR on the bias voltage. For large values of the transport voltage (regime D), the first-order tunnelling processes dominate, and therefore the total TMR is only slightly modified as compared to that in the sequential transport regime. However, for voltages below the threshold voltage (regime B), the cotunnelling processes lead to a strong bias dependence of TMR in the Coulomb blockade regime, and to a deep minimum of TMR in the zero-bias limit. In the case of metallic islands, cotunnelling processes usually lead to an enhancement of the TMR effect in the Coulomb blockade regime [74]. Here, we have the opposite situation, i.e., suppression of the effect. At low bias voltage, $|eV| \ll k_BT$, the single-barrier spin-flip processes reduce the TMR. This is however no longer the case for nonlinear response regime, $|eV| \gg k_BT$, where the spin accumulation diminishes the amount of spin-flip processes and the TMR increases. Consequently, the TMR effect in regime B increases with rising bias voltage within the limits $\mathrm{TMR}^{\mathrm{Jull}}/3 \leqslant \mathrm{TMR}^{\mathrm{B}} \leqslant \mathrm{TMR}^{\mathrm{Jull}}$. The minimum value is reached at $V = 0$ and $\varepsilon = -U/2$, whereas the maximum value is approached for bias voltages large compared to the thermal energy but still far away from the onset of sequential tunnelling.

New features of transport characteristics appear when the spin degeneration of the dot level is lifted, $\varepsilon_\uparrow \neq \varepsilon_\downarrow$, e.g. due to an external magnetic field applied to the system. It turns out that a finite Zeeman splitting, $\Delta = \varepsilon_\downarrow - \varepsilon_\uparrow$, changes the transport characteristics substantially. Figure 20(a) illustrates the gate and bias voltage dependence of tunnel magnetoresistance for $\Delta = 4\Gamma$. First of all, a finite Zeeman splitting affects the TMR mainly in the regimes A (A′) and B, where the second-order processes dominate. Furthermore, TMR exhibits a distinctively different behaviour in the regions A and A′. It is enhanced in the case of an empty dot, and reduced in the case of a doubly occupied dot (it may even become negative in the latter case). This effect depends on the orientation of applied magnetic field; when the field is applied in the opposite direction, $\Delta = -4\Gamma$, there is an enhancement of TMR in regime A′ and suppression in regime A, as illustrated in figure 20(b). Thus, by changing the sign of the Zeeman splitting (magnetic field orientation) or applying a gate voltage, which changes the dot occupation, it is possible to reduce or enhance the TMR effect considerably. Another interesting feature of TMR displayed in figure 20(a) appears in the region B. There is a strong asymmetry of TMR with respect to the bias reversal. The TMR is decreased for positive and increased for negative bias voltage. This can also be seen in figure 20(b), but for positive transport voltage TMR is then larger than for negative bias voltage. The crossover between those two values of TMR takes place roughly at zero bias. As a consequence, by changing the bias voltage in a small range one can substantially tune the magnitude of the TMR effect.

4.2. Transport through quantum dots in the Coulomb blockade regime: collinear magnetizations

As we know from previous subsection, the most interesting features due to ferromagnetism of the electrodes, e.g. the zero-bias anomaly, occur in the blockade regime, where sequential tunnelling processes play a minor role. This anomaly appears only in the case when the dot is singly occupied at equilibrium ($\varepsilon_\sigma < 0$, $\varepsilon_\sigma + U > 0$) and the system is in a deep Coulomb blockade regime; $\Gamma, k_BT \ll |\varepsilon_\sigma|, \varepsilon_\sigma + U$. In such a case the sequential tunnelling is exponentially suppressed, and cotunnelling gives the dominant contribution to electric current [76, 155, 157, 171–173]. Therefore, the sequential tunnelling can be completely ignored. In this subsection we look more carefully at these features taking into account only the second-order contribution.

In order to calculate the cotunnelling current in the deep blockade regime one can employ a simplified second-order perturbation theory and master equation for the occupation probabilities. The rate of a cotunnelling process from lead r to lead r', which change the dot state from $|\chi\rangle$ to $|\chi'\rangle$, can be

written as

$$\gamma_{rr'}^{\chi\to\chi'} = \frac{2\pi}{\hbar}\left|\sum_{v}\frac{\langle\Phi_{r'}^{\chi'}|H_{\mathrm{T}}|\Phi_{\mathrm{v}}\rangle\langle\Phi_{\mathrm{v}}|H_{\mathrm{T}}|\Phi_{r}^{\chi}\rangle}{\varepsilon_i-\varepsilon_v}\right|^2\delta(\varepsilon_i-\varepsilon_f), \tag{41}$$

with ε_i and ε_f denoting the energies of initial and final states, $|\Phi_r^{\chi}\rangle$ being the state of the system with an electron in the lead r and the dot in state $|\chi\rangle$, whereas $|\Phi_{\mathrm{v}}\rangle$ is a virtual state with ε_v denoting the corresponding energy. Among different cotunnelling processes one can distinguish single-barrier ($r = r'$) and double-barrier ($r \neq r'$) cotunnelling as well as spin-flip ($\chi \neq \chi'$) and non-spin-flip ($\chi = \chi'$) cotunnelling. The spin-flip processes change the spin state of the dot, whereas the non-spin-flip processes do not change the dot state. The current flows through the system due to double-barrier cotunnelling processes. On the other hand, the single-barrier processes do not contribute directly to electric current, however, they can change the dot occupations, and this way also influence the current.

The cotunnelling current flowing through the system from the left to right lead is given by

$$I = -e\sum_{\chi\chi'}P_{\chi}\left[\gamma_{\mathrm{LR}}^{\chi\to\chi'}-\gamma_{\mathrm{RL}}^{\chi\to\chi'}\right], \tag{42}$$

where P_χ denotes the corresponding occupation probability. The probabilities P_χ can be found from the master equation,

$$0 = \sum_{rr'}\sum_{\chi'}\left[-\gamma_{rr'}^{\chi\to\chi'}P_{\chi}+\gamma_{rr'}^{\chi'\to\chi}P_{\chi'}\right], \tag{43}$$

together with the normalization condition $\sum_\chi P_\chi = 1$.

4.2.1. Zero-bias anomaly and its physical mechanism. In order to elucidate and understand the anomalous behaviour of TMR in the Coulomb blockade regime, we show in figure 21(a) the differential conductance in the small bias regime for both parallel and antiparallel configurations and for several temperatures. Figure 21(b) displays the corresponding TMR effect. First of all, the TMR effect in the regime B for $|eV| \gg k_{\mathrm{B}}T$ increases with lowering temperature and approaches Jullière's value, whereas the minimum at zero bias does not depend on temperature. The differential conductance in the parallel alignment has characteristics typical of the cotunnelling regime, with a smooth parabolic dependence on the bias voltage. For the antiparallel configuration, on the other hand, differential conductance has a local maximum at zero bias, followed by local minimum with increasing bias, as illustrated in figure 21(a). This zero-bias anomaly stems from the interplay of the spin-flip and non-spin-flip single-barrier and double-barrier cotunnelling processes [155]. The minimum in the TMR effect is a direct consequence of this anomalous behaviour of differential conductance in the antiparallel configuration.

The zero-bias anomaly in the cotunnelling regime is qualitatively similar to the anomaly due to the Kondo effect, which occurs in the strong coupling limit [174–176]. There are, however, some distinct differences. First of all, processes

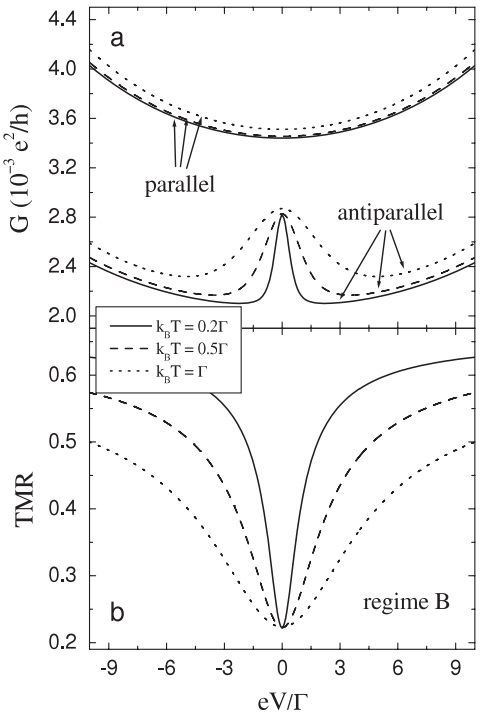

Figure 21. The differential conductance (a) for the parallel and antiparallel configurations and the tunnel magnetoresistance (b) as a function of the bias voltage for different values of temperature. The maximum in differential conductance for antiparallel configuration at zero bias is clearly demonstrated. The other parameters are the same as in figure 19. The figure was generated using the scheme for the perturbation expansion in the Coulomb blockade regime. Reprinted with permission from [156]. Copyright 2005 by the American Physical Society.

responsible for the zero-bias anomaly in the cotunnelling regime are of the second order in tunnelling processes, while these leading to the Kondo effect are of higher order. The conductance in the cotunnelling regime is much smaller than in the Kondo regime, where almost perfect transmission ($G = e^2/h$) through the dot is possible owing to the Kondo peak in the density of states at the Fermi level. Furthermore, the Kondo peak occurs at temperatures lower than the so-called Kondo temperature, $T \lesssim T_{\mathrm{K}}$, and exists also in the parallel configuration [51, 139].

To understand the mechanism of the zero-bias anomaly it is crucial to distinguish between different types of cotunnelling processes: the single-barrier cotunnelling processes shown in figure 22(a) and double-barrier cotunnelling processes illustrated in figure 22(b). Both single-barrier and double-barrier processes can be either spin-flip or non-spin-flip ones. The current flows due to double-barrier cotunnelling, whereas the single-barrier cotunnelling can influence the current in an indirect way, by changing the spin state of the dot. In the antiparallel configuration, there is a finite spin accumulation on the dot, as presented in figure 22(c). The different occupation probabilities for spin-up and spin-down electrons appear due to spin asymmetry in tunnelling processes. In equilibrium, both rates are equal and there is no spin accumulation, $P_\uparrow = P_\downarrow$. When a bias voltage is applied, and the system is in the antiparallel configuration, the relative amount of single-

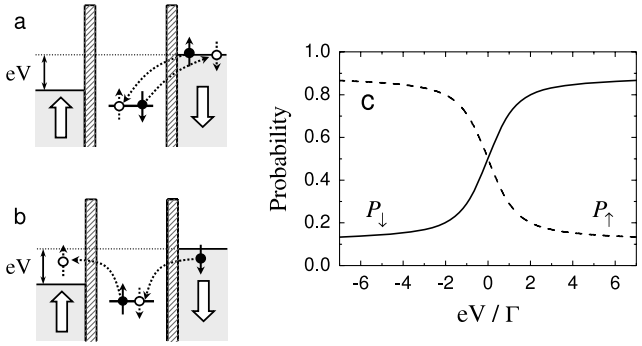

Figure 22. Single-barrier (a) and double-barrier (b) cotunnelling processes, and the occupation probabilities for spin-up and spin-down electrons in the antiparallel configuration (c). The parameters are $k_BT = 0.5\Gamma$, $\varepsilon = -U/2$, $U = 30\Gamma$, and $p = 0.5$. Reprinted figure with permission from [155]. Copyright 2005 by the American Physical Society.

barrier cotunnelling is diminished as compared to the double-barrier cotunnelling. This is because the rate of single-barrier cotunnelling is proportional to thermal energy, whereas that of double-barrier cotunnelling is proportional to the bias voltage. In the nonlinear response regime, the magnetic state of the dot is mainly determined by the spin-flip processes that transfer an electron from the left to the right leads. The one shown in figure 22(b) changes the dot spin from $|\uparrow\rangle$ to $|\downarrow\rangle$. Because the rate of this process is proportional to a product of densities of states for majority electrons, the corresponding rate is larger than that of the other process that changes the dot spin from $|\downarrow\rangle$ to $|\uparrow\rangle$, where only the minority spins are involved. This results in a nonequilibrium spin accumulation, $P_\downarrow > P_\uparrow$, that increases with increasing voltage, as shown in figure 22(c). The initial state for the dominant spin-flip cotunnelling process that contributes to current is $|\uparrow\rangle$, as sketched in figure 22(b). Thus, the conductance is diminished by spin accumulation. This is the mechanism by which spin accumulation gives rise to the nonzero tunnel magnetoresistance effect, $G^{\rm P} > G^{\rm AP}$, see figure 21(b).

Since the spin accumulation reduces electronic transport, any spin-flip process that reduces the spin accumulation should enhance the conductance. In particular, single-barrier spin-flip cotunnelling is an example of such a process. As pointed above, the rate of single-barrier processes scales with k_BT while that of double-barrier cotunnelling is proportional to $\max\{|eV|, k_BT\}$, which explains the mechanism of the zero-bias anomaly. At low bias voltage, $|eV| \lesssim k_BT$, single-barrier spin-flip processes play a significant role—they decrease the spin accumulation opening, in this way, the system for the fastest double-barrier cotunnelling. As a consequence, the current increases relatively fast with applied bias, leading to a maximum in differential conductance. For $|eV| \gg k_BT$, on the other hand, the relative role of single-barrier processes is negligible as compared to double-barrier cotunnelling, and the conductance is reduced. Thus, the interplay between the rates of double-barrier and single-barrier cotunnelling processes leads to a maximum in the differential conductance at the zero bias.

4.2.2. Effects of spin relaxation in the dot on cotunnelling transport. Intrinsic spin relaxation in the dot can result, for instance, from spin–orbit interaction, coupling of the electron spin to nuclear spins, etc. However, we will not consider a particular microscopic mechanism of the intrinsic spin-flip processes, but simply assume that the spin-flip relaxation is described by a spin-relaxation time $\tau_{\rm sf}$, and is taken into account *via* a relaxation term in the appropriate master equation for the occupation probabilities [157],

$$0 = \sum_{\nu,\nu'={\rm L,R}} \left(-\gamma_{\nu\nu'}^{\sigma\to\bar\sigma} P_\sigma + \gamma_{\nu\nu'}^{\bar\sigma\to\sigma} P_{\bar\sigma}\right) - \frac{2}{\tau_{\rm sf}} \frac{P_\sigma e^{\beta\varepsilon_\sigma} - P_{\bar\sigma} e^{\beta\varepsilon_{\bar\sigma}}}{e^{\beta\varepsilon_\sigma} + e^{\beta\varepsilon_{\bar\sigma}}}, \tag{44}$$

where $\beta = 1/(k_BT)$, P_σ denotes the probability that the dot is occupied by a spin-σ electron, and $\gamma_{\nu\nu'}^{\sigma\to\bar\sigma}$ is the cotunnelling rate from lead ν to lead ν' with a change of the dot spin from σ to $\bar\sigma$ ($\bar\sigma = -\sigma$). The last term describes the spin-relaxation processes, which in the case of spin-degenerate dot level reduces to $-(P_\sigma - P_{\bar\sigma})/\tau_{\rm sf}$.

As before, (see section 2) one can distinguish between the fast and slow spin-relaxation limits. The former (latter) limit corresponds to the situation when the time between successive cotunnelling events, $\tau_{\rm cot}$, is significantly longer (shorter) than the intrinsic spin-relaxation time $\tau_{\rm sf}$. A typical spin-relaxation time for quantum dots can be relatively long, up to μs [177, 178]. On the other hand, the time between successive cotunnelling events can be estimated taking into account the fact that the rate of spin-flip cotunnelling is generally larger than that of non-spin-flip cotunnelling (for a finite parameter U). Assuming $\varepsilon_\uparrow = \varepsilon_\downarrow = \varepsilon$, one then finds

$$\tau_{\rm cot} \approx \frac{h\varepsilon^2(\varepsilon+U)^2}{AU^2\Gamma^2}, \tag{45}$$

with $A = \max\{|eV|, k_BT\}$ and $h = 2\pi\hbar$. Assuming typical parameters [165], one can roughly estimate $\tau_{\rm cot}$ to range from 10^{-3} to 1 ns.

The anomalous behaviour of differential conductance in the antiparallel configuration results from spin asymmetry of the tunnelling processes, which gives rise to spin accumulation, $P_\uparrow \neq P_\downarrow$. The intrinsic spin-flip processes in the dot reduce the spin accumulation and this way suppress the anomaly. This behaviour is displayed in figure 23(a), where different curves correspond to different values of the parameter r defined as $r = h/(\tau_{\rm sf}\Gamma)$. Thus, $r = 0$ describes the case with no intrinsic spin relaxation, whereas the curves corresponding to nonzero r describe the influence of intrinsic relaxation processes. First of all, one can note that a small amount of intrinsic spin-flip processes enhance the zero-bias anomaly (see the curve for $r = 10^{-2}$ in figure 23(a)). This is because such processes then play a role similar to that of single-barrier spin-flip cotunnelling. In the case of fast spin relaxation, on the other hand, the spin accumulation is suppressed and the anomaly disappears, as can be seen in figure 23(a) for $r = 1$. It is also worth noting that spin-flip processes in the dot enhance the overall conductance in the antiparallel configuration. In the parallel configuration, however, the differential conductance does not depend on intrinsic relaxation.

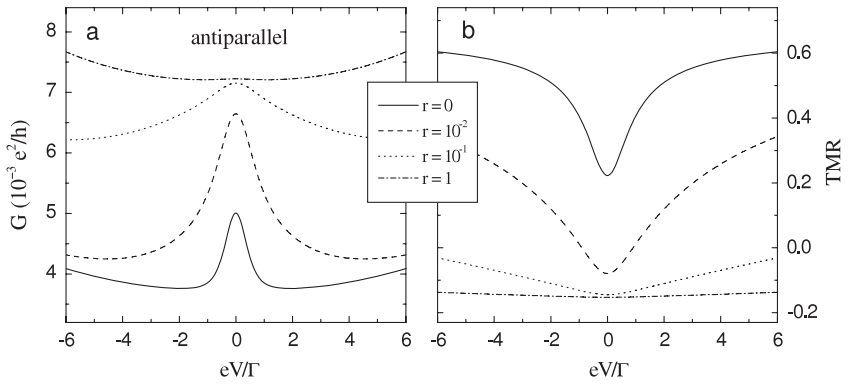

Figure 23. The differential conductance in the antiparallel configurations (a) and tunnel magnetoresistance (b) as a function of the bias voltage for different spin relaxation $r = h/(\tau_{\rm sf}\Gamma)$. The parameters are: $k_{\rm B}T = 0.2\Gamma$, $\varepsilon = -15\Gamma$, $U = 30\Gamma$, and $p_{\rm L} = p_{\rm R} = 0.5$. Reprinted figure with permission from [157]. Copyright 2006 by the American Physical Society.

Modifying the conductance in the antiparallel configuration, spin-relaxation processes suppress the tunnel magnetoresistance, as shown in figure 23(b). Since the zero-bias maximum in conductance is suppressed in the fast spin-relaxation limit, the corresponding dip in TMR at small voltages is also suppressed by the intrinsic relaxation processes. More specifically, the dip in TMR broadens with increasing r and disappears in the limit of fast relaxation (see the curve for $r = 1$). An interesting feature of TMR in the presence of spin-flip scattering in the dot is the crossover from positive to negative values when r increases, as illustrated in figure 23(b). Thus, the difference between conductances in the parallel and antiparallel magnetic configurations persists even for fast spin relaxation in the dot, contrary to the sequential tunnelling regime, where such a difference disappears [147]. This seemingly counterintuitive behaviour can be understood by taking into account the following two facts: (i) absence of spin accumulation in the dot for fast spin relaxation ($P_\uparrow = P_\downarrow$), and (ii) difference in the fastest cotunnelling processes contributing to the current in the two magnetic configurations. The fastest double-barrier cotunnelling processes involve only the majority-spin electrons of the two leads—thus, in the parallel configuration the fastest cotunnelling processes are the non-spin-flip ones. They take place either *via* the empty-dot virtual state (for one orientation of the dot spin) or *via* the doubly occupied dot virtual state (for the second orientation of the dot spin). The dominant contribution to the current is then proportional to $1/\varepsilon^2 + 1/(\varepsilon + U)^2$. On the other hand, in the antiparallel magnetic configuration the fastest cotunnelling processes are the spin-flip ones, which can occur only for one particular orientation of the dot spin. However, for this spin orientation cotunnelling can take place *via* both empty and doubly occupied dot virtual states. The corresponding dominant contribution to electric current is then proportional to $[1/\varepsilon - 1/(\varepsilon + U)]^2 = 1/\varepsilon^2 + 1/(\varepsilon + U)^2 - 2/[\varepsilon(\varepsilon + U)]$. It is thus clear that the difference in currents flowing through the system in the antiparallel and parallel configurations is equal to $-2/[\varepsilon(\varepsilon+U)]$, which results from the interference term. Since $\varepsilon < 0$ and $\varepsilon + U > 0$, this interference contribution is positive. As a result, the current in the antiparallel configuration is larger than the current in the parallel configuration.

The minimum in TMR at zero bias in the case of a symmetric Anderson model can be expressed as

$$\mathrm{TMR}_{\rm min} = \frac{2p^2\left(4k_{\rm B}T\Gamma^2 - \varepsilon^2 h/\tau_{\rm sf}\right)}{12(1-p^2)k_{\rm B}T\Gamma^2 + (3+p^2)\varepsilon^2 h/\tau_{\rm sf}}, \qquad (46)$$

whereas for $|eV| \gg k_{\rm B}T$ and $r \ll 1$ one finds

$$\mathrm{TMR}_{\rm max} = \frac{2p^2\left[2(3-p^2)k_{\rm B}T\Gamma^2 - \varepsilon^2 h/\tau_{\rm sf}\right]}{2(1-p^2)(3-p^2)k_{\rm B}T\Gamma^2 + (3+p^2)\varepsilon^2 h/\tau_{\rm sf}}. \qquad (47)$$

The latter formula approximates the value of TMR corresponding to the bias voltage at which the differential conductance has a local minimum. In the slow spin-relaxation limit one finds $\mathrm{TMR}_{\rm min} = 2p^2/(3-3p^2)$, and $\mathrm{TMR}_{\rm max} = 2p^2/(1-p^2)$. However, in the limit of fast spin-relaxation TMR becomes negative and is given by

$$\mathrm{TMR}_{\rm min} = \mathrm{TMR}_{\rm max} = -2p^2/(3+p^2). \qquad (48)$$

4.2.3. Effects of external magnetic field on cotunnelling transport. The discussion up to now was limited to the case of degenerate dot level. The situation changes when $\varepsilon_\uparrow \neq \varepsilon_\downarrow$, e.g., due to an external magnetic field. The level splitting is described by the parameter $\Delta = \varepsilon_\downarrow - \varepsilon_\uparrow$, where the magnetic field is assumed to be along the magnetic moment of the left electrode. In figure 24 we show the bias voltage dependence of the differential conductance in the parallel and antiparallel configurations for different values of parameter r. In the limit of no intrinsic spin relaxation in the dot (solid line in figure 24) and at low bias voltage, the dot is occupied by a spin-up electron and the current flows mainly due to non-spin-flip cotunnelling. The spin-flip cotunnelling processes are suppressed for $|\Delta| \gtrsim |eV|, k_{\rm B}T$, which results in steps in differential conductance at $|\Delta| \simeq |eV|$. The suppression of spin-flip inelastic cotunnelling was recently used as a tool to determine the spectroscopic g-factor [165]. When $|eV|$ becomes larger than $|\Delta|$, spin-flip cotunnelling is allowed, consequently the conductance increases. However, there is a large asymmetry of differential conductance in the antiparallel configuration with respect to the bias reversal. To understand this asymmetry, it is crucial to realize that when the splitting

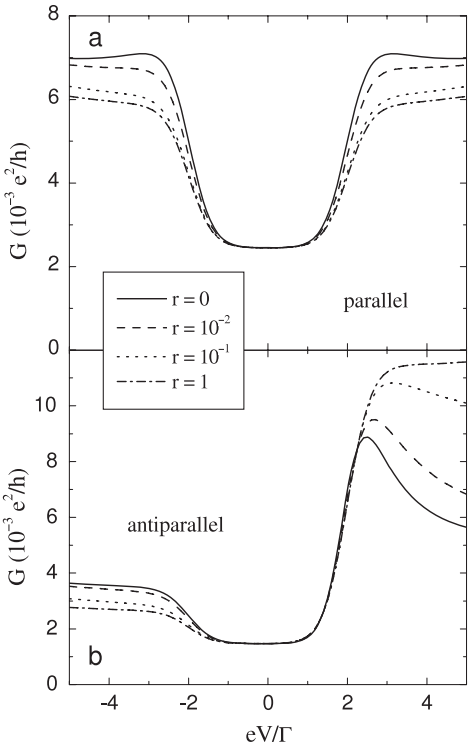

Figure 24. The differential conductance in the nonlinear response regime for different spin relaxation in the parallel (a) and antiparallel (b) configurations. The parameters are: $k_BT = 0.2\Gamma$, $\varepsilon_\uparrow = -16\Gamma$, $\varepsilon_\downarrow = -14\Gamma$, $U = 30\Gamma$ and $p = 0.5$. Reprinted figure with permission from [157]. Copyright 2006 by the American Physical Society.

$\Delta = \varepsilon_\downarrow - \varepsilon_\uparrow$ is larger than k_BT, the single-barrier spin-flip cotunnelling processes can occur only when the dot is occupied by a spin-down electron. Thus, the single-barrier processes can assist the fastest double-barrier cotunnelling processes, but only for positive bias. This is because the fastest processes can occur when the dot is occupied by a spin-down electron for negative bias and by a spin-up electron for positive bias, leading to a larger conductance for positive than for negative bias voltage. No such asymmetry occurs in the parallel configuration (see figure 24 (a)), as now the system is fully symmetric with respect to bias reversal.

The situation changes when intrinsic spin-flip relaxation processes occur in the dot. For the parameters assumed in figure 24, the spin relaxation in the dot affects the conductance only for $|eV| \gtrsim |\Delta|$, while for $|eV| \lesssim |\Delta|$ the conductance is basically independent of r (see figure 24). This is because for $|eV| \lesssim |\Delta|$ and $|\Delta| \gg k_BT$, the dot is predominantly occupied by a spin-up electron and the transitions to the spin-down state due to relaxation processes are energetically forbidden. As a consequence, the current flows mainly due to non-spin-flip cotunnelling, irrespective of spin-relaxation time. This scenario holds for both magnetic configurations of the system.

When $|eV| \gtrsim |\Delta|$, spin-flip cotunnelling processes can take place and the dot can be either in the spin-up or spin-down state. In the parallel configuration, figure 24(a), the conductance is slightly reduced by the spin-flip relaxation processes. This can be understood by realizing that the fastest non-spin-flip cotunnelling processes in the parallel

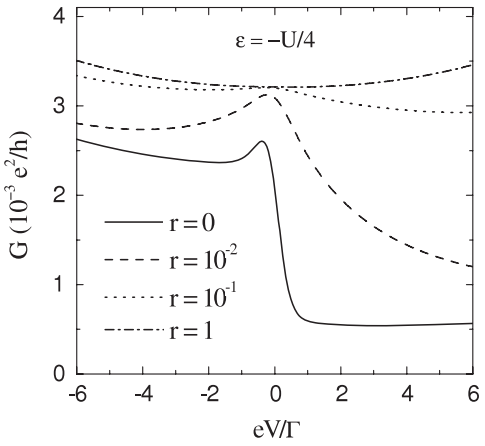

Figure 25. The differential conductance in the nonlinear response regime for the asymmetric Anderson model, $\varepsilon = -U/4$, for different spin relaxation. The parameters are: $k_BT = 0.2\Gamma$, $U = 60\Gamma$, $p_L = 0.95$ and $p_R = 0$. Reprinted figure with permission from [157]. Copyright 2006 by the American Physical Society.

configuration are more probable when the dot is occupied by a spin-down electron than by a spin-up one (due to smaller energy denominator, see equation (41)). Since the spin-down state (as that of larger energy) relaxes relatively fast to the spin-up state (which has definitely smaller energy), this leads to a reduction in the conductance. On the other hand, the differential conductance in the antiparallel configuration is enhanced by the relaxation processes for positive bias and diminished for negative bias voltages. Consider first the situation for positive bias. As already discussed above for $r = 0$, an important role in that transport regime is played by the single-barrier spin-flip cotunnelling processes, which open the system for the fast double-barrier cotunnelling by reversing spin of the dot from the spin-down to the spin-up state. The relaxation processes play a role similar to that of the single-barrier cotunnelling, and lead to a certain increase in the conductance. For negative bias voltage, in turn, the fast double-barrier cotunnelling processes occur when the dot is occupied by a spin-down electron. The probability of such events is decreased by spin relaxation, leading to a reduced conductance. An interesting consequence of the enhancement (reduction) of the differential conductance for positive (negative) bias voltage is an increase of the asymmetry with respect to the bias reversal—see the curve for $r = 1$ in figure 24(b).

4.2.4. Asymmetric situations. An interesting situation occurs when the quantum dot is coupled asymmetrically to the left and right leads ($p_L \neq p_R$). The differential conductance for a system with one electrode nonmagnetic and the other one made of a ferromagnet with large spin polarization (in the following referred to as strong ferromagnet) is shown in figure 25 for the case when the dot is described by an asymmetric Anderson model ($|\varepsilon| \neq \varepsilon + U$).

Consider first the situation in the absence of intrinsic spin relaxation in the dot (solid curves in figure 25). When $|eV| \gg k_BT$, the influence of single-barrier cotunnelling can be neglected [155]. The cotunnelling processes which transfer charge from one lead to another take place *via* two possible

virtual states—empty dot (an electron residing in the dot tunnels to one of the leads and another electron from the second lead enters the dot) and doubly occupied dot (an electron of spin opposite to that in the dot enters the dot and then one of the two electrons leaves the dot). Consider first positive bias ($eV > 0$, electrons flow from right to left, i.e., from normal metal to strong ferromagnet), and assume for clarity of discussion that the strong ferromagnet is a half-metallic one with full spin polarization (only spin-up electrons can then tunnel to the left lead). When a spin-down electron enters the dot, it has no possibility of leaving the dot for a long time. The allowed cotunnelling processes then occur *via* doubly occupied dot virtual states. In the absence of intrinsic spin relaxation in the dot, the only processes which can reverse the dot spin are the single-barrier cotunnelling ones, which however play a minor role when $k_BT \ll |eV|$. Thus, the current flows due to non-spin-flip cotunnelling *via* doubly occupied dot virtual states, whereas cotunnelling through empty-dot virtual states is suppressed. The situation is changed for negative bias (electrons flow from strong ferromagnet to normal metal). Now, the dot is mostly occupied by a spin-up electron, which suppresses cotunnelling *via* doubly occupied dot virtual state and the only contribution comes from cotunnelling *via* an empty-dot virtual state. The ratio of cotunnelling rates through the empty-dot and doubly occupied dot virtual states is approximately equal to $\xi = [\varepsilon/(\varepsilon + U)]^{-2}$. In the situation presented in figure 25 one finds $\xi \gg 1$. Accordingly, the conductance for negative bias is much larger than for positive bias voltage.

When $|eV|$ becomes of the order of k_BT or smaller, the rate of single-barrier cotunnelling is of the order of the rate of double-barrier cotunnelling. Therefore, the single-barrier processes can play an important role in transport. More precisely, single-barrier cotunnelling processes can reverse the spin of an electron in the dot and thus can open the system for the fast cotunnelling processes.

Intrinsic spin-flip processes in the dot have similar influence on electronic transport as in the case discussed in the previous section. As before, relaxation processes remove the asymmetry with respect to the bias reversal and suppress the zero-bias anomaly. Thus, the diode-like behaviour can appear only in the limit of slow spin relaxation, and is suppressed in the limit of fast spin relaxation, as shown in figure 25 by the curves corresponding to $r = 1$.

4.3. Systems with noncollinear magnetizations

New features of transport characteristics occur when the leads' magnetizations form an arbitrary noncollinear magnetic configuration [137, 140, 141, 148–150, 161, 179–184]. Such a configuration can be controlled by a weak external magnetic field, weak enough to neglect the corresponding Zeeman splitting of the dot level and weaker than the effective exchange field exerted on the dot by ferromagnetic leads. In particular, the differential conductance is significantly modified by the exchange field in noncollinear configurations. This also applies to the TMR effect, which for arbitrarily aligned leads' magnetizations can be defined as, TMR $= [I_P - I(\varphi)]/I(\varphi)$, where φ is an angle between the leads' magnetic moments.

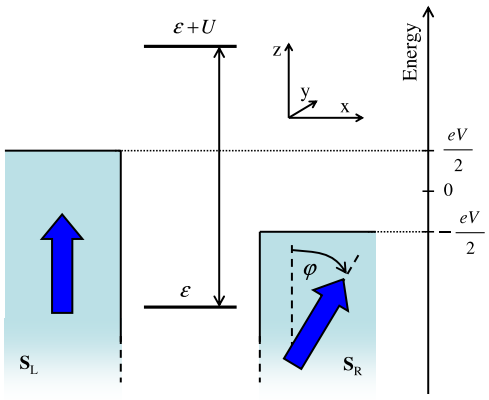

Figure 26. Schematic of a quantum dot coupled to ferromagnetic leads with noncollinearly aligned magnetizations. The net spin moments of the left $\mathbf{S}_L$ and right $\mathbf{S}_R$ lead form an angle φ. There is a symmetric bias voltage applied to the system.

The system, whose spin moments $\mathbf{S}_L$ and $\mathbf{S}_R$ of the left and right lead, respectively, form an arbitrary configuration is shown in figure 26. The corresponding Hamiltonian, written for the quantization axis of the dot equivalent to that of the left lead, is given by equation (26), where the tunnel Hamiltonian can be decomposed into two terms $H_T = H_{TL} + H_{TR}$. The term H_{TL} describes tunnelling processes between the left electrode and the dot, and takes the same form as for collinear configurations, while H_{TR} describes tunnelling processes between the dot and right lead, and acquires the form

$$H_{TR} = \sum_k \Big[\Big(t_{R+} c^\dagger_{Rk+} \cos\frac{\varphi}{2} - t_{R-} c^\dagger_{Rk-} \sin\frac{\varphi}{2} \Big) d_\uparrow + \Big(t_{R+} c^\dagger_{Rk+} \sin\frac{\varphi}{2} + t_{R-} a^\dagger_{Rk-} \cos\frac{\varphi}{2} \Big) d_\downarrow + \text{h.c.} \Big]. \quad (49)$$

The real-time diagrammatic method described at the beginning of this section for collinear magnetic configurations can be extended to include the effects due to noncollinearity of the leads' magnetic moments. The density matrix of the quantum dot for an arbitrary magnetic configuration is given by

$$\hat{\rho}_D = \begin{pmatrix} P_0^0 & 0 & 0 & 0 \\ 0 & P_\uparrow^\uparrow & P_\downarrow^\uparrow & 0 \\ 0 & P_\uparrow^\downarrow & P_\downarrow^\downarrow & 0 \\ 0 & 0 & 0 & P_d^d \end{pmatrix}. \quad (50)$$

The diagonal elements of the density matrix correspond to the respective occupation probabilities, while the off-diagonal elements $P_\uparrow^\downarrow$ and $P_\downarrow^\uparrow$ describe the dot spin $\vec{S}$, with $S_x = \mathrm{Re}P_\downarrow^\uparrow$, $S_y = \mathrm{Im}P_\downarrow^\uparrow$, and $S_z = (P_\uparrow^\uparrow - P_\downarrow^\downarrow)/2$. The density matrix elements can be determined from the corresponding kinetic equation, which in the steady state and for a spin-degenerate dot level can be written as [104, 161, 166, 167]

$$0 = \sum_{\chi_1',\chi_2'} P^{\chi_1'}_{\chi_2'} \Sigma^{\chi_1'\chi_1}_{\chi_2'\chi_2}. \quad (51)$$

By expanding the self-energies and density matrix elements, one can calculate the sequential and cotunnelling current.

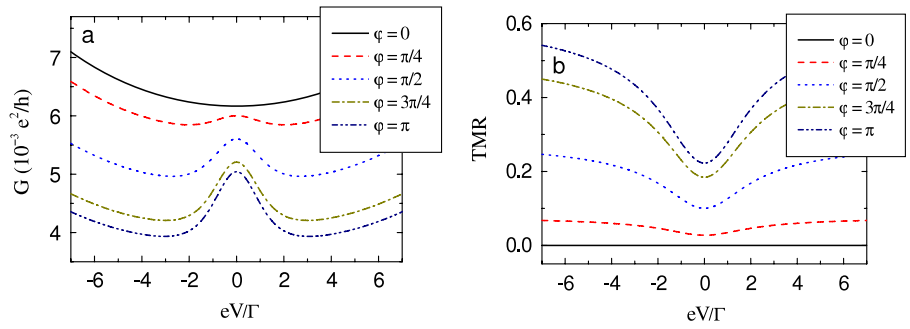

Figure 27. Differential conductance $G = \mathrm{d}I/\mathrm{d}V$ (a) and tunnel magnetoresistance TMR (b) as a function of the bias voltage V for indicated values of the angle φ between magnetic moments, calculated for symmetric Anderson model. The parameters are: $k_\mathrm{B}T = 0.5\Gamma$, $\varepsilon = -15\Gamma$, $U = 30\Gamma$, and $p_\mathrm{L} = p_\mathrm{R} \equiv p = 0.5$. Reprinted with permission from [161]. Copyright 2007 by the American Physical Society.

In the following we focus on transport in the Coulomb blockade regime, $|\varepsilon|, |\varepsilon + U| \gg \Gamma, k_\mathrm{B}T$, and when the dot is singly occupied, $\varepsilon < 0 < \varepsilon + U$. From the discussion above we know that there is an anomalous behaviour of the differential conductance in the small bias regime for antiparallel magnetic configuration. Now, we will consider how this anomaly changes when magnetic configuration varies continuously from antiparallel to parallel alignment.

4.3.1. Symmetric Anderson model. We consider first the symmetric Anderson model, $\varepsilon = -U/2$. The exchange field then vanishes for an arbitrary magnetic configuration, and both differential conductance and TMR change monotonically when going from antiparallel to parallel magnetic configurations. However, for $\varepsilon \neq -U/2$, the effects of exchange field become important and lead to a nontrivial behaviour of the transport characteristics, as will be discussed later.

The differential conductance G as a function of the bias voltage is shown in figure 27(a) for several values of the angle φ. The conductance varies monotonically with the angle between leads' magnetic moments. When the angle increases from zero to π, an anomaly emerges at small values of φ and its relative height increases with increasing angle, reaching a maximum value at $\varphi = \pi$.

The exchange field for a symmetric Anderson model is negligible, and the average dot spin tends to zero in the linear response regime. The angular dependence of the linear conductance can be then expressed as

$$G = \frac{e^2\Gamma^2}{2h\varepsilon^2}\left[3 - p^2\left(1 + 2\sin^2\frac{\varphi}{2}\right)\right]. \tag{52}$$

The variation of G with φ at low bias is thus characterized by the factor $1 + 2\sin^2(\varphi/2)$, which leads to maximum (minimum) conductance in the parallel (antiparallel) magnetic configuration. Such behaviour is typical of a normal spin-valve effect.

The bias dependence of the associated TMR is shown in figure 27(b) for several values of the angle φ. The zero-bias anomaly in the differential conductance (see figure 27(a)) leads to a corresponding anomaly (dip) in TMR at small bias voltages. The dip in TMR decreases when the magnetic configuration departs from the antiparallel alignment, and eventually disappears in the parallel configuration. The variation of TMR with the angle is monotonic, similarly to the angular variation of the differential conductance. The dependence of TMR on the angle φ at zero bias is approximately given by the formula

$$\mathrm{TMR} = \frac{2p^2\sin^2\frac{\varphi}{2}}{3 - p^2\left(1 + 2\sin^2\frac{\varphi}{2}\right)}. \tag{53}$$

Now, the angular dependence of TMR is governed by $\sin^2(\varphi/2)$, which gives maximum TMR in the antiparallel configuration and zero TMR in the parallel one.

4.3.2. Asymmetric Anderson model. The transport characteristics, described above for the symmetric Anderson model, are significantly modified when the model becomes asymmetric, i.e. when $\varepsilon \neq -U/2$. This can be realized by shifting the dot level position by a gate voltage applied to the dot. Different contributions to the exchange field do not cancel then, and the resulting effective exchange field becomes nonzero. This exchange field has a significant influence on transport properties. The strength of effective exchange field grows with the deviation of the Anderson model from the symmetric one, described quantitatively by $2\varepsilon + U$ (with $2\varepsilon + U = 0$ for the symmetric model).

The leading contribution to the exchange field comes from the first-order diagrams of the perturbation expansion in terms of the real-time diagrammatic technique, whereas the current flows due to the second-order tunnelling processes. This leads to two different timescales which determine transport characteristics. Transport properties are thus a result of the interplay of the first- and second-order processes. Although the first-order processes do not contribute directly to current, they influence transport *via* modification of the dot spin.

The differential conductance is shown in figure 28(a) as a function of bias voltage for an asymmetric Anderson model, $\varepsilon \neq -U/2$, and for different values of φ. The low bias differential conductance becomes enhanced in a certain range of the angle φ, leading to a nonmonotonic dependence of the conductance G on the angle between the leads' magnetizations. This nonmonotonic behaviour is also visible in TMR, see figure 28(b). There is also a range of the angle φ, where TMR changes sign and becomes negative in the small bias region,

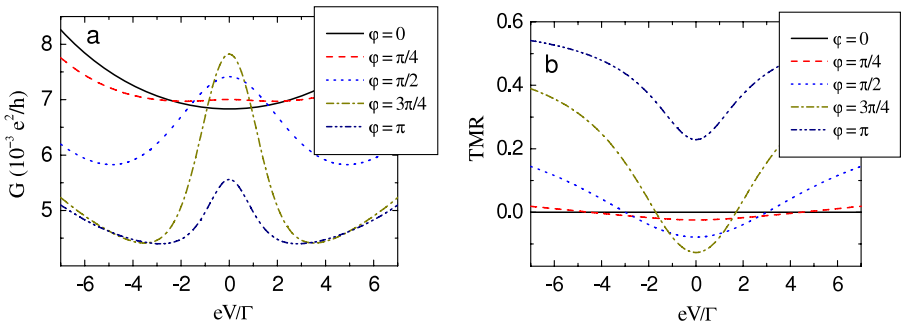

Figure 28. The differential conductance $G = \mathrm{d}I/\mathrm{d}V$ (a) and tunnel magnetoresistance TMR (b) as a function of the bias voltage V for indicated values of the angle φ for the asymmetric Anderson model $\varepsilon = -12\Gamma$ and $U = 30\Gamma$. The other parameters are the same as in figure 27. Reprinted with permission from [161]. Copyright 2007 by the American Physical Society.

i.e. the corresponding conductance is larger than that in the parallel configuration.

The most characteristic features of transport characteristics in the presence of exchange field are the enhanced differential conductance at a noncollinear alignment and its rapid drop when the system approaches the antiparallel configuration. The key role in this behaviour is played by the first-order processes giving rise to the exchange field. These processes lead to the precession of spin in the dot, which facilitates tunnelling processes and leads to an increase in the conductance as compared to that in the parallel configuration. When the configuration becomes close to the antiparallel one, the first-order processes become suppressed and the conductance drops to that for antiparallel alignment. The nonmonotonic behaviour of the differential conductance with φ leads to a nonmonotonic dependence of TMR. The effects due to exchange field give rise to a local minimum in TMR in a noncollinear magnetic configuration. Moreover, in this transport regime TMR changes sign and becomes negative. When the magnetic configuration is close to the antiparallel one, TMR starts to increase rapidly, reaching a maximum for $\varphi = \pi$. The negative TMR and its sudden increase when the configuration tends to the antiparallel one are a consequence of the processes leading to nonmonotonic behaviour of the differential conductance, as described above.

To understand more intuitively the above presented behaviour of the differential conductance and TMR at low bias voltage and close to the antiparallel configuration, one should consider two different timescales. One timescale, τ_{prec}, is established by the virtual first-order processes responsible for the spin precession due to exchange field,

$$\left|\tau_{\mathrm{prec}}^{-1}\right| \approx \frac{\Gamma}{2h} p \sin\varphi \ln\left|\frac{\varepsilon}{\varepsilon + U}\right|. \tag{54}$$

The second timescale, τ_{cot}, is associated with second-order processes which drive the current through the system. At low temperature and low bias voltage, the cotunnelling rate can be expressed as

$$\tau_{\mathrm{cot}}^{-1} \approx \frac{\Gamma^2}{4h}(1+p)(1-p\cos\varphi)\frac{|eV|U^2}{\varepsilon^2(\varepsilon+U)^2}. \tag{55}$$

The rate τ_{cot} depends linearly on the applied voltage, whereas τ_{prec} is relatively independent of V. As a consequence, at low bias and for noncollinear configuration, the exchange field plays an important role leading to a nonmonotonic dependence of differential conductance on the angle between the leads' magnetizations. When magnetic configuration is close to the antiparallel one, the spin precession rate is decreased ($|\tau_{\mathrm{prec}}^{-1}| \sim \sin\varphi$) and, at certain angle, the rate of spin precession becomes comparable to the cotunnelling rate. This gives rise to a sudden drop (increase) in differential conductance (TMR). We note that the nonmonotonic dependence of differential conductance and magnetoresistance has also been observed in quantum dots in the strong coupling limit [140, 141].

5. Transport through multi-level quantum dots connected to ferromagnetic leads

Up to now we have discussed theoretical aspects of electronic transport through the simplest quantum dots, i.e. the dots with only one orbital level. Real dots are usually more complex and their electronic spectrum includes many orbital levels taking part in electronic transport. This may significantly change transport characteristics and also may lead to qualitatively new features [185–190]. In this section we will consider some of the new effects in transport through multi-dot systems.

5.1. Sequential transport in two-level dots

The schematic of a two-level quantum dot coupled to ferromagnetic leads with collinear magnetizations is shown in figure 29. The quantum dot is described by the following Hamiltonian

$$\hat{H}_{\mathrm{D}} = \sum_{j\sigma}\varepsilon_j n_{j\sigma} + U\sum_j n_{j\uparrow}n_{j\downarrow} + U'\sum_{\sigma\sigma'} n_{1\sigma}n_{2\sigma'} - \frac{\Delta}{2}\sum_j\left(n_{j\uparrow} - n_{j\downarrow}\right), \tag{56}$$

where $n_{j\sigma}$ is the particle number operator, $n_{j\sigma} = d_{j\sigma}^{\dagger}d_{j\sigma}$, $d_{j\sigma}^{\dagger}$ ($d_{j\sigma}$) is the creation (annihilation) operator of an electron with spin σ on the jth level ($j = 1, 2$), and ε_j is the corresponding single-particle energy. The on-level Coulomb repulsion between two electrons of opposite spins is described by U, whereas the inter-level repulsion energy is denoted by U'. The fourth term in equation (56) describes the Zeeman

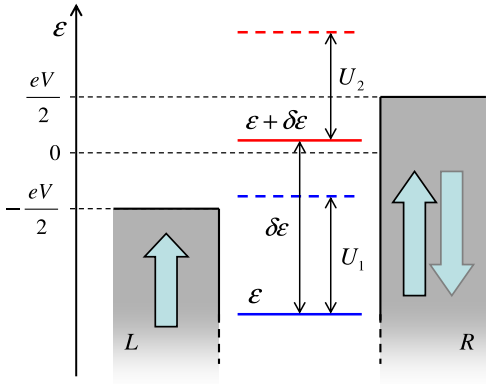

Figure 29. Energy diagram of a two-level quantum dot coupled to ferromagnetic leads. For clarity the energy diagram is shown here for $\Delta = U' = 0$. The leads' magnetizations can form either parallel or antiparallel configurations. The arrows indicate the net spin of the leads.

energy, with $\Delta = g\mu_B B$ being the Zeeman splitting of the energy levels (B is an external magnetic field along the magnetic moment of the left electrode). To present the main features of transport characteristics, it is convenient to introduce the level spacing $\delta\varepsilon = \varepsilon_2 - \varepsilon_1$ and also define $\varepsilon_1 \equiv \varepsilon$.

In the following we analyse the current I, differential conductance G, and the Fano factor F in the parallel and antiparallel magnetic configurations, as well as the corresponding TMR for two-level quantum dots. The Fano factor, $F = S/S_p$, describes the deviation of the zero-frequency shot noise S from the Poissonian shot noise $S_p = 2e|I|$. The results presented have been obtained with the real-time diagrammatic technique [169, 185, 188].

5.1.1. Quantum dots symmetrically coupled to ferromagnetic leads. Typical variation of the differential conductance with the bias voltage V and level position ε (gate voltage) is shown in figure 30(a) for the parallel magnetic configuration. The conductance in the antiparallel configuration is qualitatively similar to that in the parallel configuration, but generally smaller, which leads to a nonzero TMR effect. The diamonds in figure 30(a) around $V = 0$ correspond to the Coulomb blockade regions. When lowering the position of the dot levels, the charge of the dot changes successively. The dot is empty for $\varepsilon \gtrsim 0$, occupied by one electron for $0 \gtrsim \varepsilon \gtrsim -U$, doubly occupied for $-U \gtrsim \varepsilon \gtrsim -(2U + \delta\varepsilon)$, occupied by three electrons for $-(2U + \delta\varepsilon) \gtrsim \varepsilon \gtrsim -(3U + \delta\varepsilon)$, and the two orbital levels of the dot are fully occupied for $-(3U + \delta\varepsilon) \gtrsim \varepsilon$. In all these transport regions the dot is in a well-defined charge state, and the sequential tunnelling is exponentially suppressed. If the bias voltage is increased above a certain threshold voltage, the current flows due to first-order (sequential) tunnelling processes. When the thermal energy is low enough, one then observes a well-resolved step in the current as a function of the bias voltage. In the density plots shown in figure 30(a), this can be seen in the form of lines that clearly separate the Coulomb blockade regions from transport regions associated with consecutive charge states taking part in transport. When the bias voltage increases further, additional steps (and consequently lines in figure 30(a)) arise at voltages where new states become active in transport.

The corresponding TMR as a function of the bias and gate voltages is shown in figure 30(b). It is worth noting that TMR takes now several well-defined values. Such behaviour of TMR is significantly different from that for a single-level quantum dot, where TMR in the sequential tunnelling regime acquires only two values [156]. As in single-level dots, TMR in the linear response regime is independent of the gate voltage and is given by $p^2/(1 - p^2)$, i.e. half of the TMR in the Jullière model [13]. Figure 30 also shows that, when increasing the bias voltage V and keeping constant position of the dot levels, the current and TMR acquire some specific and well-defined values in different transport regions. As shown in [188], the current and TMR at these plateaus can be approximated by simple analytical formulae.

This behaviour is presented in more detail in figure 31(a), where the bias voltage dependence of the current and TMR is shown explicitly for the case when the dot level is above ($\varepsilon = U/2$) the Fermi level of the leads at equilibrium. The current in both magnetic configurations and the associated TMR exhibit characteristic plateaus which correspond to different transport regions. The corresponding Fano factors F_P and F_{AP} in the parallel and antiparallel magnetic configurations are shown in figure 31(b). Similarly as for current and TMR, the Fano factor acquires roughly constant values, different in different transport regions. Due to the spin asymmetry in the coupling of the dot to external leads, the bias

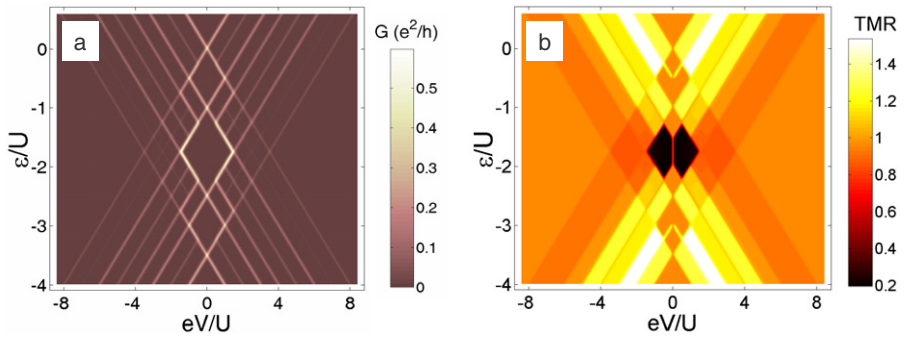

Figure 30. The differential conductance $G = dI/dV$ as a function of the bias voltage and level position in the parallel magnetic configuration (a) and TMR (b) for the parameters: $k_B T = \Gamma$, $\delta\varepsilon = 25\Gamma$, $U = 50\Gamma$, $\Delta = 0$, $p_L = p_R \equiv p = 0.7$, and $\Gamma_{rj} \equiv \Gamma/2$ ($r = L, R$, $j = 1, 2$). Reprinted figure with permission from [188]. Copyright 2007 by IOP Publishing Limited.

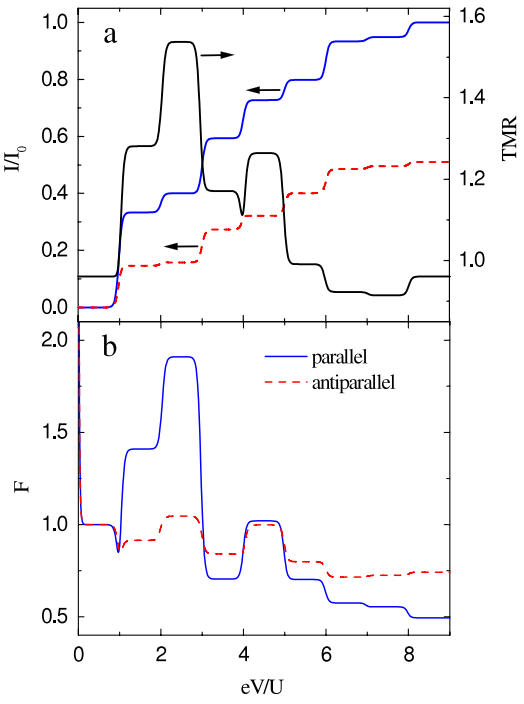

Figure 31. Current (a) in the units of $I_0 = e\Gamma/\hbar$ and Fano factor (b) in the parallel (solid line) and antiparallel (dashed line) configurations as well as tunnel magnetoresistance (a) as a function of the bias voltage for $\varepsilon = U/2$. The other parameters are the same as in figure 30. Reprinted figure with permission from [188]. Copyright 2007 by IOP Publishing Limited.

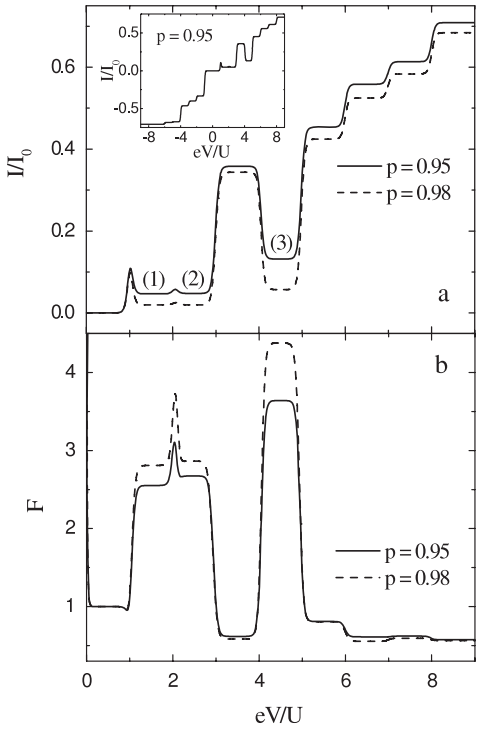

Figure 32. The current (a) in units of $I_0 = e\Gamma/\hbar$ and Fano factor (b) as a function of the bias voltage for $p_L \equiv p = 0.95, 0.98$, $p_R = 0$, while the other parameters are the same as in figure 30. The inset in part (a) shows the current in the whole range of the bias voltage. Reprinted figure with permission from [188]. Copyright 2007 by IOP Publishing Limited.

dependence of the Fano factor is significantly different from that in the corresponding nonmagnetic situations [185]. For both magnetic configurations of the system, the Fano factor depends on the polarization factor p (differently in the two configurations, in general). If $|eV| \ll k_B T$, the Fano factor becomes divergent due to the thermal noise, which dominates in this transport regime; in the case of $V = 0$, the noise is given by $S = 4k_B T G^{\rm lin}$, with $G^{\rm lin}$ being the linear conductance, leading to a divergence of the Fano factor [116, 191]. Apart from this, in some transport regions we find $F_P > F_{AP}$, while in other ones $F_P < F_{AP}$. The ratio F_P/F_{AP} generally depends on the spin polarization of the leads p [188]. Furthermore, we note that if the leads are half-metallic, the Fano factor in the parallel configuration diverges as $p \to 1$. This increase of the Fano factor is due to the enhanced spin asymmetry in transport processes through the dot [146, 192, 193]. On the other hand, in the antiparallel configuration the Fano factor tends to unity for $p \to 1$, except for the Coulomb blockade regime with two electrons trapped in the dot, where the shot noise is super-Poissonian.

5.1.2. Quantum dots asymmetrically coupled to the leads. When one of the leads is half-metallic ($p = 1$) and the other one is nonmagnetic ($p = 0$), transport characteristics become asymmetric with respect to the bias reversal. Furthermore, the current can be suppressed in certain bias regions, and this suppression is accompanied by the occurrence of NDC. This basically happens when the electrons residing in the dot have spins opposite to those of electrons in the half-metallic drain electrode. In figure 32 we show the current and Fano factor for a quantum dot coupled to half-metallic (left) and nonmagnetic (right) lead as a function of the bias voltage. For the situation shown in figure 32, current is suppressed in certain regions of positive bias voltage. As follows from figure 32(a), there are three such blockade regions, labelled with the consecutive numbers. On the other hand, for negative bias voltage, the current changes monotonically with the transport voltage, as shown in the inset of figure 32(a).

The mechanism of the blockade can be described as follows. In the blockade region (1), $1 \lesssim eV/U \lesssim 2$, the dot is in the state $|\downarrow\rangle|0\rangle$ and the spin-down electron residing in the dot has no possibility of tunnelling further to the left lead, which leads to suppression of the current. Here, the first (second) *ket* corresponds to the first (second) orbital level of the dot. The blockade region (2), $2 \lesssim eV/U \lesssim 3$, is associated with the occupation of the states $|\downarrow\rangle|0\rangle$ and $|0\rangle|\downarrow\rangle$. The current is then prohibited due to the full occupation of the single-particle spin-down states. When increasing the bias voltage further, $3 \lesssim eV/U \lesssim 4$, the blockade of the current becomes suppressed (see the plateau between regions (2) and (3) in figure 32(a)), which is due to a finite occupation of state $|\uparrow\downarrow\rangle|0\rangle$. Although tunnelling of spin-down electrons is then blocked, the current is still carried by spin-up electrons. In turn, the blockade region (3) occurs for $4 \lesssim eV/U \lesssim 5$, where the dot is in the triplet state $|\downarrow\rangle|\downarrow\rangle$ and tunnelling is also suppressed. Thus, the current is blocked when the total dot spin S_z is either $S_z = -1/2$ or $S_z = -1$, i.e., the spin of electrons on

the dot is opposite to that of electrons in the half-metallic lead. There is no suppression of current for negative voltage. This is because the electrons residing in the dot can always tunnel to the nonmagnetic drain electrode. It is also interesting to note that a pure triplet state is formed in the region (3) [188, 194].

The current blockade in the regions (1)–(3) in figure 32(a) for positive bias is not due to the charging effects as in the Coulomb blockade regime, but due to a particular occupation of the dot spin state. Such a blockade is frequently referred to as the Pauli spin blockade, and has already been found in single-dot and double-dot systems [195–199]. It is worth noting that the current blockade in figure 32(a) is not complete—there is a small leakage current in each blockade region, which results from the fact that the assumed spin polarization of the half-metallic lead is not exactly equal to unity. When spin polarization is increased, the current in the blockade regions decreases (compare the curves for $p = 0.95$ and 0.98).

The spin blockade of charge current leads to super-Poissonian shot noise, i.e., the corresponding Fano factor is larger than unity. On the other hand, the Fano factor outside the spin blockade regions is sub-Poissonian (smaller than unity), as shown in figure 32(b). The enhancement of the shot noise in the Pauli blockade regions is a consequence of large spin asymmetry in the tunnelling processes. The occurrence of a spin-down electron on the dot prevents further tunnelling processes for a longer time, while spin-up electrons on the dot can escape much faster, allowing further tunnelling processes. This bunching of fast tunnelling processes gives rise to large current fluctuations, and consequently also to Fano factors much larger than unity.

Recently an interacting three-terminal quantum dot with ferromagnetic leads was considered in [192, 193]. The dot operated as a beam splitter—one contact was a source and the other two acted as drains. The authors found a dynamical spin blockade (spin-dependent bunching of tunnelling events) and positive zero-frequency cross-correlations of the current in the drain electrodes.

5.2. Cotunnelling in two-level quantum dots

In all transport characteristics discussed above only sequential tunnelling processes were taken into account, while higher-order processes, in particular the cotunnelling ones, have been neglected. From our discussion on single-level dots we already know that higher-order contributions are particularly pronounced in the blockade regions, where they have a significant influence on TMR and Fano factor. The role of cotunnelling processes in two-level dots was studied in a recent paper [200]. It has been shown there that the cotunnelling processes lead to a significant enhancement (or reduction) of TMR in the blockade regime. Outside the blockade regions, however, TMR is determined mainly by sequential transport, so the contribution from cotunnelling processes is rather minor. Similarly, the cotunnelling processes significantly modify the Fano factor in the blockade regions, while outside these regions the Fano factor is only weakly sensitive to the cotunnelling. More specifically, the Fano factor in the blockade regions is reduced in comparison to that obtained in the sequential transport limit. However, it is still larger than one, indicating super-Poissonian shot noise in the blockade regime due to bunching of the fastest cotunnelling processes.

There is also another interesting phenomenon in the blockade regime, which resembles the zero-bias anomaly observed in single-level dots in the antiparallel magnetic configuration. This takes place when each orbital level of the dot at equilibrium is occupied by a single electron, and the system is in the Coulomb blockade regime [189]. The Hamiltonian H of the system is given by equation (26), where H_{D} additionally includes the exchange term and can be expressed by the formula [201, 202]

$$H_{\mathrm{D}} = \sum_{j\sigma} \varepsilon_j n_{j\sigma} + U \sum_{j} n_{j\uparrow} n_{j\downarrow} + U' \sum_{\sigma\sigma'} n_{1\sigma} n_{2\sigma'} - J \sum_{\alpha\beta\gamma\delta} d^{\dagger}_{1\alpha} d_{1\beta} d^{\dagger}_{2\gamma} d_{2\delta} \vec{\sigma}_{\alpha\beta} \vec{\sigma}_{\gamma\delta}. \tag{57}$$

The last term in H_{D} corresponds to the exchange energy according to the Hund's rule, with J being the respective exchange coupling and $\vec{\sigma}$ denoting a vector of Pauli spin matrices.

Six different two-particle states of the dot are possible, these are: three singlets $|S = 0, M = 0\rangle_1 = (|\uparrow\rangle|\downarrow\rangle - |\downarrow\rangle|\uparrow\rangle)/\sqrt{2}$, $|0, 0\rangle_2 = |\uparrow\downarrow\rangle|0\rangle$, $|0, 0\rangle_3 = |0\rangle|\uparrow\downarrow\rangle$, and three triplets $|1, 0\rangle = (|\uparrow\rangle|\downarrow\rangle + |\downarrow\rangle|\uparrow\rangle)/\sqrt{2}$, $|1, 1\rangle = |\uparrow\rangle|\uparrow\rangle$ and $|1, -1\rangle = |\downarrow\rangle|\downarrow\rangle$. In the case of finite level spacing, $\delta\varepsilon > k_{\mathrm{B}}T, \Gamma$, and $J < \delta\varepsilon$, the lowest singlet state is $|0, 0\rangle_2$. Transport characteristics strongly depend on the ground state of the system. It is therefore useful to introduce the difference between the energy of the lowest lying singlet (ε_{S}) and triplet (ε_{T}) states, $\Delta_{\mathrm{ST}} = \varepsilon_{\mathrm{S}} - \varepsilon_{\mathrm{T}} = J - \delta\varepsilon$.

For $\Delta_{\mathrm{ST}} < 0$, the ground state of the dot is a singlet, $|0, 0\rangle_2$, whereas for $\Delta_{\mathrm{ST}} > 0$, the ground state is a triplet, which is three-fold degenerate, $|1, 0\rangle$, $|1, 1\rangle$, $|1, -1\rangle$. On the other hand, for $\Delta_{\mathrm{ST}} = 0$, the dot is in a mixed state and the occupation of singlet and each triplet is equal at equilibrium and given by 1/4.

Figure 33 presents the bias voltage dependence of differential conductance G in the parallel and antiparallel magnetic configuration and for several values of $\Delta_{\mathrm{ST}} = J - \delta\varepsilon$. Let us consider the situation in figure 33(c), which corresponds to degenerate singlet and triplet states, $\Delta_{\mathrm{ST}} = 0$. The differential conductance in the parallel configuration exhibits a smooth parabolic dependence on the bias voltage, whereas in the antiparallel configuration there is a maximum at the zero-bias voltage. This effect bears a resemblance to that found in the case of singly occupied one-level quantum dots discussed in previous sections [155]. Here, however, the mechanism leading to the maximum is different—the zero-bias peak appears due to cotunnelling through the singlet and triplet states of the dot. In the case of $\Delta_{\mathrm{ST}} = 0$ and at low bias voltages, all the four dot states, i.e. $|0, 0\rangle_2$, $|1, 0\rangle$, $|1, -1\rangle$, $|1, 1\rangle$, participate in transport on an equal footing. Consequently, the current flows due to both spin-flip and non-spin-flip cotunnelling processes. To understand the mechanism leading to the zero-bias peak, one should bear in mind that in the antiparallel configuration the spin-majority

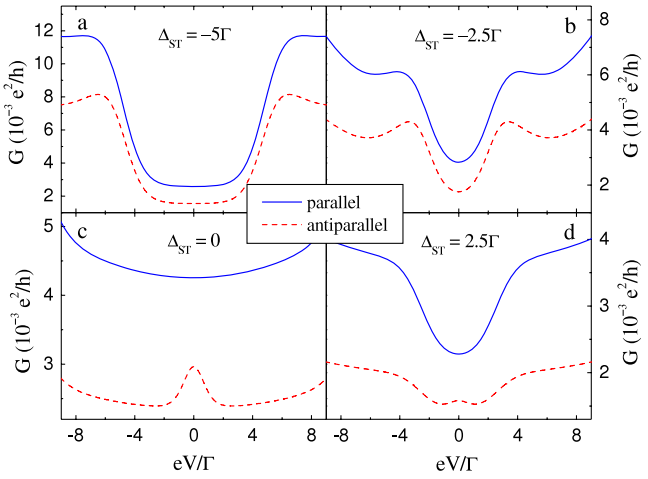

Figure 33. The differential conductance in the parallel (solid line) and antiparallel (dashed line) magnetic configuration of the system as a function of the bias voltage for several values of $\Delta_{ST} = J - \delta\varepsilon$ as indicated: (a) $\Delta_{ST} = -5\Gamma$, (b) $\Delta_{ST} = -2.5\Gamma$, (c) $\Delta_{ST} = 0$, (d) $\Delta_{ST} = 2.5\Gamma$. The other parameters are: $k_B T = 0.5\Gamma$, $\varepsilon = -60\Gamma$, $\delta\varepsilon = 5\Gamma$, $U = U' = 40\Gamma$, and $p = 0.5$. Reprinted figure with permission from [189]. Copyright 2006 by IOP Publishing Limited.

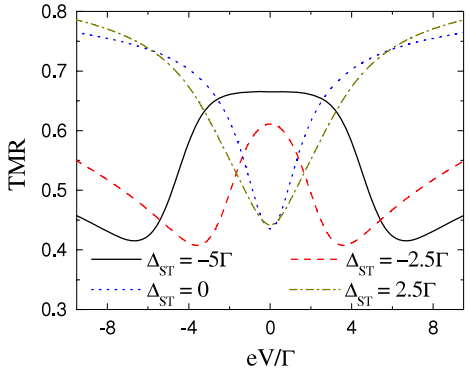

Figure 34. Tunnel magnetoresistance as a function of the bias voltage for $\Delta_{ST} = -5, -2.5, 0, 2.5\Gamma$, as indicated in the figure. The other parameters are the same as in figure 33. Reprinted figure with permission from [189]. Copyright 2006 by IOP Publishing Limited.

electrons of one lead tunnel to the spin-minority electron band of the other lead. For example, for positive bias voltage (electrons tunnel then from the right to left lead), the spin-↑ electrons can easily tunnel to the left lead (the spin-↑ electrons are the majority ones), while this is more difficult for the spin-↓ electrons (they tunnel to the minority electron band). Thus, the occupation of state $|1,-1\rangle$ ($|\downarrow\rangle|\downarrow\rangle$) is increased with increasing bias voltage, while the occupation of state $|1,1\rangle$ ($|\uparrow\rangle|\uparrow\rangle$) decreases. The unequal occupations of these triplet states lead to a nonequilibrium spin accumulation in the dot, $P_{|1,1\rangle} - P_{|1,-1\rangle} < 0$. It is further interesting to note that in the antiparallel configuration the possible non-spin-flip cotunnelling processes are proportional to $\Gamma_L^+\Gamma_R^-$ and $\Gamma_L^-\Gamma_R^+$, whereas the spin-flip cotunnelling is proportional to $\Gamma_L^+\Gamma_R^+$ and $\Gamma_L^-\Gamma_R^-$. It is clear that the fastest cotunnelling processes are the ones involving only the majority spins, i.e. $\Gamma_L^+\Gamma_R^+$. However, because of nonequilibrium spin accumulation, with increasing bias ($V > 0$), the dot becomes dominantly occupied by majority electrons of the right lead, $P_{|1,-1\rangle} > P_{|1,1\rangle}$, and the processes proportional to $\Gamma_L^+\Gamma_R^+$ are suppressed. As a consequence, the differential conductance drops with the bias voltage, leading to the zero-bias peak. This is thus the nonequilibrium accumulation of spin $S = 1$ which is responsible for the maximum in G at low bias voltage. Because the dot is coupled symmetrically to the leads, there is no spin accumulation in the parallel configuration and the differential conductance exhibits a smooth parabolic dependence.

The maximum in the conductance at zero bias disappears for $\Delta_{ST} < 0$ as well as for $\Delta_{ST} > 0$. Instead of the narrow maximum, a relatively broad minimum develops then in the conductance for both magnetic configurations, as shown in figures 33(a), (b) or for one magnetic configuration as in figure 33(d). Consider, for instance, the case $\Delta_{ST} < 0$, shown in figures 33(a), (b). At low bias voltage the dot is occupied by two electrons on the lowest energy level and the ground state is singlet, $S = 0$. Current is mediated then only by non-spin-flip cotunnelling processes. Once $|eV| \gtrsim |\Delta_{ST}|$, the triplet states start participating in transport leading to an increase in the differential conductance at $|eV| \approx |\Delta_{ST}|$. Thus, the suppression of cotunnelling through $S = 1$ states gives rise to a broad minimum in the differential conductance. The width of this minimum is determined by the splitting between the singlet and triplet states, $2|\Delta_{ST}|$.

The bias voltage dependence of TMR is shown in figure 34. Generally, TMR displays a nontrivial dependence on the ground state of the dot. When the dot is occupied by a singlet, $\Delta_{ST} < 0$, TMR displays a maximum plateau at low bias, which can be approximated by, $\mathrm{TMR}^{S=0} = 2p^2/(1-p^2)$ [189]. This is the Jullière value of TMR. Here, it results from the fact that in this transport regime current flows due to non-spin-flip cotunnelling. On the other hand, for $\Delta_{ST} \geqslant 0$, the TMR exhibits a minimum at zero bias, which can be seen in figure 34 for $\Delta_{ST} = 0$ and $\Delta_{ST} = 2.5\Gamma$.

5.3. Multi-level quantum dots based on single-wall carbon nanotubes

When the number of discrete levels in the dot (relevant for electronic transport) becomes larger than two, transport characteristics of the dots attached to ferromagnetic leads become more complex and reveal further interesting features. Such features were observed experimentally mainly in molecule-based quantum dots. When a large natural molecule is weakly attached to metallic leads, it can be treated simply as a multi-level QD [203–205]. As a specific case, we discuss transport properties of a single-wall metallic carbon nanotube (CNT) weakly coupled to ferromagnetic leads [206–210].

Sequential transport in CNTs weakly coupled to nonmagnetic and ferromagnetic leads was considered in a recent paper [206], where TMR and the Fano factor have been calculated with the real-time diagrammatic technique. The system was modelled by the Hamiltonian in the form introduced by Oreg *et al* [211],

$$H_{QD} = \sum_{\mu j\sigma} \varepsilon_{\mu j} n_{\mu j\sigma} + \frac{U}{2}\left[\sum_{\mu j\sigma} n_{\mu j\sigma} - N_0\right]^2 + \delta U \sum_{\mu j} n_{\mu j\uparrow} n_{\mu j\downarrow} + J \sum_{\mu j,\mu' j'} n_{\mu j\uparrow} n_{\mu' j'\downarrow}, \quad (58)$$

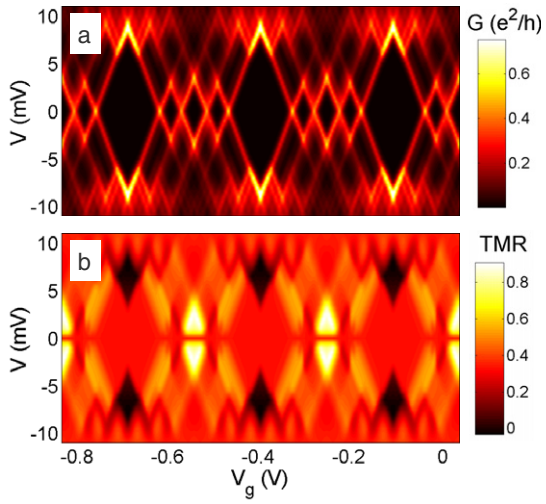

Figure 35. The differential conductance in the parallel configuration (a) and tunnel magnetoresistance (b) as a function of bias and gate voltages. The parameters are: $\Delta = 8.4$ meV, $U/\Delta = 0.26$, $J/\Delta = 0.12$, $\delta U/\Delta = 0.04$, $\delta/\Delta = 0.1$, $k_{\mathrm{B}}T/\Delta = 0.025$, $p_{\mathrm{L}} = p_{\mathrm{R}} = 0.5$, $x = 0.14$, and $\Gamma = 0.2$ meV.

where $n_{\mu j\sigma} = d^{\dagger}_{\mu j\sigma} d_{\mu j\sigma}$, and $d^{\dagger}_{\mu j\sigma}$ ($d_{\mu j\sigma}$) is the creation (annihilation) operator of an electron with spin σ on the jth level in the subband μ ($\mu = 1, 2$). The corresponding energy $\varepsilon_{\mu j}$ of the jth discrete level in the subband μ is given by $\varepsilon_{\mu j} = j\Delta + (\mu - 1)\delta$, where Δ is the mean level spacing and δ describes the energy mismatch between the discrete levels corresponding to the two subbands. The second term in equation (58) stands for the electrostatic energy of a charged CNT, with U denoting the charging energy and N_0 being the charge on the nanotube induced by gate voltages. The next term corresponds to the on-level Coulomb interaction with δU being the relevant on-site Coulomb parameter. Finally, the last term in equation (58) describes the exchange energy, with J being the relevant exchange parameter.

In figure 35 we show the differential conductance in the parallel configuration and associated TMR, calculated in the first-order approximation. The results are for a specific choice of parameters, namely $\delta U + J > \delta$. The latter condition indicates that the following sequence of the ground states is realized when filling the CNT with electrons while sweeping the gate voltage (for $V = 0$): $S = 0, 1/2, 1, 1/2$, where S is the total spin of the nanotube. This means that in a certain transport regions, the system is in the triplet state at equilibrium. Figure 35(a) clearly reveals the four-fold pattern of the conductance spectra, associated with filling of the consecutive levels in the two electron subbands of the CNT. The corresponding TMR is shown in figure 35(b), and reveals a complex variation with both gate and bias voltages.

As shown in [206], shot noise calculated in the first-order approximation is super-Poissonian in the blockade regions, and sub-Poissonian in the transport regions where sequential tunnelling dominates. The corresponding Fano factor in the latter case is close to $1/2$, while in the former one it is above 1. Detailed calculations taking into account second-order (cotunnelling) processes show that the Fano factor in the blockade regions is generally larger than 1, although it is reduced in comparison to that derived in the first-order approximation, similarly to in the case of two-level dot.

6. Kondo effect in quantum dots coupled to ferromagnetic leads

When a quantum dot or a large molecule is strongly coupled to external leads, low-temperature transport characteristics reveal features that are typical of the Kondo phenomenon [51, 139, 174–176, 212]. To analyse the Kondo effect [213], one may use various theoretical techniques. For instance, one can use the perturbative methods, like the real-time diagrammatic technique discussed in previous sections. However, one has to go beyond the approximations used in the discussion of the sequential and cotunnelling transport. Another approximate method that is frequently used to study electronic transport through quantum dots, including the Kondo regime, is the equation of motion method for the relevant Green function. Alternatively, one may employ nonperturbative methods, such as for example the numerical renormalization-group method [214–217].

The Kondo effect [78] in electronic transport through a quantum dot was first predicted theoretically in [218, 219]. Since then, it has become well-documented experimentally [174, 220–223]. The dot with an odd number of electrons has a local spin, which at low temperatures, $k_{\mathrm{B}}T \leqslant k_{\mathrm{B}}T_{\mathrm{K}} \ll \Gamma$, and in the presence of strong coupling to the electrodes, behaves effectively like a magnetic Kondo impurity. Exchange coupling with the leads' electrons gives rise to spin fluctuations in the dot and screening of the dot's spin. This, in turn, leads to the formation of a singlet state and a Kondo resonance peak at the Fermi level in the dot's density of states. This Kondo-correlated state leads to an increased transmission through the dot, and also gives rise to a sharp zero-bias anomaly in the current–voltage characteristics. The successful observation of the Kondo effect in semiconductor-based quantum dots, as well as in molecular quantum dots based for instance on carbon nanotubes [224, 225] or other single molecules [226, 227] attached to metallic electrodes opened a new possibility to study the influence of ferromagnetism on the Kondo phenomenon [44, 51, 228].

In this section we briefly discuss how the Kondo effect is modified by ferromagnetism of the electrodes. First, we note that in the extreme case of half-metallic leads, i.e. in the absence of minority-spin electrons, the screening of the dot spin is not possible in the parallel magnetic configuration. Consequently, no Kondo-correlated state can be then formed in this particular magnetic configuration.

The possibility of the Kondo effect in a quantum dot attached to ferromagnetic electrodes was discussed in a number of papers [137, 139, 143, 212, 229–235]. It was shown, that the Kondo resonance in the parallel configuration is split and suppressed in the presence of ferromagnetic leads [139, 231, 232, 235, 234]. However, it was also demonstrated that this splitting can be compensated by an appropriate external magnetic field which restores the Kondo effect [139, 231].

Let us begin with the collinear (parallel and antiparallel) magnetic configurations. For the antiparallel configuration and vanishing magnetic field and bias voltage, the model is equivalent to a quantum dot coupled to a single lead with density of states $\rho_{L\uparrow}+\rho_{R\uparrow}=\rho_{L\downarrow}+\rho_{R\downarrow}$ [218, 219]. Thus, the usual Kondo resonance forms in such a case, which is the same as for nonmagnetic electrodes [78]. The situation changes in the parallel configuration, where there is an overall asymmetry for up and down spins, say $\rho_{L\uparrow}+\rho_{R\uparrow}>\rho_{L\downarrow}+\rho_{R\downarrow}$. This significantly reduces (or even suppresses) the Kondo effect.

6.1. Poor man's scaling approach

Some basic relations concerning the Kondo effect, and particularly those concerning the Kondo temperature, can be derived from a simple poor man's scaling [236] performed in two stages [237]. First one reduces the energy scale of the effective electron bandwidth D starting from D_0. This leads to a renormalization of the level position $\epsilon_{d\sigma}$ according to the scaling equations [139]

$$\frac{d\epsilon_{d\sigma}}{d\ln(D_0/D)}=\frac{\Gamma_{\bar\sigma}}{2\pi}. \tag{59}$$

This leads to a spin splitting of the level, which in the presence of a magnetic field simply adds to the initial Zeeman splitting $\Delta\epsilon_d$. As a result, one finds

$$\Delta\widetilde{\epsilon}_d=\widetilde{\epsilon}_{d\uparrow}-\widetilde{\epsilon}_{d\downarrow}=-(1/\pi)P\Gamma\ln(D_0/D)+\Delta\epsilon_d. \tag{60}$$

The scaling of equation (59) is terminated at $\widetilde{D}\sim-\widetilde{\epsilon}_d$ [237].

The strong coupling limit can be reached by tuning the external magnetic field B in such a way that the total effective Zeeman splitting vanishes, $\Delta\widetilde{\epsilon}_d=0$. In the second stage [236], spin fluctuations are integrated out. The Schrieffer–Wolff transformation [78] allows one to map the Anderson model, with renormalized parameters $\widetilde{D}$ and $\widetilde{\epsilon}_d$, to the effective Kondo Hamiltonian [139]

$$H_{\rm Kondo}=J_+S^+\sum_{rr'kq}a^\dagger_{rk\downarrow}a_{r'q\uparrow}+J_-S^-\sum_{rr'kq}a^\dagger_{rq\uparrow}a_{r'k\downarrow}+S^z\left(J_{z\uparrow}\sum_{rr'qq'}a^\dagger_{rq\uparrow}a_{r'q'\uparrow}-J_{z\downarrow}\sum_{rr'kk'}a^\dagger_{rk\downarrow}a_{r'k'\downarrow}\right), \tag{61}$$

with $J_+=J_-=J_{z\uparrow}=J_{z\downarrow}=|T|^2/|\widetilde{\epsilon}_d|\equiv J_0$ in the large-U limit. Although initially identical, the three coupling constants $J_+=J_-\equiv J_\pm$, $J_{z\uparrow}$, and $J_{z\downarrow}$ are renormalized differently during the second stage of scaling. The relevant scaling equations are

$$\frac{d(\rho_\pm J_\pm)}{d\ln(\widetilde{D}/D)}=\rho_\pm J_\pm(\rho_\uparrow J_{z\uparrow}+\rho_\downarrow J_{z\downarrow}) \tag{62}$$

$$\frac{d(\rho_\sigma J_{z\sigma})}{d\ln(\widetilde{D}/D)}=2(\rho_\pm J_\pm)^2. \tag{63}$$

All the coupling constants reach the stable strong coupling fixed point $J_\pm=J_{z\uparrow}=J_{z\downarrow}=\infty$ at the Kondo energy scale, $D\sim k_BT_K$. For the parallel configuration, the Kondo temperature in leading order depends on the polarization p in the leads following the formula

$$T_K(p)\approx\widetilde{D}\exp\left\{-\frac{1}{(\rho_\uparrow+\rho_\downarrow)J_0}\frac{\arctan h(p)}{p}\right\}. \tag{64}$$

The Kondo temperature is maximal for nonmagnetic leads, $p=0$, and vanishes for $p\to1$. The unitary limit for the parallel configuration can be reached by tuning the magnetic field, as discussed above. In this case, the maximum conductance through the quantum dot is the same as for nonmagnetic leads, i.e. $G^P_{\max,\sigma}=e^2/h$ per spin.

The scaling procedure was extended in [144, 145, 238] to noncollinear configurations, where instead of equation (64) one finds

$$T_K(p)\approx\widetilde{D}\exp\left\{-\frac{1}{(\rho_\uparrow+\rho_\downarrow)J_0}\frac{\arctan h(p\cos(\theta/2))}{p\cos(\theta/2)}\right\}. \tag{65}$$

This formula shows explicitly how the Kondo temperature varies with the angle θ between magnetic moments of the leads.

6.2. Numerical renormalization group

The numerical renormalization-group (NRG) technique [78, 214, 217] is one of the most powerful and accurate methods available currently to study strongly-correlated systems in the Kondo regime. This technique has been adapted recently to the case of a quantum dot coupled to ferromagnetic leads [145, 231, 232]. A simple way to model the ferromagnetic leads in the standard NRG procedure is to take the density of states in the leads to be constant and independent of electron spin, $\rho_{r\sigma}(\omega)\equiv\rho$, the bandwidths to be equal $D_\uparrow=D_\downarrow$, and lump all the spin dependence into the spin-dependent coupling parameter, $\Gamma_{r\sigma}(\omega)$, which can be taken as independent of energy.

The NRG method, with recent improvements related to high-energy features and finite magnetic field [239–242], is a well-established method to study the Kondo impurity (quantum dot) physics. Using this technique one can calculate the level occupation $n_{d\sigma}\equiv\langle d^\dagger_\sigma d_\sigma\rangle$, and the spin-dependent single-particle spectral density $A_\sigma(\omega)$ for arbitrary temperature T, magnetic field B and polarization p. Using the spectral function one can find the spin-resolved linear conductance

$$G_\sigma=\frac{e^2}{\hbar}\frac{\Gamma_{L\sigma}\Gamma_{R\sigma}}{(\Gamma_{L\sigma}+\Gamma_{R\sigma})}\int_{-\infty}^{\infty}d\omega\,A_\sigma(\omega)\left(-\frac{\partial f(\omega)}{\partial\omega}\right) \tag{66}$$

with $f(\omega)$ denoting the Fermi function.

6.3. Nonequilibrium transport: zero-bias anomaly

The Kondo effect is usually observed as a zero bias anomaly in the differential conductance. This requires theoretical methods applicable to nonequilibrium situations. One of such techniques is based on the nonequilibrium Green functions. The latter are usually determined from the relevant equation of motion and the appropriate decoupling scheme. To describe the main features of the Kondo effect in transport through quantum

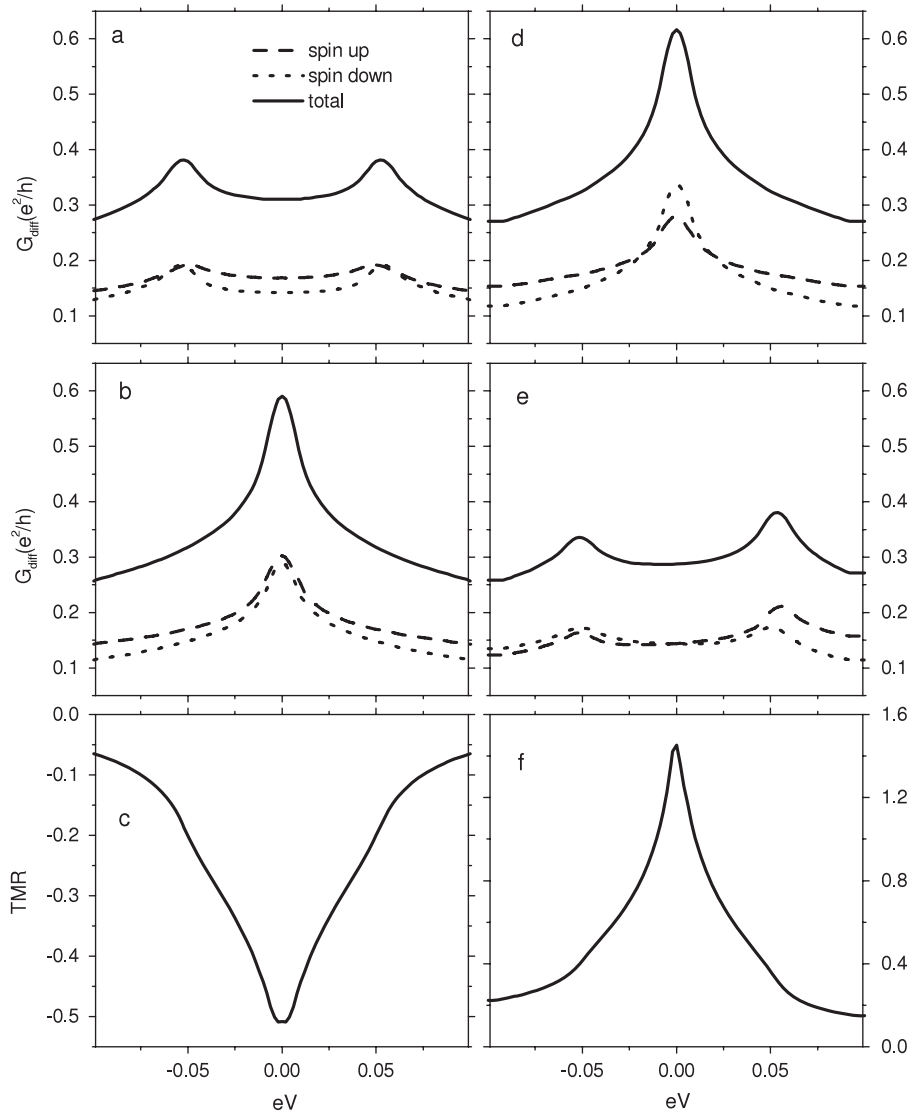

Figure 36. Differential conductance in the P ((a), (d)) and AP ((b), (e)) configurations, and the corresponding TMR ((c), (f)). Contributions to the conductance from spin-up (dashed lines) and spin-down (dotted lines) channels are also indicated. The left column ((a)–(c)) corresponds to zero magnetic field, whereas the right column ((d)–(f)) corresponds to the case when the compensating magnetic field $B = 14.53$ T is applied (for the Lande factor $g = 0.152$). The numerical results are for large U limit, while the other parameters are: $k_B T/\Gamma = 0.01$, $p = 0.2$, $\Gamma/D = 0.001$. Reprinted with permission from [233]. Copyright Springer 2004.

dots connected to ferromagnetic leads (at least qualitatively), one may use the decoupling scheme introduced in [135, 136], but generalized by a self-consistent determination of the level energy to account for the exchange field [139, 233]. Alternatively, one may calculate the exchange field first and then include it in the formalism by hand [234].

Figure 36 shows the differential conductance as a function of the transport voltage. For zero magnetic field there is a pronounced splitting of the peak in the parallel configuration (figure 36(a)), which can be tuned away by an appropriate external magnetic field (figure 36(b)). In the antiparallel configuration, in turn, the opposite happens, i.e. there is no splitting at $B = 0$ (figure 36(d)) and a finite splitting at $B > 0$ (figure 36(e)) with an additional asymmetry in the peak amplitudes as a function of the bias voltage. Figures 36(c), (f) show the corresponding TMR, which becomes negative without magnetic field and changes sign to positive when a compensating magnetic field is applied.

Within the EOM approach the effect of spin-dependent quantum charge fluctuations is accounted for in a self-consistent but intuitive manner. The real-time diagrammatic technique [104, 167] enables one to construct a systematic approach, where the effect of ferromagnetic electrodes can be analysed without any additional assumptions. Recently the resonant tunnelling approximation (RTA) was extended by Utsumi *et al* [142] to account for the influence of the electrodes' ferromagnetism on the Kondo phenomenon. This technique gives more reasonable results and allows for a further systematic insight into the physics of the transport through quantum dots in the Kondo regime.

The Kondo phenomenon in noncollinear magnetic configuration was considered in [143–145]. The results show

that in symmetric systems, the Kondo anomaly gradually disappears when the magnetic configuration varies from the antiparallel to parallel one. However, the main drop of the Kondo peak already appears at small deviations from the antiparallel alignment.

Recently Pasupathy *et al* [51] studied electronic transport through a single C_{60} molecule attached to ferromagnetic nickel electrodes in the Kondo regime. It was shown that the Kondo correlations appear even in the presence of ferromagnetic leads. The zero-bias anomaly in the nonequilibrium conductance, however, was split for a parallel alignment of the leads magnetization in agreement with theoretical predictions. For the antiparallel alignment, on the other hand, no splitting of the zero-bias anomaly was observed. Some residual splitting observed in this geometry for some samples can be interpreted as an effect of asymmetric coupling $\Gamma_L \neq \Gamma_R$. Similar behaviour has also been observed in electronic transport through carbon nanotubes coupled to ferromagnetic leads [243].

7. Concluding remarks

In this review we addressed certain aspects of electronic transport in mesoscopic tunnel junctions consisting of magnetic metallic nanoparticles, semiconducting quantum dots, or molecules attached to ferromagnetic electrodes. We are aware that the review does not cover all the problems considered in such systems and many references have not been included. There are some other aspects of electronic and spin transport which have been omitted. One of such aspects is spin torque acting on the island and/or electrodes in ferromagnetic single-electron transistors based on magnetic metallic nanoparticles [244]. Another topic omitted in this review is the role of electron coupling to a phonon bath. Such a coupling leads to new interesting phenomena in transport characteristics [245]. For instance, the electron–phonon coupling leads to phonon satellite peaks in the differential conductance. However, the most important spin effects generated by spin-dependent tunnelling through the barriers separating the central part from the ferromagnetic electrodes have been addressed.

We note that spin-polarized transport through nanostructures, where the Coulomb effects become important, has been rapidly developing in recent years. This applies not only to theoretical part of the subject, but also to the experimental side, where recent progress in nanotechnology allows one to attach external leads to individual nanoparticles, quantum dots, and single molecules. An interesting and new field within this topic is the spintronics based on molecular magnets. Such molecules are good candidates for magnetic memory cells and also are considered as potential candidates for information processing devices. There is no doubt, that the rapid progress in the physics and technology of spin-polarized electronic transport through nanostructures is stimulated by application possibilities in magnetoelectronics, spintronics, and information technology.

Acknowledgments

We acknowledge discussions with J König, J Martinek, W Rudziński, R Świrkowicz, and M Wilczyński. This work was supported by funds of the Ministry of Science and Higher Education as a research project in the period 2006–2009. IW also acknowledges support from the Foundation for Polish Science.

References

[1] Baibich M N, Broto J M, Fert A, Van Dau F N, Petroff F, Eitenne P, Creuzet G, Friederich A and Chazelas J 1988 *Phys. Rev. Lett.* **61** 2472
[2] Binasch G, Grünberg P, Saurenbach F and Zinn W 1989 *Phys. Rev.* B **39** 4828
[3] Barnaś J, Fuss A, Camley R E, Grünberg P and Zinn W 1990 *Phys. Rev.* B **42** 8110
[4] Barnaś J, Fuss A, Camley R E, Walz U, Grünberg P and Zinn W 1990 *Vacuum* **41** 1414
[5] Wolf S A, Awschalom D D, Buhrman R A, Daughton J M, von Molnar S, Roukes M L, Chtchelkanova A Y and Treger D M 2001 *Science* **294** 1488
[6] Ziese M and Thornton M J (ed) 2001 *Spin Electronics* (Berlin: Springer)
[7] Gregg J F, Petej I, Jouguelet E and Dennis C 2002 *J. Phys. D: Appl. Phys.* **35** R121
[8] Maekawa S and Shinjo T 2002 *Spin Dependent Transport in Magnetic Nanostructures* (London: Taylor and Francis)
[9] Awschalom D D, Loss D and Samarth N (ed) 2002 *Semiconductor Spintronics and Quantum Computation* (Berlin: Springer)
[10] Zutic I, Fabian J and Das Sarma S 2004 *Rev. Mod. Phys.* **76** 323
[11] Dyakonov M I 2004 *Future Trends in Microelectronics: The Nano, the Giga, and the Ultra* ed S Luryi, J Xu and A Zaslavsky (New York: Wiley–IEEE)
[12] Maekawa S (ed) 2006 *Concepts in Spin Electronics* (Oxford: Oxford University Press)
[13] Jullière M 1975 *Phys. Lett.* A **54** 225
[14] Averin D V and Likharev K K 1991 *Mesoscopic Phenomenon in Solids* ed B L Altshuler, P A Lee and R A Webb (Amsterdam: North-Holland)
[15] Grabert H and Devoret M H (ed) 1992 *Single Charge Tunneling: Coulomb Blockade Phenomena in Nanostructures* (*NATO ASI Series B: Physics* vol 294) (New York: Plenum)
[16] Datta S 1995 *Electronic Transport in Mesoscopic Systems* (Cambridge: Cambridge University Press)
[17] Ferry D K and Goodnick S M 1997 *Transport in Nanostructures* (Cambridge: Cambridge University Press)
[18] Kouwenhoven L P, Marcus C M, McEuen P L, Tarucha S, Westervelt R M and Wingreen N S 1997 *Proc. NATO Advanced Study Institute on Mesoscopic Electron Transport* (*Kluwer Series* E345) ed L L Sohn, L P Kouwenhoven and G Schön (Dordrecht: Kluwer)
[19] Schön G 1998 *Quantum Transport and Dissipation* ed T Dittrich, P Haenggi, G Ingold, B Kramer, G Schön and W Zwerger (New York: Wiley–VCH) chapter 3
[20] Likharev K K 1999 Single-electron devices and their applications *Proc. IEEE* **87** 606
[21] von Delft J and Ralph D C 2001 *Phys. Rep.* **345** 61
[22] Heinzel T 2003 *Mesoscopic Electronics in Solid State Nanostructures* (New York: Wiley–VCH)
[23] Seneor P, Bernand-Mantel A and Petroff F 2007 *J. Phys.: Condens. Matter* **19** 165222
[24] Ernult F, Yakushiji K, Mitani S and Takanashi K 2007 *J. Phys.: Condens. Matter* **19** 165214

[25] Ono K, Shimada H, Kobayashi S and Outuka Y 1996 *J. Phys. Soc. Japan* **65** 3449
[26] Ono K, Shimada H and Outuka Y 1997 *J. Phys. Soc. Japan* **66** 1261
[27] Brückl H, Reiss G, Vinzelberg H, Bertram M, Mönch I and Schumann J 1998 *Phys. Rev.* B **58** R8893
[28] Chen C D, Kuo W, Chung D S, Shyu J H and Wu C S 2002 *Phys. Rev. Lett.* **88** 047004
[29] Chen C D, Yao Y D, Lee S F and Shyu J H 2002 *J. Appl. Phys.* **91** 7469
[30] Shyu J H, Yao Y D, Chen C D and Lee S F 2003 *J. Appl. Phys.* **93** 8421
[31] Johansson J, Urech M, Haviland D and Korenivski V 2003 *Phys. Rev. Lett.* **91** 149701
[32] Helman J S and Abeles B 1976 *Phys. Rev. Lett.* **37** 1429
[33] Schelp L F, Fert A, Fettar F, Holody P, Lee S F, Maurice J L, Petroff F and Vaures A 1997 *Phys. Rev.* B **56** R5747
[34] Fettar F, Lee S F, Petroff F, Vaures A, Holody P, Schelp L F and Fert A 2002 *Phys. Rev.* B **65** 174415
[35] Mitani S, Takahashi S, Takanashi K, Yakushiji K, Maekawa S and Fujimori H 1998 *Phys. Rev. Lett.* **81** 2799
[36] Imamura H, Chiba J, Mitani S, Takanashi K, Takahashi S, Maekawa S and Fujimori H 2000 *Phys. Rev.* B **61** 46
[37] Yakushiji K, Mitani S, Takanashi K, Takahashi S, Maekawa S, Imamura H and Fujimori H 2001 *Appl. Phys. Lett.* **78** 515
[38] Yakushiji K, Mitani S, Takanashi K and Fujimori H 2002 *J. Appl. Phys.* **91** 7038
[39] Ernult F, Yamane K, Mitani S, Yakushiji K, Takanashi K, TakahashiY K and Hono K 2004 *Appl. Phys. Lett.* **84** 3106
[40] Yakushiji K, Ernult F, Imamura H, Yamane K, Mitani S, Takanashi K, Takahashi S, Maekawa S and Fujimori H 2005 *Nat. Mater.* **4** 57
[41] Deshmukh M M and Ralph D C 2002 *Phys. Rev. Lett.* **89** 266803
[42] Hamaya K, Masubuchi S, Kawamura M, Machida T, Jung M, Shibata K, Hirakawa K, Taniyama T, Ishida S and Arakawa Y 2007 *Appl. Phys. Lett.* **90** 053108
[43] Hamaya K, Kitabatake M, Shibata K, Jung M, Kawamura M, Hirakawa K, Machida T, Taniyama T, Ishida S and Arakawa Y 2007 *Appl. Phys. Lett.* **91** 22107
[44] Amaya K, Kitabatake M, Shibata K, Jung M, Kawamura M, Hirakawa K, Machida T, Taniyama T, Ishida S and Arakawa Y 2007 *Appl. Phys. Lett.* **91** 232105
[45] Hamaya K, Kitabatake M, Shibata K, Jung M, Kawamura M, Ishida S, Taniyama T, Hirakawa K, Arakawa Y and Machida T 2008 *Phys. Rev.* B **77** 081302(R)
[46] Chye Y, White M E, Johnston-Halperin E, Gerardot B D, Awschalom D D and Petroff P M 2002 *Phys. Rev.* B **66** 201301(R)
[47] Jansen R and Moodera J S 1999 *Appl. Phys. Lett.* **75** 400
[48] Tanoue S and Yamasaki A 2000 *J. Appl. Phys.* **88** 4764
[49] Bernand-Mantel A, Seneor P, Lidgi N, Munoz M, Cros V, Fusil S, Bouzehouane K, Deranlot C, Vaures A, Petroff F and Fert A 2006 *Appl. Phys. Lett.* **89** 062502
[50] Yang H, Yang S-H and Parkin S S P 2008 *Nano Lett.* **8** 340
[51] Pasupathy A N, Bialczak R C, Martinek J, Grose J E, Donev L A K, McEuen P L and Ralph D C 2004 *Science* **306** 86
[52] Tsukagoshi K, Alphenaar B W and Ago H 1999 *Nature* **401** 572
[53] Zhao B, Mönch I, Vinzelberg H, Mühl T and Schneider C M 2002 *Appl. Phys. Lett.* **80** 3144
[54] Zhao B, Mönch I, Vinzelberg H, Mühl T and Schneider C M 2002 *J. Appl. Phys.* **91** 7026
[55] Jensen A, Nygård J and Borggreen J 2003 *Proc. Int. Symp. on Mesoscopic Superconductivity and Spintronics* ed H Takayanagi and J Nitta (Singapore: World Scientific) pp 33–7
[56] Sahoo S, Kontos T, Furer J, Hoffmann C, Gräber M, Cottet A and Schönenberger C 2005 *Nat. Phys.* **1** 102
[57] Jensen A, Hauptmann J R, Nygård J and Lindelof P E 2005 *Phys. Rev.* B **72** 035419
[58] Man H T, Wever I J W and Morpurgo A F 2006 *Phys. Rev.* B **73** 241401(R)
[59] Liu L W, Fang J H, Lu L, Yang H F, Jin A Z and Gu C Z 2006 *Phys. Rev.* B **74** 245429
[60] Nagabhirava B, Bansal T, Sumanasekera G U, Alphenaara B W and Liu L 2006 *Appl. Phys. Lett.* **88** 023503
[61] Cottet A, Kontos T, Sahoo S, Man H T, Choi M-S, Belzig W, Bruder C, Morpurgo A F and Schönenberger C 2006 *Semicond. Sci. Technol.* **21** S78
[62] Schönenberger C 2006 *Semicond. Sci. Technol.* **21** S1
[63] Fulton T A and Dolan G J 1987 *Phys. Rev. Lett.* **59** 109
[64] Mullen K, Ben-Jacob E, Jaklevic R C and Schuss Z 1988 *Phys. Rev.* B **37** 98
[65] Likharev K K 1988 *J. Res. Dev.* **32** 144
[66] Geerligs L J, Anderegg V F, Holweg P A M, Mooij J E, Pothier H, Esteve D, Urbina C and Devoret M H 1990 *Phys. Rev. Lett.* **64** 2691
[67] Meir Y, Wingreen N S and Lee P A 1991 *Phys. Rev. Lett.* **66** 3048
[68] Meir Y and Wingreen N S 1992 *Phys. Rev. Lett.* **68** 2512
[69] Devoret M H, Esteve D and Urbina C 1992 *Nature* **360** 547
[70] Averin D V and Likharev K K 1986 *J. Low Temp. Phys.* **62** 345
[71] Beenakker C W J 1991 *Phys. Rev.* B **44** 1646
[72] Kouwenhoven L P, Johnson A T, van der Vaart N C, Harmans C J P M and Foxon C T 1991 *Phys. Rev. Lett.* **67** 1626
[73] Barnaś J and Fert A 1998 *Phys. Rev. Lett.* **80** 1058
[74] Takahashi S and Maekawa S 1998 *Phys. Rev. Lett.* **80** 1758
[75] Averin D V and Odintsov A A 1989 *Phys. Lett.* A **140** 251
[76] Averin D V and Nazarov Yu V 1990 *Phys. Rev. Lett.* **65** 2446
[77] Geerligs L J, Averin D V and Mooij J E 1990 *Phys. Rev. Lett.* **65** 3037
[78] Hewson A C 1993 *The Kondo Problem to Heavy Fermions* (Cambridge: Cambridge University Press)
[79] Kastner M A 1992 *Rev. Mod. Phys.* **64** 849
[80] Devoret M and Glatti Ch 1998 *Phys. World* **11** (September) 29
[81] Averin A V and Korotkov A N 1990 *Zh. Eksp. Teor. Fiz.* **97** 1661
[82] Averin D V, Korotkov A N and Likharev K K 1991 *Phys. Rev.* B **44** 6199
[83] Amman M, Wilkins R, Ben-Jacob E, Maker P D and Jaklevic R C 1991 *Phys. Rev.* B **43** 1146
[84] Hanna A E and Tinkham M 1991 *Phys. Rev.* **44** 5919
[85] Whan C B, White J and Orladno T P 1996 *Appl. Phys. Lett.* **68** 2996
[86] Hirvi K P, Paalanen M A and Pekola J P 1996 *J. Appl. Phys.* **80** 256
[87] Melsen J A, Hanke U, Müller H-O and Chao K-A 1997 *Phys. Rev.* B **55** 10638
[88] Park H, Park J, Lim A K L, Anderson E H, Alivisatos A P and Mc Euen P L 2000 *Nature* **407** 57
[89] Lientschnig G, Weymann I and Hadley P 2003 *Japan. J. Appl. Phys.* **42** 6467
[90] Moodera J S, Kinder L R, Wong T M and Meservey R 1995 *Phys. Rev. Lett.* **74** 3273
[91] Moodera J S and Kinder L R 1996 *J. Appl. Phys.* **79** 4724
[92] Imamura H, Chiba J, Mitani S, Takanashi K, Takahashi S, Maekawa S and Fujimori H 2000 *Phys. Rev.* B **61** 46
[93] Barnaś J and Fert A 1998 *Europhys. Lett.* **44** 85
[94] Majumdar K and Hershfield S 1998 *Phys. Rev.* B **57** 11521
[95] Brataas A, Nazarov Yu V, Inoue J and Bauer G E W 1999 *Eur. Phys. J.* B **9** 421
[96] Korotkov A N and Safarov V I 1999 *Phys. Rev.* B **59** 89
[97] Martinek J, Barnaś J, Maekawa S, Schoeller H and Schön G 2002 *Phys. Rev.* B **66** 014402
[98] Weymann I and Barnaś J 2003 *Phys. Status Solidi* b **236** 651

[99] Takanashi K, Mitani S, Chiba J and Fujimori H 2000 *J. Appl. Phys.* **87** 6331
[100] Mitani S, Takahashi S, Takanashi K, Yakushiji K, Maekawa S and Fujimori H 1988 *Phys. Rev. Lett.* **81** 2799
[101] Pashkin Yu A, Nakamura Y and Tsai J S 2000 *Appl. Phys. Lett.* **76** 2256
[102] Martinek J, Barnaś J, Michałek G, Bułka B R and Fert A 1999 *J. Magn. Magn. Mater.* **207** L1
[103] Barnaś J, Martinek J, Michałek G, Bułka B R and Fert A 2000 *Phys. Rev.* B **62** 12363
[104] Schoeller H and Schön G 1994 *Phys. Rev.* B **50** 18436
[105] Barnaś J and Fert A 1999 *J. Magn. Magn. Mater.* **192** 391
[106] Lubzens D and Schultz S 1976 *Phys. Rev. Lett.* **36** 1104
[107] Johnson M and Silsbee R H 1985 *Phys. Rev. Lett.* **55** 1790
[108] Imamura H, Takahashi S and Maekawa S 1999 *Phys. Rev.* B **59** 6017
[109] Aronov A G 1976 *Pis. Zh. Eksp. Teor. Fiz.* **24** 37
Aronov A G 1976 *JETP Lett.* **24** 37 (Engl. Transl.)
[110] König J, Schoeller H and Schön G 1997 *Phys. Rev. Lett.* **78** 4482
[111] König J, Schoeller H and Schön G 1998 *Phys. Rev.* B **58** 7882
[112] Jedema F J, Filip A T and van Wees J 2001 *Nature* **410** 345
[113] Kuo W and Chen C D 2002 *Phys. Rev.* B **65** 104427
[114] Brataas A, Hirano M, Inoue J, Nazarov Yu V and Bauer G E W 2001 *Japan. J. Appl. Phys.* **40** 2329
[115] Inoue J-I and Brataas A 2004 *Phys. Rev.* B **70** 140406(R)
[116] Blanter Ya M and Büttiker M 2000 *Phys. Rep.* **336** 1
[117] Bułka B R, Martinek J, Michałek G and Barnaś J 1999 *Phys. Rev.* B **60** 12246
[118] Korotkov A N 1994 *Phys. Rev.* B **49** 10381
[119] Hershfield S, Davies J H, Hyldgaard P, Stanton C J and Wilkins J W 1993 *Phys. Rev.* B **47** 1967
[120] Hanke U, Galperin Y M, Chao K A and Zou N 1993 *Phys. Rev.* B **48** 17209
[121] Hanke U, Galperin Y M and Chao K A 1994 *Phys. Rev.* B **50** 1595
[122] Imamoglu A and Yamamoto Y 1993 *Phys. Rev. Lett.* **70** 3327
[123] van Vliet K M and Fassett J R 1965 *Fluctuation Phenomena in Solids* ed R E Burgess (New York: Academic) p 267
[124] Weymann I and Barnaś J 2006 *Phys. Rev.* B **73** 033409
[125] Shimada H and Ootuka Y 2001 *Phys. Rev.* B **64** 235418
[126] van der Wiel W G, De Franceschi S, Elzerman J M, Fujisawa T, Tarucha S and Kouwenhoven L P 2003 *Rev. Mod. Phys.* **75** 1
[127] Nakashima H and Uozumi K 1997 *J. Vac. Sci. Technol.* B **15** 1411
[128] Nguyen V H, Nguyen L and Nguyen H N 2004 *J. Appl. Phys.* **96** 3302
[129] Kastner M 1993 *Phys. Today* **44** 24
[130] Kouwenhoven L P 1995 *Science* **268** 5216
[131] Kouwenhoven L P and Marcus C 1998 *Phys. World* **11** (June) 35
[132] Hanson R, Witkamp B, Vandersypen L M K, Willems van Beveren L H, Elzerman J M and Kouvenhoven L P 2003 *Phys. Rev. Lett.* **91** 196802
[133] Loss D and DiVincenzo D P 1998 *Phys. Rev.* A **57** 120
[134] Loss D and Sukhorukov E V 2000 *Phys. Rev. Lett.* **84** 1035
[135] Meir Y, Wingreen N S and Lee P A 1993 *Phys. Rev. Lett.* **70** 2601
[136] Wingreen N S and Meir Y 1994 *Phys. Rev.* B **49** 11040
[137] Sergueev N, Sun Q-F, Guo H, Wang B G and Wang J 2002 *Phys. Rev.* B **65** 165303
[138] López R and Sánchez D 2003 *Phys. Rev. Lett.* **90** 116602
[139] Martinek J, Utsumi Y, Imamura H, Barnaś J, Maekawa S, König J and Schön G 2003 *Phys. Rev. Lett.* **91** 127203
[140] Fransson J 2005 *Phys. Rev.* B **72** 045415
[141] Fransson J 2005 *Europhys. Lett.* **70** 796
[142] Utsumi Y, Martinek J, Schön G, Imamura H and Maekawa S 2005 *Phys. Rev.* B **71** 245116
[143] Świrkowicz R, Wilczyński M, Wawrzyniak M and Barnaś J 2006 *Phys. Rev.* B **73** 193312
[144] Matsubayashi D and Eto M 2007 *Phys. Rev.* B **75** 165319
[145] Simon P, Cornaglia P S, Feinberg D and Balseiro C A 2007 *Phys. Rev.* B **75** 045310
[146] Bułka B R 2000 *Phys. Rev.* B **62** 1186
[147] Rudziński W and Barnaś J 2001 *Phys. Rev.* B **64** 085318
[148] König J and Martinek J 2003 *Phys. Rev. Lett.* **90** 166602
[149] Braun M, König J and Martinek J 2004 *Phys. Rev.* B **70** 195345
[150] Rudziński W, Barnaś J, Świrkowicz R and Wilczyński M 2005 *Phys. Rev.* B **71** 205307
[151] Braig S and Brouwer P W 2005 *Phys. Rev.* B **71** 195324
[152] Wetzels W, Bauer G E W and Grifoni M 2005 *Phys. Rev.* B **72** 020407(R)
[153] Braun M, König J and Martinek J 2006 *Phys. Rev.* B **74** 075328
[154] Hartmann U and Wilhelm F K 2003 *Phys. Rev.* B **67** 161307(R)
[155] Weymann I, Barnaś J, König J, Martinek J and Schön G 2005 *Phys. Rev.* B **72** 113301
[156] Weymann I, König J, Martinek J, Barnaś J and Schön G 2005 *Phys. Rev.* B **72** 115334
[157] Weymann I and Barnaś J 2006 *Phys. Rev.* B **73** 205309
[158] Pedersen J N, Thomassen J Q and Flensberg K 2005 *Phys. Rev.* B **72** 045341
[159] Braig S and Brouwer P W 2005 *Phys. Rev.* B **71** 195324
[160] Weymann I and Barnaś J 2005 *Eur. Phys. J.* B **46** 289
[161] Weymann I and Barnaś J 2007 *Phys. Rev.* B **75** 155308
[162] Świrkowicz R, Barnaś J and Wilczyński M 2002 *J. Phys.: Condens. Matter* **14** 2011
[163] Zhang L Y, Wang C Y, Wei Y G, Liu X Y and Davidović D 2005 *Phys. Rev.* B **72** 155445
[164] Anderson P W 1961 *Phys. Rev.* **124** 41
[165] Kogan A, Amasha S, Goldhaber-Gordon D, Granger G, Kastner M A and Shtrikman H 2004 *Phys. Rev. Lett.* **93** 166602
[166] König J 1999 *Quantum Fluctuations in the Single-Electron Transistor* (Aachen: Shaker)
[167] König J, Schmid J, Schoeller H and Schön G 1996 *Phys. Rev.* B **54** 16820
[168] König J, Schoeller H and Schön G 1996 *Phys. Rev. Lett.* **76** 1715
[169] Thielmann A, Hettler M H, König J and Schön G 2003 *Phys. Rev.* B **68** 115105
[170] Thielmann A, Hettler M H, König J and Schön G 2005 *Phys. Rev. Lett.* **95** 146806
[171] Kang K and Min B I 1997 *Phys. Rev.* B **55** 15412
[172] De Franceschi S, Sasaki S, Elzerman J M, van der Wiel W G, Tarucha S and Kouvenhoven L P 2001 *Phys. Rev. Lett.* **86** 878
[173] Zumbühl D M, Marcus C M, Hanson M P and Gossard A C 2004 *Phys. Rev. Lett.* **93** 256801
[174] Cronenwett S M, Oosterkamp T H and Kouvenhoven L P 1998 *Science* **281** 540
[175] Gores J, Goldhaber-Gordon D, Heemeyer S, Kastner M A, Shtrikman H, Mahalu D and Meirav U 2000 *Phys. Rev.* B **62** 2188
[176] Sasaki S, De Franceschi S, Elzerman J M, van der Wiel W G, Eto M, Tarucha S and Kouvenhoven L P 2000 *Nature* **405** 764
[177] Fujisawa T, Austing D G, Tokura Y, Hirayama Y and Tarucha S 2002 *Nature* **419** 278
[178] Elzerman J M, Hanson R, van Beveren L H W, Witkamp B, Vandersypen L M K and Kouwenhoven L P 2004 *Nature* **430** 6998
[179] König J, Martinek J, Barnas J and Schön G 2005 *CFN Lectures on Functional Nanostructures* (*Springer Lecture Notes in Physics* vol 658) ed K Busch *et al* (Berlin: Springer) p 145
[180] Rudziński W and Barnaś J 2004 *J. Magn. Magn. Mater.* **279** 134

[181] Wilczyński M, Świrkowicz R, Rudziński W, Barnaś J and Dugaev V 2005 *J. Magn. Magn. Mater.* **290** 209
[182] Pedersen J N, Thomassen J Q and Flensberg K 2005 *Phys. Rev.* B **72** 045341
[183] Rudziński W, Barnaś J, Świrkowicz R and Wilczyński M 2005 *Phys. Status Solidi* b **242** 342
[184] Mu H-F, Su G and Zheng Q-R 2006 *Phys. Rev.* B **73** 054414
[185] Thielmann A, Hettler M H, König J and Schön G 2005 *Phys. Rev.* B **71** 045341
[186] Belzig W 2005 *Phys. Rev.* B **71** 161301(R)
[187] Elste F and Timm C 2006 *Phys. Rev.* B **73** 235305
[188] Weymann I and Barnaś J 2007 *J. Phys.: Condens. Matter* **19** 096208
[189] Weymann I 2006 *Europhys. Lett.* **76** 1200
[190] Cottet A and Choi M-S 2006 *Phys. Rev.* B **74** 235316
[191] Sukhorukov E V, Burkard G and Loss D 2001 *Phys. Rev.* B **63** 125315
[192] Cottet A, Belzig W and Bruder C 2004 *Phys. Rev. Lett.* **92** 206801
[193] Cottet A, Belzig W and Bruder C 2004 *Phys. Rev.* B **70** 115315
[194] Fransson J 2006 *Nanotechnology* **17** 5344
[195] Weinmann D, Häusler W and Kramer B 1995 *Phys. Rev. Lett.* **74** 984
[196] Fransson J and Rasander M 2006 *Phys. Rev.* B **73** 205333
[197] Fransson J 2006 *New J. Phys.* **8** 114
[198] Ono K, Austing D G, Tokura Y and Tarucha S 2002 *Science* **297** 1313
[199] Inarrea J, Platero G and MacDonald A H 2007 *Phys. Rev.* B **76** 085329
[200] Weymann I and Barnaś J 2008 *Phys. Rev.* B **77** 075305
[201] Izumida W, Sakai O and Tarucha S 2001 *Phys. Rev. Lett.* **87** 216803
[202] Dong B and Lei X L 2002 *Phys. Rev.* B **66** 113310
[203] Liang W, Bockrath M and Park H 2002 *Phys. Rev. Lett.* **88** 126801
[204] Sapmaz S, Jarillo-Herrero P, Kong J, Dekker C, Kouwenhoven L P and van der Zant H S J 2005 *Phys. Rev.* B **71** 153402
[205] Onac E, Balestro F, Trauzettel B, Lodewijk C F J and Kouwenhoven L P 2006 *Phys. Rev. Lett.* **96** 026803
[206] Weymann I, Barnaś J and Krompiewski S 2007 *Phys. Rev.* B **76** 155408
[207] Mayrhofer L and Grifoni M 2007 *Eur. Phys. J.* B **56** 107
[208] Koller S, Mayrhofer L, Grifoni M and Wetzels W 2007 *New J. Phys.* **9** 348
[209] Weymann I and Barnaś J 2008 *Appl. Phys. Lett.* **92** 103127
[210] Weymann I, Barnaś J and Krompiewski S 2008 *Preprint* 0803.1969 [cond-mat]
[211] Oreg Y, Byczuk K and Halperin B I 2000 *Phys. Rev. Lett.* **85** 365
[212] Lopez R and Sanchez D 2003 *Phys. Rev. Lett.* **90** 116602
[213] Kondo J 1964 *Prog. Theor. Phys.* **32** 37
[214] Wilson K G 1975 *Rev. Mod. Phys.* **47** 773
[215] Krishna-Murthy H R, Wilkins J W and Wilson K G 1980 *Phys. Rev.* B **21** 1003
[216] Krishna-Murthy H R, Wilkins J W and Wilson K G 1980 *Phys. Rev.* B **21** 1044
[217] Bulla R, Costi T and Pruschke T 2008 *Rev. Mod. Phys.* **80** 395
[218] Glazman L I and Raikh M E 1988 *JETP Lett.* **47** 452
[219] Ng T K and Lee P A 1988 *Phys. Rev. Lett.* **61** 1768
[220] Goldhaber-Gordon D, Shtrikman H, Mahalu D, Abusch-Magder D, Meirav U and Kastner M A 1998 *Nature* **391** 156
[221] Simmel F, Blick R H, Kotthaus J P, Wegscheider W and Bichler M 1999 *Phys. Rev. Lett.* **83** 804
[222] Schmid J, Weis J, Eberl K and von Klitzing K 2000 *Phys. Rev. Lett.* **84** 5824
[223] van der Wiel G W, De Franceschi S, Fujisawa T, Elzerman J M, Tarucha S and Kouwenhoven L P 2000 *Science* **289** 2105
[224] Nygård J, Cobden D H and Lindelof P E 2000 *Nature* **408** 342
[225] Buitelaar M R, Bachtold A, Nussbaumer T, Iqbal M and Schönenberger C 2002 *Phys. Rev. Lett.* **88** 156801
[226] Park J, Pasupathy A N, Goldsmith J I, Chang C, Yaish Y, Petta J R, Rinkoski M, Sethna J P, Abruna H D, McEuen P L and Ralph D C 2002 *Nature* **417** 722
[227] Liang W, Shores M P, Bockrath M, Long J R and Park H 2002 *Nature* **417** 725
[228] Nygård J, Koehl W F, Mason N, DiCarlo L and Marcus C M 2004 *Preprint* cond-mat/0410467
[229] Zhang P, Xue Q K, Wang Y P and Xie X C 2002 *Phys. Rev. Lett.* **89** 286803
[230] Bułka B R and Lipiński S 2003 *Phys. Rev.* B **67** 024404
[231] Martinek J, Sindel M, Borda L, Barnaś J, König J, Schön G and von Delft J 2003 *Phys. Rev. Lett.* **91** 247202
[232] Choi M S, Sanchez D and Lopez R 2004 *Phys. Rev. Lett.* **92** 056601
[233] Świrkowicz R, Wilczyński M and Barnaś J 2004 *Czech. J. Phys.* **54** (Suppl. D) D615
[234] Świrkowicz R, Barnaś J and Wilczyński M 2006 *J. Phys.: Condens. Matter* **18** 2291
[235] Sindel M, Borda L, Martinek J, Bulla R, König J, Schön G, Maekawa S and von Delft J 2007 *Phys. Rev.* B **76** 045321
[236] Anderson P W 1970 *J. Phys. C: Solid State Phys.* **3** 2439
[237] Haldane F D M 1978 *Phys. Rev. Lett.* **40** 416
[238] Wawrzyniak M, Świrkowicz R, Wilczyński M and Barnaś J 2008 *Acta Phys. Pol.* A **113** 553
[239] Costi T A, Hewson A C and Zlatic V 1994 *J. Phys.: Condens. Matter* **6** 2519
[240] Hofstetter W 2000 *Phys. Rev. Lett.* **85** 1508
[241] Costi T A 2000 *Phys. Rev. Lett.* **85** 1504
[242] Costi T A 2001 *Phys. Rev.* B **64** 241310(R)
[243] Hauptmann J R, Paaske J and Lindelof P E 2008 *Nature Phys.* **4** 373
[244] Kowalik M, Wiśniewska J and Barnaś J 2006 *Mater. Sci. Pol.* **24** 815
Kowalik M, Weymann I and Barnaś J 2007 *Mater. Sci.* **25** 453
[245] Galperin M, Ratner M A and Nitzan A 2007 *J. Phys.: Condens. Matter* **19** 103201